U.PORTO

FEUP FACULDADE DE ENGENHARIA UNIVERSIDADE DO PORTO

RAILWAY VEHICLE OUT-OF-ROUNDNESS DETECTION WITH MULTIPLE RECORDS:

Simulation and algorithm validation

VÍTOR TIAGO CASTRO GONÇALVES

Dissertation submitted in partial fulfilment of the requirements for the degree of

MASTER IN CIVIL ENGINEERING — MAJOR IN TERRITORIAL PLANNING AND TRANSPORTS

Supervisor: Prof. Dr Cecília Maria Nogueira Alvarenga Santos do Vale, PhD

Co-supervisor: Dr Araliya Mosleh, PhD

FEBRUARY 2023

MESTRADO EM ENGENHARIA CIVIL 2022/2023

DEPARTAMENTO DE ENGENHARIA CIVIL

Tel. +351-22-508 1901

Fax +351-22-508 1446

✉ m.ec@fe.up.pt

Editado por

FACULDADE DE ENGENHARIA DA UNIVERSIDADE DO PORTO

Rua Dr. Roberto Frias, s/n

4200-465 PORTO

Portugal

Tel. +351-22-508 1400

Fax +351-22-508 1440

✉ feup@fe.up.pt

http://www.fe.up.pt

Aos meus Pais e Ao meu Avô Isaías

"Everybody should have a friend (…). Even a tree needs a friend."

Bob Ross

ACKNOWLEDGEMENTS / AGRADECIMENTOS

I hereby express my deepest acknowledgements to everyone that contributed directly or indirectly to the development and conclusion of this dissertation.

To my supervisors, Professor Cecília Vale and Dr Araliya Mosleh, I thank them for their exemplary orientation, dedication and kindness demonstrated during all the time I was working on this Dissertation, for pointing me in the right direction during my work, for being always present during the making of this Dissertation and sharing the knowledge needed in order to write an academic work of value. I apologise if I have not been the best student to work with at times, and I hope all this work we made can make up for those moments. I would also like to thank Dr Pedro Aires Montenegro for his availability in providing the models and algorithm essential for the making of this work.

I thank the members of the Way4SafeRail Project, for providing me with an opportunity to experience a researcher's world and the teamwork that accompanies it, a world of which I would like to continue being part of.

I thank all the professors of the Department of Civil Engineering of the Faculty of Engineering of the University of Porto, for giving me the basis of all the knowledge needed in order to become a Civil Engineer. A special thanks to Professor Isabel Ribeiro, for caring about all of her students, for her amazing work during my time as a Civil'IN mentor and for her work and dedication as the Erasmus Exchange Program Coordinator at the time: your dedication and help made it possible for me to experience a once-in-a-lifetime opportunity as a student at the amazing Katholieke Universiteit Leuven in Belgium. The semester I spent there was one of the best moments of my life, and your dedication made that happen.

Speaking of KU Leuven, I would like to thank everyone at Guido Gezelle Student Residence for the amazing semester we all shared, especially Anastasis, Juan Fran, Miguel, Miriam, Nerea, Teo and, of course, the "Tugas Gezelle" Leo, Mariana and Sofia, thank you all for the wonderful moments in Leuven.

To my Friends, André, João Abreu, João Carneiro, Luís Fernandes, Nuno: thank you all for your support, for being by my side all these years, years which I gathered amazing memories and companionship and that I wish I have provided the same for you all and that more incredible moments will come for many more years. To my Friends and University Colleagues, Bernardo, Dias, Duarte, Hélder, Henrique, João Pereira, Luís Miguel, Luís Sousa, Mafalda, Peixe, Rego, Rosário, Rui, Santos: I am so glad to have had the honour to share these years in this Institution with all of you, from which the memories created will be forever treasured. Thank you for becoming life-long friends and future work colleagues, and for being there for the good and bad times we all passed through and shared. Words cannot express how much you all mean to me. I am excited to join the many of you that have already started the next phase of our lives in the amazing world of a Civil Engineer (and of course other Engineering fields for those that graduated from the other houses at FEUP).

À minha Família, por todo o amor e apoio que me deram ao longo da vida. Aos meus avós, Alice, Ermelinda, António e Isaías, a quem esta Dissertação é em parte dedicada, ao meu tio Jorge, à minha Madrinha Estela, às minhas primas, Susana e Mariana, ao meu irmão Quirino, à minha cunhada Diana e à minha linda sobrinha e afilhada Carolina, um grande beijinho e um enorme obrigado a todos vós.

Agradeço em particular aos meus Pais, a quem também dedico esta Dissertação, por todo o amor e apoio que me deram ao longo da vida, pela educação que me deram e que fizeram de mim a pessoa que sou e

por todos os sacrifícios que passaram para que nunca me faltasse nada. Sem eles nunca teria conseguido chegar a este ponto no meu percurso académico. Por isso, mais uma vez, muito obrigado por tudo, pois este trabalho é vosso também.

ABSTRACT

The objective of this dissertation is to detect railway vehicle wheel flats and polygonised wheels using an envelope spectrum analysis. A brief explanation of railway vehicle wheel problems is presented, focusing particularly on wheel flats and polygonal wheels. Three types of wheel flat profiles and three Periodic out-of-roundness (OOR) harmonic order ranges for the polygonal wheels are evaluated in the simulations, along with analyses implemented using only healthy wheels for comparison. Also the simulation implements track irregularity profiles modelled based on the US Federal Railroad Administration (FRA). From the numerical calculations the dynamic responses of a number of strain gauges (SGs) and accelerometer sensors located on the rail between and on top of sleepers are evaluated. In terms of defected wheels, only the right wheel of the first wheelset is considered to have a OOR problem, but the detection methodology works for various defective wheels located in any position. The results from the application of the methodology show that the envelope spectrum analysis successfully distinguishes a healthy wheel from a defective one.

KEYWORDS: wheel out-of-roundness; numerical simulation; train–track interaction; validation; algorithm

RESUMO

O objetivo desta dissertação é detetar rodados com lisos rodado poligonizados de veículos ferroviários, através de análises com recurso a *envelope spectrum*. É apresentada uma breve explicação dos problemas dos rodados dos comboios, com particular foco nos lisos e no efeito de poligonalização. Nas simulações, são avaliados três tipos de perfis de rodados com lisos e três intervalos de ordem harmónica periódicas para os rodados poligonizados, juntamente com análises implementadas utilizando apenas rodados sem defeito para comparação. Também a simulação implementa perfis de irregularidade de via modelados com base na *Federal Railroad Administration* (FRA) dos EUA. A partir dos cálculos numéricos, são avaliadas as respostas dinâmicas de vários extensómetros e acelerómetros localizados no carril, por cima e entre as travessas. Em termos de rodados defeituosos, apenas o rodado direito do primeiro conjunto de rodados é considerado como tendo um defeito, mas a metodologia de deteção funciona para vários rodados defeituosos localizadas em qualquer posição. Os resultados da aplicação da metodologia mostram que a análise do *envelope spectrum* distingue com sucesso um rodado perfeito de um rodado defeituoso.

PALAVRAS-CHAVE: rodados com defeito; simulação numérica; interação comboio-carril; validação; algoritmo

GENERAL INDEX

ACKNOWLEDGEMENTS / AGRADECIMENTOS iii
ABSTRACT v
RESUMO vii

TABLE OF CONTENTS

1 INTRODUCTION 1
1.1. PERSONAL MOTIVATION 1
1.2. THESIS OBJECTIVES 1
1.3. THESIS ORGANISATION 2
2 LITERATURE REVIEW AND STATE OF THE ART 3
2.1. OUT-OF-ROUNDNESS PROBLEMS 3
2.1.1. WHEEL FLATS 6
2.1.2. WHEEL POLYGONIZATION 8
2.2. TECHNIQUES FOR OUT-OF-ROUNDNESS DETECTION 10
2.2.1. TECHNIQUES FOR WHEEL FLAT DETECTION 10
2.2.2. TECHNIQUES FOR PERIODIC WHEEL POLYGONIZATION IDENTIFICATION 26
3 NUMERICAL MODELLING 41
3.1. INTRODUCTION 41
3.2. CONSTITUENT ELEMENTS OF A RAILWAY TRACK 42
3.2.1. RAIL 42
3.2.2. SLEEPERS 43
3.2.3. FASTENING SYSTEMS 43
3.2.4. RAIL PADS 44
3.2.5. BALLAST BED 44
3.2.6. SUB-BALLAST 44
3.2.7. SUBGRADE 45
3.3. NUMERICAL TRACK MODEL 45
3.4. NUMERICAL TRAIN MODEL 49
3.5. TRAIN-TRACK INTERACTION 49
4 ALGORITHM FOR WHEEL OOR DETECTION 53
4.1. INTRODUCTION 53

4.2. METHODOLOGY FOR WHEEL DEFECT DETECTION 53

4.2.1. DEFINITION OF KURTOSIS 53

4.2.2. DETECTING A WHEEL DEFECT USING THE ENVELOPE SPECTRUM APPROACH 54

5 CASE STUDIES 57

5.1. INTRODUCTION 57

5.1.1. LAYOUT OF THE MULTI-SENSOR ARRAY OF THE MONITORING SYSTEM 58

5.1.2. WHEEL DEFECT GEOMETRY 59

5.2. WHEEL FLATS 61

5.2.1. WHEEL FLAT DETECTION BY THE RESPONSE OBTAINED FROM THE ACCELEROMETERS 62

5.2.2. RELATION BETWEEN WHEEL FLAT PROFILE, TRAIN SPEED AND MAXIMUM ACCELERATION PEAK AMPLITUDE 70

5.2.3. WHEEL FLAT DETECTION BY THE RESPONSE OBTAINED FROM THE STRAIN GAUGES 70

5.3. WHEEL POLYGONIZATION 77

5.3.1. RESPONSE OBTAINED BY ACCELEROMETERS 77

5.3.2. RESPONSE OBTAINED BY THE STRAIN GAUGES 80

5.3.3. RELATION BETWEEN POLYGONIZATION HARMONIC ORDERS, TRAIN SPEED AND MAXIMUM PEAK ACCELERATION AMPLITUDE 83

5.4. INFLUENCE OF ONE DEFECTIVE WHEEL IN THE TRACK 84

6 CONCLUSIONS 87

6.1. GENERAL CONCLUSIONS 87

6.2. FUTURE DEVELOPMENTS 88

BIBLIOGRAPHICAL REFERENCES 89

APPENDIX 97

FIGURES INDEX

Figure 2-1 - Modern wheelsets manufactured by KLW WheelCo. Taken from KLW WheelCo SA (2019) 3

Figure 2-2 - Schematics of a healthy wheel (in blue) and worn wheel (red) over a healthy rail (green). Taken from Shevtsov (2008) 4

Figure 2-3 - Non-periodic OOR detected from ICE train wheel in Germany. The bars display the distribution of the OOR shape's various harmonics. Taken from Nielsen & Johansson (2000) based on results from Pallgen (1998) 6

Figure 2-4 - Wheel flat formed by wheel–rail slip in the contact. Taken from Steenbergen (2008) 7

Figure 2-5 - Illustration of a newly wheel flat (left) and an advanced/rounded wheel flat (right). Adapted from Steenbergen (2008) 7

Figure 2-6 - Schematics of a wheel flat. r_w is the radius of the wheel, L is the wheel flat length and D is the flat depth 8

Figure 2-7 - Periodic OOR wheel with one, three, six and eight harmonic orders. Taken from Lan et al. (2019) 8

Figure 2-8 - Periodic OOR detected from ICE train wheel in Germany. The bars display the distribution of the OOR shape's various harmonics. Taken from Nielsen & Johansson (2000) based on results from Pallgen (1998) 9

Figure 2-9 - Defected wheel with polygonization. Taken from Jin et al. (2018) 9

Figure 2-10 - Schematic of the parallelogram mechanism. Taken from Gao et al. (2019) 11

Figure 2-11 - Waveform measurement of a wheel flat obtained by the parallelogram method in laboratory enviornment. Taken from Gao et al. (2019) 12

Figure 2-12 – Motion process of the mechanism parameters both before and after a thoughtful selection of the parameters for implementing the parallelogram mechanism in field conditions. Taken from Gao et al. (2019) 12

Figure 2-13 - Time domain (left) and frequency spectrum (right) of vibration signals at various speeds. Taken from Wang et al. (2020) 14

Figure 2-14 - Filtered envelope analysis of vibration signals. Taken from Wang et al. (2020) 15

Figure 2-15 - Schematic of a vehicle passing through the six pairs of SGs. Taken from Mosleh et al. (2020b) 16

Figure 2-16 - Frequency contents of shear obtatined for the 12 SGs for speed V=20 m/s: defective wheel with a flat, L = 150 mm and D = 1.5 mm (left); healthy wheel (right). Taken from Mosleh et al. (2020b) 16

Figure 2-17 - Envelope spectrum analysis for the 12 SGs for speed V=20 m/s: defective wheel with a flat, L = 150 mm and D = 1.5 mm (left); healthy wheel (right). Taken from Mosleh et al. (2020b) 17

Figure 2-18 - Envelope spectrum analysis for the 12 SGs with unevenness track profile: defective wheel with a flat (left); healthy wheel (right). Taken from Mosleh et al. (2020b) 17

Figure 2-19 - Schematic of the sensors locations with a vehicle passing with a wheel flat. Taken from Mosleh et al. (2021) 18

Figure 2-20 - Main signal obtained from strain gauge 9 from the passage of the *Alfa Pendular* vehicle (left) and corresponding spectral kurtosis, with K_{max} = 60.25 Hz, optimal window length = 16, center frequency = 0.1875 kHz, and bandwidth frequency = 0.125 kHz. Taken from Mosleh et al. (2021) 19

Figure 2-21 - Envelope spectrum analysis for the 12 SGs for the Alfa Pendular considering unevenness profile of the track, with a defective wheel (left), and a healthy wheel (right). Taken from Mosleh et al. (2021) 19

Figure 2-22 - Envelope spectrum analysis for the 12 Accelerometers between the sleepers for the Alfa Pendular considering unevenness profile of the track, with a defective wheel (left), and a healthy wheel (right). Taken from Mosleh et al. (2021) 20

Figure 2-23 - Envelope spectrum analysis for the 7 Accelerometers on top of the sleeper for the Alfa Pendular considering unevenness profile of the track and considering a noise intensity level in the signal of 10%, with a defective wheel (left), and a healthy wheel (right). Taken from Mosleh et al. (2021) 20

Figure 2-24 - Envelope Kurtosis values for healthy wheel and wheel flat for each SG sensor located on the track for the passage of the *Alfa Pendula*. Taken from Mosleh et al. (2021) 21

Figure 2-25 - Diagram of wheel tread defect diagnosis. The main modules above described are highlighted in shade of gray. Auxiliary modules Image Processing (IP), Cropping and Circunference Calculation (CC) are shown in white. Taken from Trilla et al. (2021) 22

Figure 2-26 - Diagram of the functional blocks of the proposed unified CNN, showing the feature and task learning stages. Taken from Trilla et al. (2021) 22

Figure 2-27 - Four layers utilised in the industrialised architecture of the wheel tread diagnosis framework. Taken from Trilla et al. (2021) 23

Figure 2-28 - Histogram of the defect location prediction error, with the uncertainty indicates by the 60% confidence interval Standard Deviation (SD). Taken from Trilla et al. (2021) 23

Figure 2-29 - Scheme of the measuring position during accoustic pass-by-tests. M1, M2 and M3 - Microphones; P - Photocells. Taken from Komorski et al. (2021) 25

Figure 2-30 - FFT sound pressure spectrum for tram speeds of 30 km/h (left) and 40 km/h (right). Red corresponds to wheel flat and blue corresponds to healthy wheel. Taken from Komorski et al. (2021) 26

Figure 2-31 - Spectrum of acoustic signal envelopes with the marked band of the first three rotational harmonic frequencies of the wheel for tram speed of 30 km/h (left) and 40 km/h (right). Red corresponds to wheel flat and blue corresponds to healthy wheel. Taken from Komorski et al. (2021) 26

Figure 2-32 - Diagram of the work principle of PVDF OOR detection method. Taken from Song et al. (2014) 27

Figure 2-33 - Relation between stress and vertical wheel/rail force. Taken from Song et al. (2014) 28

Figure 2-34 - Relation between curve slope and train speed. Taken from Song et al. (2014) 28

Figure 2-35 - Relation between curve slope and horizontal wheel/rail force. Taken from Song et al. (2014) 29

Figure 2-36 - Diagram of wheel non-circular detection method based on POVMD and mult-core LS-SVM. Taken from Fang et al. (2020) 30

Figure 2-37 - Results from wheel classification analyses. Taken from Fang et al. (2020) 30

Figure 2-38 – Diagram of the detection method for polygonised wheels based on dynamic response. Taken from Xu et al. (2020) 31

Figure 2-39 - Vehicle axle box acceleration. Taken from Xu et al. (2020) 32

Figure 2-40 - Power spectrum (left) and time-frequency diagram (right). Taken from Xu et al. (2020) 32

Figure 2-41 - Spectral envelope from the proposed method (left) and the traditional method (right). Taken from Xu et al. (2020) 33

Figure 2-42 - Roughness data of wheel surface: amplitude in polar coordinates (left); polygonization level (right). Taken from Xu et al. (2020) 33

Figure 2-43 - Schematic for the location of the vibration sensors. Taken from Huang et al. (2021) 34

Figure 2-44 - Vibration waves of healthy wheels. Taken from Huang et al. (2021) 34

Figure 2-45 - Vibration waves of incipient faults wheels. Taken from Huang et al. (2021) 35

Figure 2-46 - Vibration waves of serious faults wheels. Taken from Huang et al. (2021) 35

Figure 2-47 - Spectra display of normal signals. Taken from Huang et al. (2021) 36

Figure 2-48 - Spectra display of incipient faults signals. Taken from Huang et al. (2021) 36

Figure 2-49 - Spectra display of serious faults signals. Taken from Huang et al. (2021) 36

Figure 2-50 - Optimisation of the network using DBN. Taken from Huang et al. (2021) 38

Figure 2-51 - Diagram of the procedure of OOR defect diagnosis for the metro vehicle wheels. Taken from Huang et al. (2021) 38

Figure 2-52 - Graph of declining erros with each iteration for Test Six. Taken from Huang et al. (2021) 39

Figure 2-53 - Calculation accuracy with different epochs of Test Six. Taken from Huang et al. (2021) 39

Figure 3-1 - Elements and layers of a ballasted track. Taken from Phanyakit & Satiennam (2018) 42

Figure 3-2 - Rail profile types. Adapted from Esveld (2001) 43

Figure 3-3 - Examples of direct fastenings (left) and indirect fastenings (right). Taken from Sadeghi et al. (2020) 44

Figure 3-4 - Examples of track models: (**a**) 2D track mode, taken from Vale (2021); (**b**) 2.5D track model, taken from Costa (2011); (**c**) 3D track model, taken from Costa (2011) 46

Figure 3-5 - Track irregularity profiles for classes 3 to 8. Adapted from Gonçalves et al. (2023) 48

Figure 3-6 - Dynamic model of the railway vehicle lateral view (left) and front view (right). Taken from Mosleh et al. (2020b) 49

Figure 3-7 - Graphical representation of the the train-track interaction numerical model. Taken from Mosleh et al. (2022b) 51

Figure 4-1 – Diagram of the methodology for identifying a defective wheel 55

Figure 4-2 - Spectral kurtosis for a shear signal corresponding to the *Alfa Pendular* train, showing the maximum kurtosis, optimal window length, centre frequency, and bandwidth frequency 56

Figure 5-1 - Schematics of a train containing a defective wheel and the SG and Accelerometer sensors locations. Adapted from Gonçalves et al. (2023) 59

Figure 5-2 - Schematics of wheel polygonization with 2 harmonic orders (left), 3 harmonic orders (middle), and 4 harmonic orders (right). r_w is the radius of the wheel 61

Figure 5-3 - Scheme of the wheel flat impact areas within the track section, as well as the location of each sensor. X_i is the beginning of the track section, X_f is the end of the track section 62

Figure 5-4 - Envelope spectrum analyses for the 10 Accelerometers between the sleepers (layout scheme 2) for the *Alfa Pendular*, considering train speed ***V*=60 km/h** and *wf1* wheel flat profile: (**a**) class 3 track irregularity profile; (**b**) class 4 track irregularity profile; (**c**) class 5 track irregularity profile; (**d**) class 6 track irregularity profile; (**e**) class 7 track irregularity profile; (**f**) class 8 track irregularity profile; (**g**) control analyses with: train speed ***V*=60 km/h**, class 8 irregularity profile, and healthy wheel 64

Figure 5-5 - Envelope spectrum analyses for the 10 Accelerometers between the sleepers (layout scheme 2) for the *Alfa Pendular*, considering train speed ***V*=100** km/h and *wf1* wheel flat profile: (**a**) class 4 track irregularity profile; (**b**) class 5 track irregularity profile; (**c**) class 6 track irregularity profile; (**d**) class 7 track irregularity profile; (**e**) class 8 track irregularity profile; (**f**) control analyses with: train speed ***V*=100 km/h**, class 8 irregularity profile, and healthy wheel 65

Figure 5-6 - Envelope spectrum analyses for the 10 Accelerometers between the sleepers (layout scheme 2) for the *Alfa Pendular*, considering train speed ***V*=140 km/h** and *wf1* wheel flat profile: (**a**) class 6 track irregularity profile; (**b**) class 7 track irregularity profile; (**c**) class 8 track irregularity profile; (**d**) control analyses with: train speed ***V*=140 km/h**, class 8 irregularity profile, and healthy wheel 66

Figure 5-7 - Envelope spectrum analyses for the 10 Accelerometers between the sleepers (layout scheme 2) for the Alfa Pendular, considering train speed V=100 km/h and class 7 track irregularity profile: (**a**) ***wf1*** wheel flat profile; (**b**) ***wf2*** wheel flat profile; (**c**) ***wf3*** wheel flat profile; (**d**) control analyses with: train speed *V*=100 km/h, class 7 irregularity profile, and **healthy wheel**; (**e**) control analyses with: train speed *V*=100 km/h, class 8 irregularity profile, and **healthy wheel** 68

Figure 5-8 - Comparison between envelope spectrum analyses for the Accelerometers located on the sleepers (layout scheme 3) and for the Accelerometers located between the sleepers (layout scheme 2) for the Alfa Pendular, considering train speed V=100 km/h and class 7 track irregularity profile: (**a**) **layout 3** and *wf2* wheel flat profile; (**b**) **layout 2** and *wf2* wheel flat profile; (**c**) control analyses from **layout 3** with: train speed V=100 km/h, class 7 irregularity profile, and healthy wheel; (**d**) control analyses from **layout 2** with: train speed V=100 km/h, class 7 irregularity profile, and healthy wheel 69

Figure 5-9 - Relation between train speed, *V*, wheel flat profile and maximum peak amplitude obtained from the Accelerometers (layout scheme 2) responses, using class 7 track irregularity profile 70

Figure 5-10 - Envelope spectrum analyses for the 10 SGs (layout scheme 1) for the *Alfa Pendular*, considering train speed ***V*=60 km/h** and *wf1* wheel flat profile: (**a**) class 3 track irregularity profile; (**b**) class 4 track irregularity profile; (**c**) class 5 track irregularity profile; (**d**) class 6 track irregularity profile; (**e**) class 7 track irregularity profile; (**f**) class 8 track irregularity profile; (**g**) control analyses with: train speed ***V*=60 km/h**, class 8 irregularity profile, and healthy wheel 72

Figure 5-11 - Envelope spectrum analyses for the 10 SGs (layout scheme 1) for the *Alfa Pendular*, considering train speed ***V*=100 km/h** and *wf1* wheel flat profile: (**a**) class 4 track irregularity profile; (**b**) class 5 track irregularity profile; (**c**) class 6 track irregularity profile; (**d**) class 7 track irregularity profile; (**e**) class 8 track irregularity profile; (**f**) control analyses with: train speed ***V*=100 km/h**, class 8 irregularity profile, and healthy wheel 73

Figure 5-12 - Envelope spectrum analyses for the 10 SGs (layout scheme 1) for the *Alfa Pendular*, considering train speed *V*=**140 km/h** and *wf1* wheel flat profile: (**a**) class 6 track irregularity profile; (**b**) class 7 track irregularity profile; (**c**) class 8 track irregularity profile; (**d**) control analyses with: train speed ***V*=140 km/h**, class 8 irregularity profile, and healthy wheel 74

Figure 5-13 - Envelope spectrum analyses for the 10 SGs (layout scheme 1) for the *Alfa Pendular*, considering train speed *V*=140 km/h and class 7 track irregularity profile: (**a**) ***wf1*** wheel flat profile; (**b**) ***wf2*** wheel flat profile; (**c**) ***wf3*** wheel flat profile; (**d**) control analyses with: train speed *V*=140 km/h, class 7 irregularity profile, and **healthy wheel**; (**e**) control analyses with: train speed *V*=140 km/h, class 8 irregularity profile, and **healthy wheel** 76

Figure 5-14 - *Wf1* profile showing the location of the flat impacts (blue line). The red lines indicate the length of the track section in study where the sensors were installed 76

Figure 5-15 - Envelope spectrum analyses for the 10 accelerometers (layout scheme 2) for the *Alfa Pendular*, considering class 7 track irregularity profile and polygonised wheel with *wp12*: (**a**) train speed ***V*=60 km/h**; (**b**) train speed ***V*=80 km/h**; (**c**) train speed ***V*=100 km/h**; (**d**) train speed ***V*=140 km/h**; (**e**) control analyses with: train speed ***V*=100 km/h**, class 7 track irregularity profile, and healthy wheel .. 78

Figure 5-16 - Envelope spectrum analyses for the 10 Accelerometers (layout scheme 2) for the *Alfa Pendular*, considering class 7 track irregularity profile and train speed *V*=100 km/h: (**a**) polygonised wheel profile ***wp5***; (**b**) polygonised wheel profile ***wp12***; (**c**) polygonised wheel profile ***wp20***; (**d**) control analyses with: train speed *V*=100 km/h, class 7 track irregularity profile, and **healthy wheel** 80

Figure 5-17 - Envelope spectrum analyses for the 10 SGs (layout scheme 1) for the *Alfa Pendular*, considering class 7 track irregularity profile and polygonised wheel profile *wp12*: (**a**) train speed ***V*=60 km/h**; (**b**) train speed ***V*=80 km/h**; (**c**) train speed ***V*=100 km/h**; (**d**) train speed ***V*=140 km/h**; (**e**) control analyses with: train speed ***V*=100 km/h**, class 7 track irregularity profile, and healthy wheel 82

Figure 5-18 - Envelope spectrum analyses for the 10 SGs (layout scheme 1) for the *Alfa Pendular*, considering class 7 track irregularity profile and train speed *V*=100 km/h: (**a**) polygonised wheel profile ***wp5***; (**b**) polygonised wheel profile ***wp12***; (**c**) polygonised wheel profile ***wp20***; (**d**) control analyses with: train speed *V*=100 km/h, class 7 track irregularity profile, and **healthy wheel** 83

Figure 5-19 - Relation between train speed, *V*, OOR harmonic order and maximum peak amplitude obtained from the accelerometers (layout scheme 2) responses, using class 7 track irregularity profile 84

Figure 5-20 - Comparison of envelope spectrum analyses for the 10 Accelerometers (layout scheme 2) for the *Alfa Pendular*, considering “class 7” track irregularity profile and train speed *V*=140 km/h: (**a**) *wf2* wheel flat profile measured on the **right side** of the track; (**b**) *wf2* wheel flat profile measured on the **left side** of the track; (**c**) control analyses with a healthy wheel, measured on the **right side** of the track; (**d**) control analyses with a healthy wheel, measured on the **left side** of the track..... 85

TABLES INDEX

Table 2-1 - SNR of vibration signals without denoise and extracting principle principal component. Values from Huang et al. (2021) 34

Table 3-1 - Mechanical properties of the track. Values from Mosleh et al. (2020b) 47

Table 3-2 - Roughness parameter for the FRA track classes. Values from Mosleh et al. (2020a) 48

Table 5-1 - Geometrical and mechanical properties of the *Alfa Pendular* train. Values from Mosleh et al. (2020b; 2021) 57

SYMBOLS AND ABBREVIATIONS

Chapter 2

Abbreviations

ADAMS – Automated Dynamic Analysis of Mechanical Systems

B&K – Brüel & Kjaer

CC – Cropping and Circumference calculation

CI – Confidence Index

CNN – Convolutional Neural Network

DBN – Deep Belief Network

DC – Defect Classification

DD-Loc – Defect Detection - Location

DD-Phy – Defect Detection - Physical size

EA – Engineering Assessment

EMI – Electromagnetic Interference

FASTSIM – Future Automotive Systems Technology Simulator

FFT – Conventional Power Spectral Analysis

FRA – Federal Railroad Administration

ICE – German Intercity-Express high-speed train service

IMFs – Intrinsic Mode Functions

IP – Image Processing

KPCA – Kernel Principal Component Analysis

KPCA-DBN – Kernel Principal Component Analysis applied with Deep Belief Network

LIM – Linear Induction Motor

LS-SVM - Multicore Core Least Square Support Vector Machine

MAX – maximum

MBS – Multi-body System

OOR – Out-of-Roundness

POVMD – Parameter Optimisation

PSO – Particle Swarm Optimisation

PVDF – Polyvinylidene Difluoride

RGB – Red-Green-Blue colour model

RMS – Root Mean Square value

SD – Standard Deviation

SG – Strain Gauge

SNR – Signal-to-Noise Ratio

SSTFT – Synchrosqueezed Short-Time Fourier Transform

STFT – Short-Time Fourier Transform

VMD – Variational Mode Decomposition

Symbols

D – Depth of wheel flat [mm]

K – Kurtosis

K_{max} – Maximum Kurtosis

L – Length of wheel flat [mm]

V – Speed [km/h]

f_{fp} – Wheel surface damage

r_w – Wheel radius [m]

Chapter 3

Abbreviations

54E1(UIC 54) – Rail profile 54E1 (UIC54)

60E1(UIC 60) – Rail profile 60E1 (UIC60)

Fes – Finite Element Simulation

FRA – Federal Railroad Administration

VSI – Vehicle Structure Interaction Dynamic Analysis

Symbols

$S(K_1)$ – Generated track unevenness profile

a, – Longitudinal distance between wheelsets [m]

b – Transversal distance between vertical suspensions [m]

c – Damping of the train [N s/m]

h – Vertical distance [m]

I – Rotational inertia of the train [kg m^2]

k – Stiffness of the train [N/m]

m – Mass of the train [kg]

R_0 – Nominal wheel radius [m]

s – Gauge [mm]

Chapter 4

Abbreviations

SGs – strain gauges

Symbols

D – Wheel flat depth [m]

F_s – Sampling frequency [Hz]

H – Heaviside function

K - Kurtosis

L – Wheel flat length [m]

L_w – Wheel irregularity level spectrum [dB re 1 μm]

V – Train speed [m/s]

Z – Wheel flat vertical deviation

f_f – Flat impact frequency [Hz]

f_0 – Centre frequency

i – Number of filters applied at level l

l – Level of the coefficient series

r_w – Radius of the wheel [m]

$w(x_w)$ – Irregularity profile

$\widehat{w}$ – Root mean square value of the irregularity profile

θ – Integer harmonic order

λ_θ – Wheel polygonization wavelengths

Δf – Bandwidth [Hz]

Chapter 5

Abbreviations

wf1 – Wheel flat profile with L=20 mm and D = 0.58 mm

wf2 – Wheel flat profile with L=80 mm and D = 0.93 mm

wf3 – Wheel flat profile with L=140 mm and D = 2.80 mm

wp5 – Polygonised wheel profile with a periodic harmonic order of 5

wp12 – Polygonised wheel profile with a periodic harmonic order of 12

wp20 – Polygonised wheel profile with a periodic harmonic order of 20

Symbols

$C_{1,z}$ – Damping of the primary vertical suspension [N s/m]

$C_{2,x}$ – Damping of the secondary longitudinal suspension [N s/m]

$C_{2,y}$ – Damping of the secondary transversal suspension [N s/m]

$C_{2,z}$ – Damping of the secondary vertical suspension [N s/m]

$I_{b,x}$ – Bogie roll moment of inertia [kg m^2]

$I_{b,y}$ – Bogie pitch moment of inertia [kg m^2]

$I_{b,z}$ – Bogie yaw moment of inertia [kg m^2]

$I_{cb,x}$ – Car body roll moment of inertia [kg m^2]

$I_{cb,y}$ – Car body pitch moment of inertia [kg m^2]

$I_{cb,z}$ – Car body yaw moment of inertia [kg m^2]

$I_{w,x}$ – Wheelset roll moment of inertia [kg m^2]

$I_{w,z}$ – Wheelset yaw moment of inertia [kg m^2]

R_0 – Nominal wheel radius [m]

V – Train speed [km/h]

a_1 – Longitudinal distance between bogies [m]

a_2 – Longitudinal distance between wheelsets [m]

b_1 – Transversal distance between vertical secondary suspensions [m]

b_2 – Transversal distance between longitudinal secondary suspensions [m]

b_3 – Transversal distance between primary suspensions [m]

f_f – Flat impact frequency [Hz]

h_1 – Vertical distance between car body centre and secondary suspension [m]

h_2 – Vertical distance between bogie centre and secondary suspension [m]

h_3 – Vertical distance between bogie centre and wheelset centre [m]

$k_{1,x}$ – Stiffness of the primary longitudinal suspension [N/m]

$k_{1,y}$ – Stiffness of the primary transversal suspension [N/m]

$k_{1,z}$ – Stiffness of the primary vertical suspension [N/m]

$k_{2,x}$ – Stiffness of the secondary longitudinal suspension [N/m]

$k_{2,y}$ – Stiffness of the secondary transversal suspension [N/m]

$k_{2,z}$ – Stiffness of the secondary vertical suspension [N/m]

m_b – Bogie mass [kg

m_{cb} – Car body mass [kg]

m_w – Wheelset mass [kg]

r_w – Radius of the wheel [m]

s – Gauge [m]

1 INTRODUCTION

1.1. PERSONAL MOTIVATION

The motivation for this dissertation has as a fundamental principle the will to participate and contribute in a proactive way in the research of topics in my area of training, as a Master's student of Civil Engineering in the area of Territorial Planning and Transports, of the Faculty of Engineering of the University of Porto.

I view the topic as motivating and energizing research since it contributes to the study and analysis of railway safety and efficiency, which is crucial for high-speed rail transport, which has seen significant growth in recent years in the European context and is expected to be implemented on the same level in the coming years in Portugal because of the safety, speed, convenience and opportunities it offers.

1.2. THESIS OBJECTIVES

Detecting and identifying wheel defects is one of the major challenges of railway transport. Defects create discomfort to passengers, generate wear and tear on nearby infrastructure, and if severe enough, can lead to service interruptions and train derailments. Therefore, it is necessary to monitor train wheels in order to prevent these incidents and to intervein in repairs before causing bigger problems. There are different types of railway wheel defects that originate from different sources.

In this dissertation, two types of wheel defects have been analysed: wheel flats and wheel polygonization. Moreover, a variety of monitoring and detection methods for these types of wheel defect have been researched and implemented over the last couple of decades, either *in situ* or recurring to computational simulation and modelling.

For this work, an algorithm developed by Mosleh et al. (2020b; 2021) in MATLAB® (2018) is implemented in order to analyse the existence of wheel flats and polygonised wheels. The numerical modelling of the vehicle, based on an *Alfa Pendular* train used in the Portuguese Railway Network, and the railway track, based on a straight section of the Portuguese Northern Line, were simulated in ANSYS® (2018) before being imported into MATLAB® (2018) to perform the analyses. This algorithm simulates a detection technique that can be implemented later *in situ*. A number of scenarios will be analysed, combining different train speeds, track unevenness profiles and wheel defect profiles.

In the analysis of wheel flats, three different profiles are taken into account. For the analysis of polygonised wheels, the wavelength of this type of defect ranges from 14 cm to the whole circumference of the wheel, while its amplitude is usually less than 1 mm (Nielsen & Johansson, 2000).

The objective is to determine the influence of the damage severity for both wheel flat and polygonised wheel in the detection algorithm compared to healthy wheel. It is expected that the algorithm detects major changes from a healthy wheel from a defective one. The results of this research study show that the detection method can potentially be implemented in the real case scenario in order to monitor train wheel defects.

1.3. THESIS ORGANISATION

This dissertation was divided into six chapters.

Chapter 1 – Introduction, presents the theme of this work, as well as its objectives.

Chapter 2 – Literature Review and State of the Art, introduces the problems of out-of-roundness found in railway vehicle wheels, with focus on wheel flats and periodic wheel polygonization, and presents some techniques utilised for out-of-roundness detection.

Chapter 3 – Numerical Modelling, presents a description of a ballasted railway track and its components, followed by a description of the numerical modelling for the train, the track, and the train-track interaction.

Chapter 4 – Algorithm for OOR Identification, describes the algorithm utilised for wheel defects detection and its methodology, as well as explaining the geometry and modelling of a wheel flat and a polygonised wheel profiles.

In *Chapter 5 – Study Cases*, the results from the analyses are presented, along with commentary on the results.

Finally, in *Chapter 6 – Conclusions*, the main conclusions from the study are presented, along with development perspectives for future studies.

2
LITERATURE REVIEW AND STATE OF THE ART

This Chapter presents: i.) a literature review on wheel out-of-roundness problems in trains, with a focus on wheel flats and wheel polygonization; and ii.) the state of the art of various techniques utilized in order to identify out-of-roundness in train wheels.

2.1. OUT-OF-ROUNDNESS PROBLEMS

Since the mid-18th century rail-based vehicles have been used flanged iron wheels on top cast-iron rails. By the mid-19th century, where railway lines had already appeared in the United Kingdom, coned wheels with flangeway clearance were already widely used (Lewis & Olofsson, 2009). This is the basis on which modern train wheels are modelled after. An example of modern wheelset is illustrated in Figure 2-1. When the train is moving, the coned steel wheels on the iron rails create less friction and generate less energy, thus prolonging the life of the wheel.

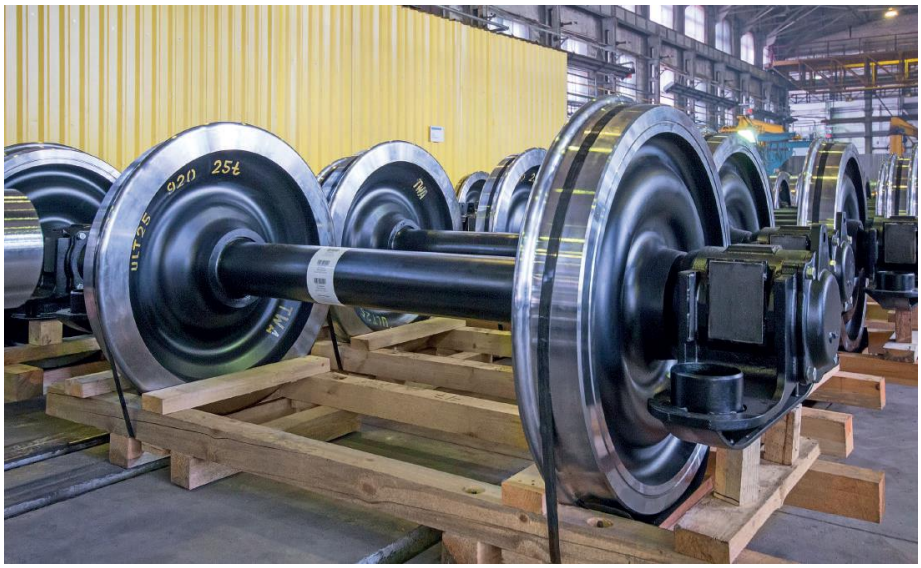

Figure 2-1 - Modern wheelsets manufactured by KLW WheelCo. Taken from KLW WheelCo SA (2019)

Railway developments in the 19th and 20th centuries allowed the usage of longer, heavier and faster trains to travel on railway networks across the world. This development has undoubtedly improved rail transport for both passengers and freight, but it has also caused additional pressure on both the railway tracks and the train wheels. Since the 1980s, the advent of new computer-based technology for numerical simulations, communication systems, control systems and data acquisition systems, has improved the monitoring and maintenance of railways at various levels, including train-track interactions. Nonetheless, in many cases, such as those related to in-depth simulation and analysis of wheel-track interactions, the computational capacity and speed required for those analyses are still limited by current technology (Lewis & Olofsson, 2009).

The factors mentioned above, such as larger trains, higher travel speeds and higher axle loads, combined with higher usage of railway transport, weather-related phenomena and, in many cases, reliance on older railway infrastructure, lead to more pressure on railway tracks and associated infrastructures, as well as on the train wheels themselves.

In the case of train wheels, there are several reasons that lead to defects (Rode et al., 1997). For example, in the surface layer or at subsurface locations, usually 5–25 mm below the surface, the contact stresses can lead to rolling contact fatigue (RCF) (Lewis & Olofsson, 2009). A wheel's out of roundness (OOR) might result from plasticization (Lewis & Olofsson, 2009). Wear mechanisms may cause OOR, a hollow tread, or, a thin flange as can be seen in Figure 2-2. Wheel material may change thermally with slight wheel slippage, leading to surface cracks that may enlarged by forces of contact. The residual surface material may undergo a phase change as a result of the wheel sliding, and wheel flats resulting in extremely strong contact forces may also develop (Lewis & Olofsson, 2009).

The block-wheel interaction in a block braked wheel can cause serious damage, such as thermal cracks in the tread or OOR. The brakes can overheat the entire wheel rim, and after cooling, residual tensile forces in the circumferential direction can lead to global wheel breakage (Lewis & Olofsson, 2009).

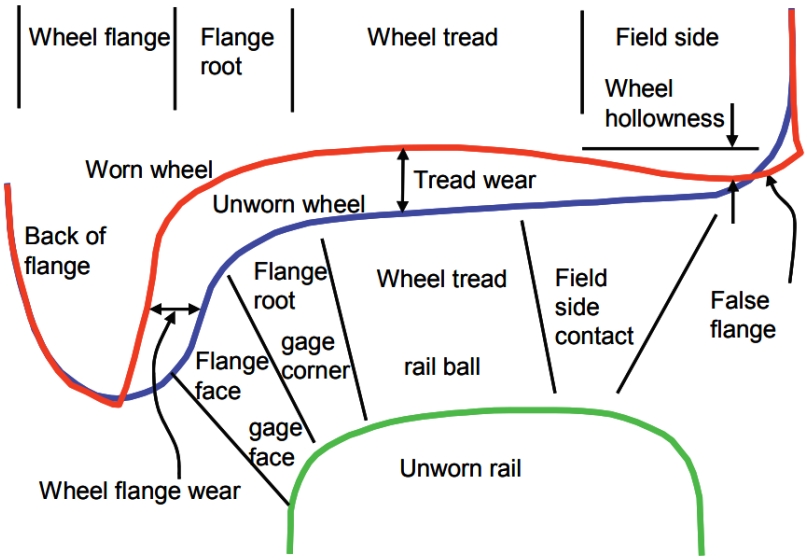

Figure 2-2 - Schematics of a healthy wheel (in blue) and worn wheel (red) over a healthy rail (green). Taken from Shevtsov (2008)

In terms of train wheel OOR, the work of Nielsen & Johansson (2000) categorized various types of OOR defects and wheel irregularities observed in the field including:

- Eccentricity: derived from misalignment of the fixation of the wheel during profiling or reprofiling;
- Discrete defect: slight deviation in the wheel radius that affects only part of the tread. Inhomogeneous characteristics of materials or wheel flats can lead to these changes. This wheel defect is often associated with plastic deformation;
- Flats: this type of defect is caused by the wheel slipping (instead of rolling) along the rail, which is caused by the friction between the wheel and the rail due to the braking force. Wheel flats are exposed in more detail in section 2.1.1;
- Periodic non-roundness: characterised by a constant wheel radius and a periodic irregularity around the circumference. The irregularity has an amplitude of around 1 mm and a wavelength that varies from 14 cm to a wheel circumference. Periodic OOR is explained in more detail in section 2.1.2;
- Non-periodic or stochastic non-roundness: inhomogeneous material properties of the wheel or unbalances in the wheelset could be to blame for this sort of OOR. On ICE wheels in Germany, stochastic OOR has been discovered (Pallgen, 1998). Figure 2-3 demonstrates a non-periodic OOR, along with the OOR's wavelength composition. It is clear from the figure that the stochastic shape incorporates a variety of harmonics through the wheel radius;
- Corrugation: wheel treads with block brakes exhibit this defect. This form of OOR has a circumferential wavelength that dominates between 3 and 6 cm, although its amplitude is less than 10 μm. Works made by Vernersson (1999b, 1999a) and Vernersson & Järnvägsmekanik (1996) have conducted theoretical and experimental research (numerical simulations) on the emergence of this particular flaw. The idea is that, during block braking, some areas of the tread on the wheel become warmer than adjacent areas. Due to thermal expansion, the heated areas protrude from the wheel surface and experience more wear than the rest of the tread surface. The volume of material in these hot spots reduces as the wheel cools down, forming valleys and creating a wavy pattern. It is known that one of the main causes of rolling noise is corrugation;
- Roughness: this type of defect has a circumferential wavelength in the range of 1 mm and an amplitude in the range of 10 μm;
- Spalling: a rolling contact fatigue phenomenan that occurs when thermally generated surface fractures collide and cause part of the wheel to separate from the tread. Hard brittle martensite that forms as a result of rapid heating and cooling of the wheel tread during and after block braking may develop thermal cracks;
- Shelling: typically used to describe all forms of subsurface-induced cracks. It manifests as the loss of material from the wheel tread. This particular type of rolling contact fatigue is mostly caused by excessive vertical wheel/rail contact forces relative to the wheel diameter.

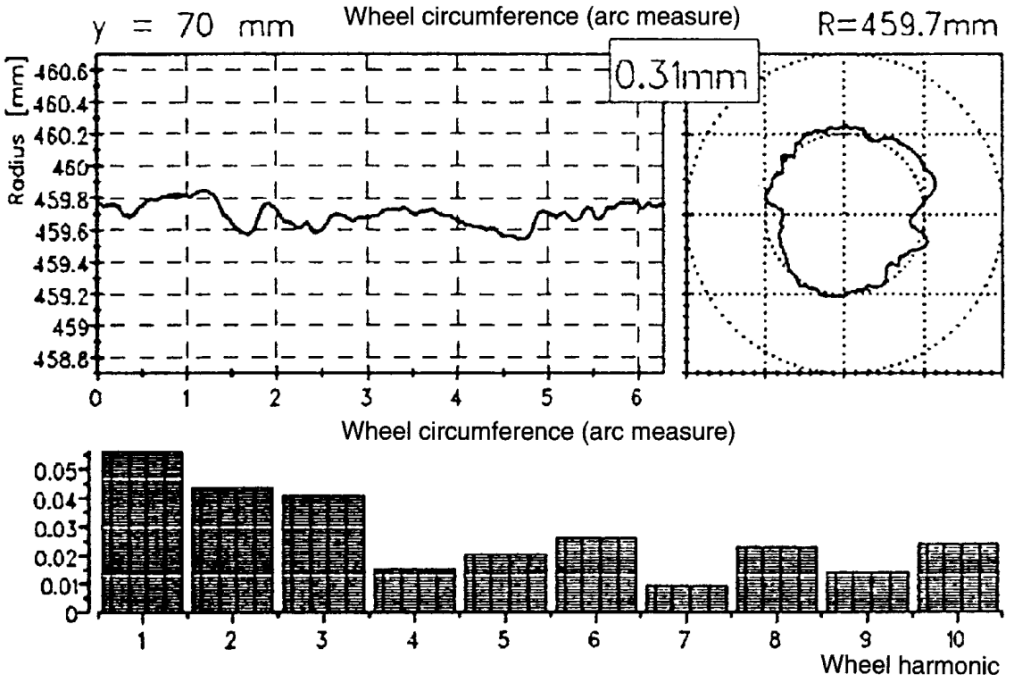

Figure 2-3 - Non-periodic OOR detected from ICE train wheel in Germany. The bars display the distribution of the OOR shape's various harmonics. Taken from Nielsen & Johansson (2000) based on results from Pallgen (1998)

In this dissertation, the algorithm implemented for wheel defects detection focus on two types of wheel OOR: wheel flats and wheel polygonization (periodic non-roundness). These types of OOR, introduced above, are further explained in subsections 2.1.1 and 2.1.2, respectively.

2.1.1. WHEEL FLATS

The wheel flat, as a local OOR defect, may have an adverse impact on the train-track systems and its occupants, as well as residents living near the tracks. The high-frequency vibration generated by wheel-flats disturbs the passenger comfort (Ye et al., 2020), as well as causes damage to infrastructure i.e., rails, sleepers and vehicle components i.e., bearings, axles, wheel sets, significantly reduces their useful lives and raising the possibility of derailment, as stated by Jergéus et al. (1999), Bogdevicius et al. (2016), and Wu et al. (2018). In addition, wheel flats lead to increased energy consumption and maintenance expenses (Ye et al., 2020).

Figure 2-4 depicts an illustration of a wheel flat created by abrasion. Previous researchers considered two types of flat wheel geometries in their studies as described in Figure 2-5. The newly formed flat wheel with sharp edges occurs immediately after the formation of the flat. In practice, due to wheel tread abrasion and continued wheel running after flat formation, the corners become rounded, whereas the central part remains unchanged. Several researchers have studied wheel flat detection and wheel condition estimation, such as Ahlström & Karlsson (1999), Jergéus et al. (1999), Snyder et al. (2003), Steenbergen (2008), and Mosleh et al. (2020b; 2021; 2022a, 2022b).

Figure 2-4 - Wheel flat formed by wheel–rail slip in the contact. Taken from Steenbergen (2008)

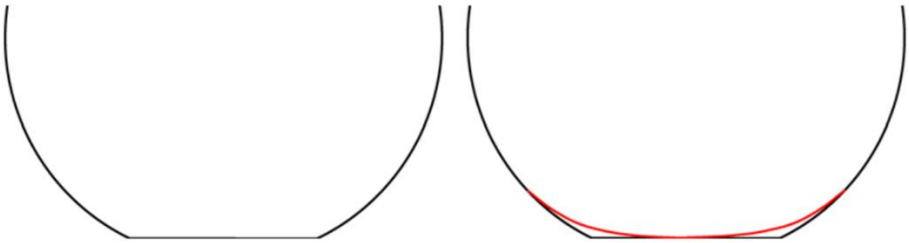

Figure 2-5 - Illustration of a newly wheel flat (left) and an advanced/rounded wheel flat (right). Adapted from Steenbergen (2008)

Wheel flats generate a high-import face that affects the train-track interaction, producing high rolling noise levels and worsening the service life for both the wheel and the nail, as well as spoiling the quality of the train ride, whether it is a passenger or a freight train service.

Figure 2-6 illustrates wheel flat properties clearly including flat length (L), the wheel flat depth (D), and the radius of the wheel (r_w). The numerical modelling of both these properties is described in Chapter 5.

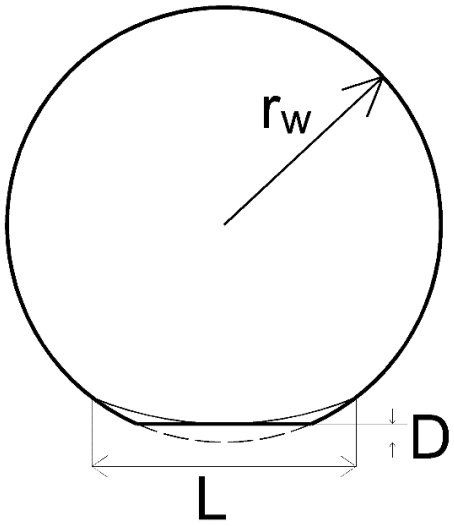

Figure 2-6 - Schematics of a wheel flat. r_w is the radius of the wheel, L is the wheel flat length and D is the flat depth

2.1.2. WHEEL POLYGONIZATION

In the train wheels, one of the most common non-uniform wear is a polygonal defect of non-circular periodic rotation. (Snyder et al., 2003). Periodic OOR, also known as the periodic deviation (single or multiple) deviations of the wheel diameter over the entire circumference of the wheel. The number of such deviations is known as the *repetition order*. The deviation may occur at a single point or various spots around the circumference of the wheel (Lan et al., 2019). Figure 2-7 shows a schematic of a periodic OOR wheel having one, three, six and eight harmonic orders, for a defect amplitude of 0.5 mm. Figure 2-8 displays a periodic OOR wheel detected on an ICE train in Germany, described by Nielsen & Johansson (2000) based on the works implemented by Pallgen (1998).

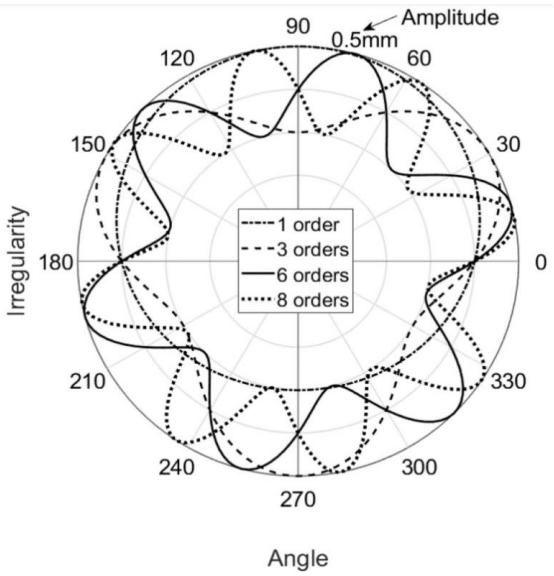

Figure 2-7 - Periodic OOR wheel with one, three, six and eight harmonic orders. Taken from Lan et al. (2019)

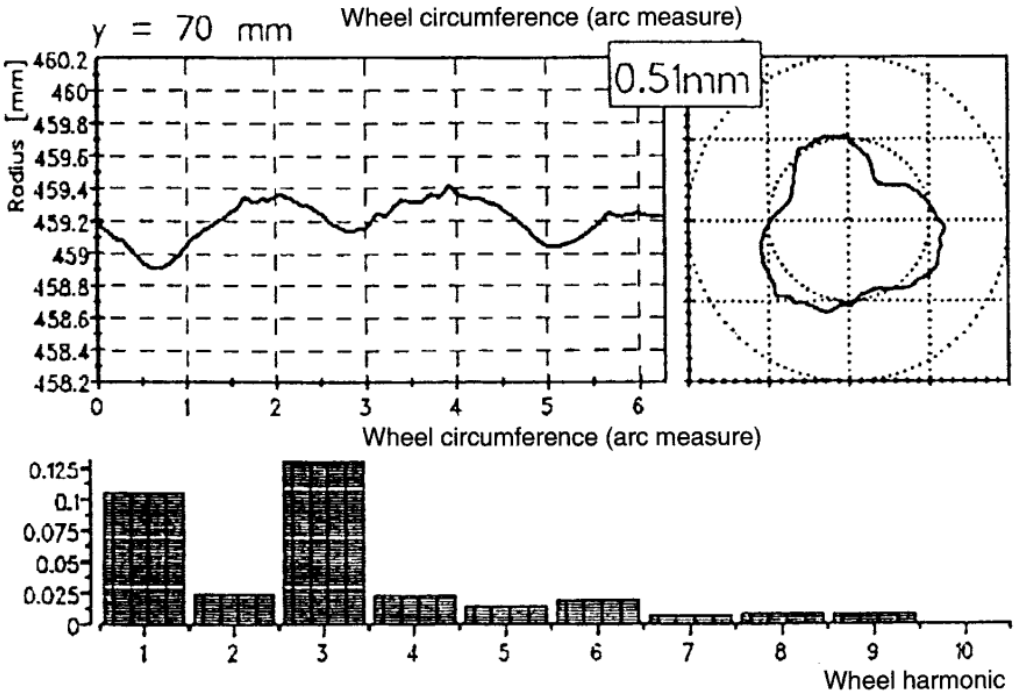

Figure 2-8 - Periodic OOR detected from ICE train wheel in Germany. The bars display the distribution of the OOR shape's various harmonics. Taken from Nielsen & Johansson (2000) based on results from Pallgen (1998)

This defect, similar to the effects caused by wheel flats, described above in subsection 2.1.1, can damage vehicle-track systems, as exposed in Iwnicki (2006) and Jin et al. (2012). Figure 2-9 shows an example of a wheel affected by periodic polygonization.

Figure 2-9 - Defected wheel with polygonization. Taken from Jin et al. (2018)

Wheel OOR polygonization mechanics has been studies intensively over the last few decades. It is a complex subject, with many parts related to the mechanisms of wheel polygonization and its influence in train-track systems not perfectly explained yet (Ye et al., 2020). In the work of Ye et al. (2020) many of these studies are mentioned, including:

- The work of Müller & Diener (1995) conducted on the Gotthard line, claimed that periodic OOR phenomenon can be caused by non-uniform material qualities across the wheel circumference;
- In the research of Rode et al. (1997) it was reported that the fixation could cause the third-order polygonal shape to emerge during the grinding operation (claw clamping);
- The work of Morys (1999) indicated that variations in normal forces at high speeds may be caused by wheel radius deviations or wheel mass eccentricities that occurs during manufacturing or re-profiling process, which would create a high level of vertical acceleration for the wheel and even excite the bending oscillation of the wheelset axle;
- The works conducted in Meinke & Meinke (1999) evaluated wheel tread polygonisation on high-speed trains caused by static and dynamic imbalances;
- The investigation conducted in Jin et al. (2012) stated that the first bending of the wheelset was the primary cause of the 9th order polygonal wear based on on-site observations and extensive experimentation of linear induction motor (LIM) metro trains;
- The research of Ma et al. (2016) investigated the mechanism causing polygon-shaped wheels to originate, based on a MBS model of a LIM-powered subway train, and discovered that over the course of several full wheel revolutions, a low-frequency vibration between the wheel and rail might result in the wheel polygon;
- The research presented in Peng et al. (2018) noted that the track imperfections and sleeper passing frequency could trigger the wheel polygonization with appropriate orders using the FASTSIM-Archard wear calculation;
- In the work of Zhao et al. (2019) the eigenvalue method to analyse a wheelset-track system model was used and suggested that the system's unstable vibration frequency was 495.01 Hz, which might cause 18th order wheel polygonal wear. The field measurement were roughly in agreement with the simulation result. It further claimed that the wheel polygonal wear was significantly influenced by the dampening of the fastener and wheelset eccentricity.

Johansson & Andersson (2005) presents a number of equations in order to define wheel polygonization. For this work, harmonic orders between 1 to 20 were considered.

2.2. Techniques for Out-of-roundness Detection

Over the last decades many studies were conducted in order to better identify railway wheel OOR. In this section, the state of the art in wheel OOR detection techniques is presented. In subsection 2.2.1 techniques developed and implemented for wheel flat detection are presented, and in subsection 2.2.2 methods for periodic wheel polygonization detection are described.

2.2.1. Techniques for Wheel Flat Detection

In recent years, many methods were developed to detect wheel flats (Mosleh et al., 2022a; 2022b, 2022c; Gonçalves et al., 2023). In this dissertation, the methods presented for wheel flat detection are:

- Parallelogram Mechanism Method (Gao et al., 2019);

- Vibration-Based Detection using Envelope Analysis (R. Wang et al., 2020);
- Wayside Monitoring System using Envelope Spectrum Analysis (Mosleh et al., 2020b);
- Wheel Flat Detection with Multiple Records using Spectral Kurtosis Analysis (Mosleh et al., 2021);
- Detection and Evaluation of Wheel Tread Images using Convolution Neural Networks (Trilla et al., 2021);
- Advanced Acoustic Signal Analysis for Wheel Flat Detection (Komorski et al., 2021).

Parallelogram Mechanism Method

The work of Gao et al. (2019) proposed a method for wheel flat detection based on a parallelogram mechanism. For this method, the main component of the wheel flats dynamic measurement system is a parallelogram mechanism, which consists of a limit block, an eddy current sensor, hydraulic damper, connecting rods, and springs, as can be demonstrated in Figure 2-10.

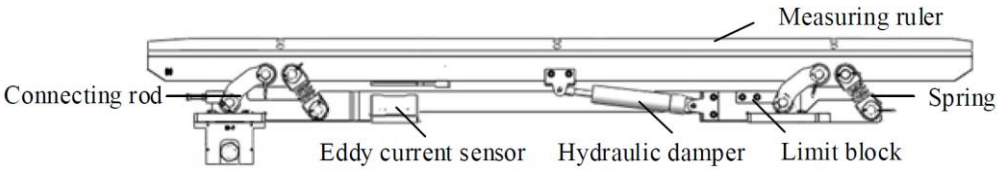

Figure 2-10 - Schematic of the parallelogram mechanism. Taken from Gao et al. (2019)

The upper plate (or measuring ruler) of the parallelogram mechanism is pressed down by the wheel as a train passes by the measuring device, and the eddy current sensor measures the vertical distance between the sensor and the measuring ruler. The vertical displacement of the detection signal does not change if the wheel being tested is a standard wheel. If there is a flat on the measured wheel tread, the detection signal will shift lower at the flat point, and the flat wheel will move vertically. The eddy current sensor may provide a downward displacement signal due to the contact between the parallelogram mechanism and the wheel, and the maximum vertical displacement corresponds to the depth of the wheel flat. To calculate the wheel flat length the following equation is used:

$$L = 2\sqrt{2r_w D - D^2} \quad (1)$$

in which:

- L, is the wheel flat length;
- D, is the maximum wheel flat depth;
- r_w, is the wheel radius.

Additionally, by contrasting the worn wheel with the normal one, the wear depth of the worn wheel may be determined.

To enhance the system performance, a 3D rigid-flexible coupled model of the measurement mechanism was created using the ADAMS dynamics modelling software. The wheel, rail, and the parallelogram mechanism, with the exception of the measuring ruler, were built up in the model as rigid bodies. The two main influencing elements on measurement were the deformation of the measuring ruler and its impact vibration. The deformation of the measurement mechanism may be examined using the

simulation model and compared with the experiment. To determine the threshold value of the measuring ruler's vibration speed, it was also necessary to check the movement of the measuring ruler at different speeds.

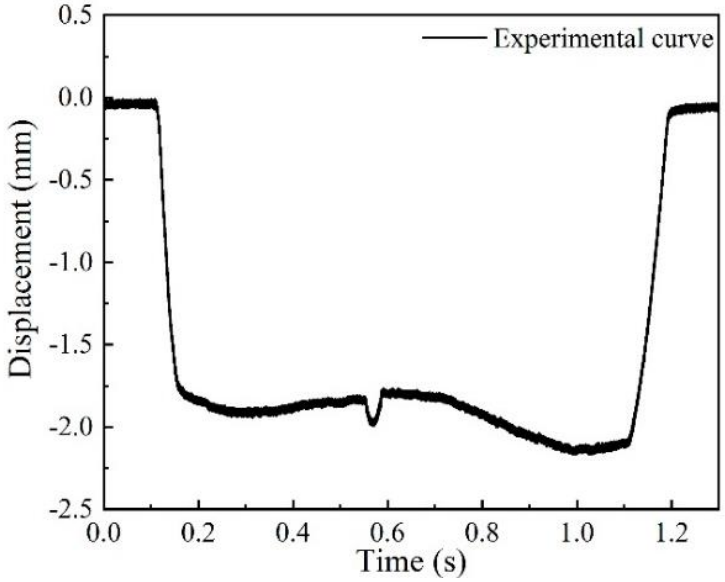

Figure 2-11 - Waveform measurement of a wheel flat obtained by the parallelogram method in laboratory enviornment. Taken from Gao et al. (2019)

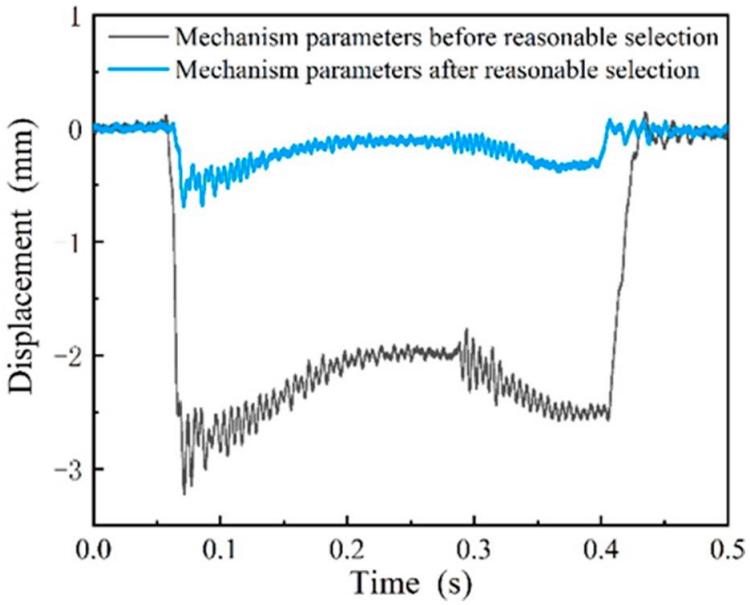

Figure 2-12 – Motion process of the mechanism parameters both before and after a thoughtful selection of the parameters for implementing the parallelogram mechanism in field conditions. Taken from Gao et al. (2019)

According to the findings in the work of Gao et al. (2019), the effectiveness of the system was demonstrated by the outcomes of laboratory tests. More details on the parallelogram mechanism method for wheel flat detection can be found in Gao et al. (2019).

Vibration-Based Detection using Envelope Analysis

The work of Wang et al. (2020) evaluated wheel flat detection on high-speed railway vehicles (running at speeds of at least 200 km/h) by utilising a vibration-based detection method. For this study a wheel flat length, L, of 10 mm was considered, along with vertical and lateral track irregularity profiles for both the left and right rail. The track is based on a normal slab track system, with the model being based on Euler-Bernoulli beam theory.

The simulations performed for conventional time domain have been shown that faster running speed of trains effectively reflect the influences of wheel flats at the same operating conditions. However, the wheel flat is difficult to describe using general time domain analysis when the wheel flat is small. Additionally, the trending amplitudes of the vibration fluctuate randomly, making it challenging to adapt to the shifting environmental conditions. In terms of frequency domain simulations, results have been illustrated that, at high running speeds, wheel flat may considerably excite the axle box frequency response. Nonetheless, basic spectrum analysis is also an ineffective approach since it has a limited ability to identify faults. The results from these simulations can be seen in Figure 2-13.

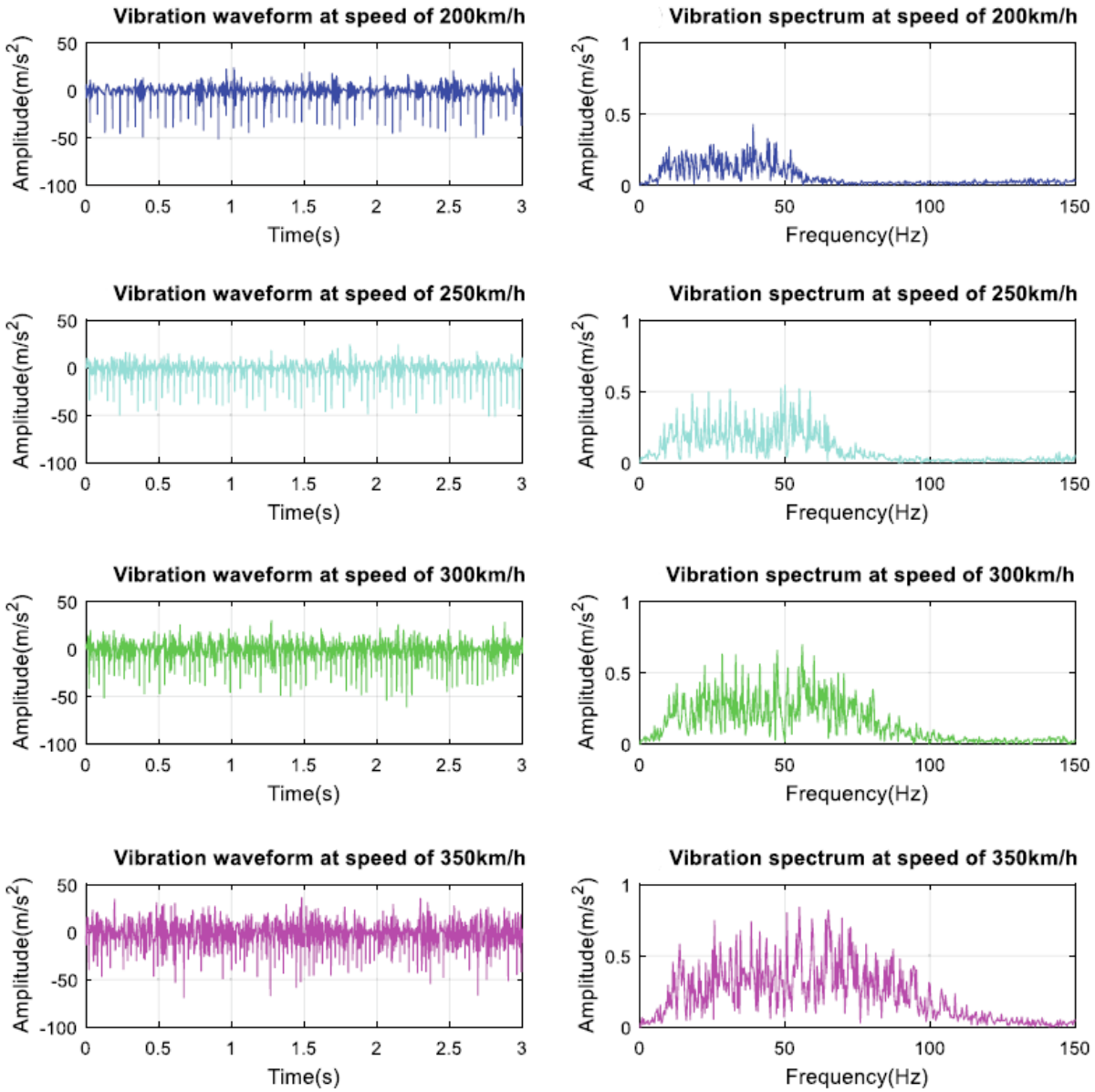

Figure 2-13 - Time domain (left) and frequency spectrum (right) of vibration signals at various speeds. Taken from Wang et al. (2020)

In order to improve the vibration-based detection technique for high-speed trains with wheel flats, Wang et al. (2020) implemented an envelope analysis to extract the modulated signal from an amplitude-modulated signal. More details on an envelope spectrum analysis are presented in Chapter 4. By subjecting the vibration signal to an envelope analysis, it is clear that the characteristic frequencies and the harmonic feature are successfully recognised for a high-speed train with flat wheels when compared to the results of the time domain and frequency domain. The results of the envelope analysis of the simulations mentioned above are shown in Figure 2-14.

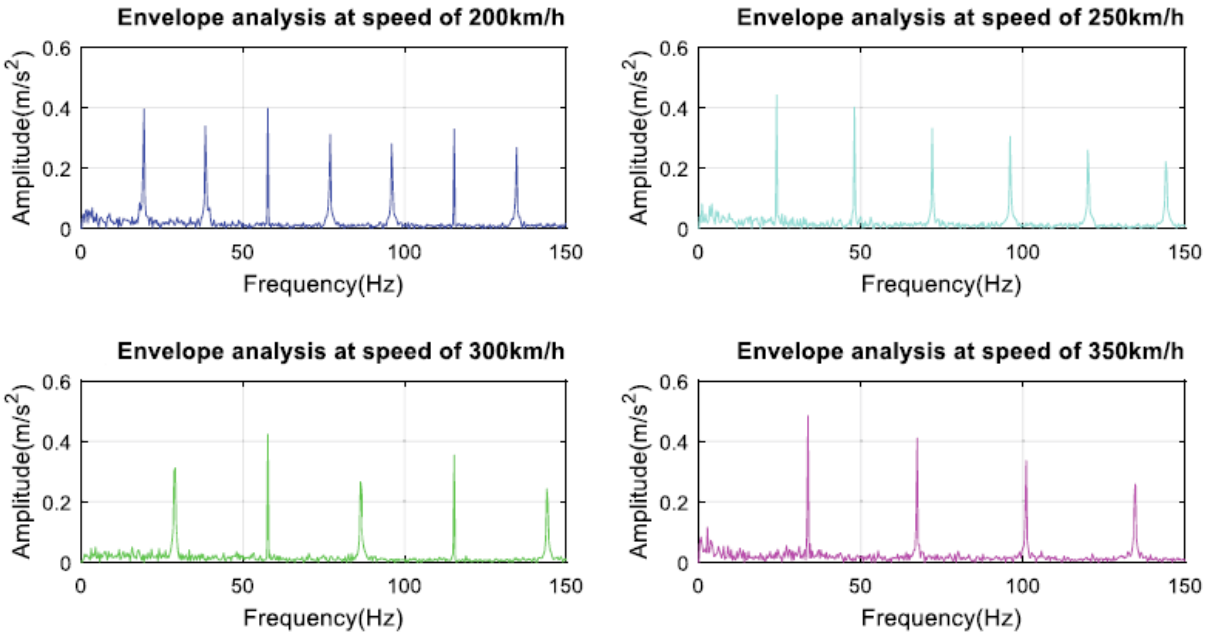

Figure 2-14 - Filtered envelope analysis of vibration signals. Taken from Wang et al. (2020)

More details on the vibration-based method using envelope analysis for train wheel flat detection can be found in Wang et al. (2020).

Wayside Monitoring System using Envelope Spectrum Analysis

The work of Mosleh et al. (2020b) explored envelope spectrum analysis as a means for wheel flat detection. In vibration monitoring, the envelope spectrum is frequently employed, particularly for rolling element bearing diagnosis. Before computing the spectrum, the envelope time signal is extracted. This relates to demodulation of the amplitude, being helpful where the vibration phenomenon is modulated above a fixed frequency value. Amplitude demodulation is used to retrieve the signal envelope. After that, the frequency is examined to reveal the repeating frequencies, even when they exhibit a slight random variation. The envelope spectrum, being the spectrum of the envelope signal, has a considerably lower frequency than the original signal. For this case, extensive demodulation was required in order to determine the envelope spectrum.

The numerical modelling of the train (based on an *Alfa Pendular* passenger train), track, and train-track interaction system were performed similarly to what was implemented for this thesis. More detail on the numerical modelling is exposed in Chapter 3. The envelope spectrum analysis, also implemented for this thesis, is explained in detail in Chapter 4.

The novelty of Mosleh et al. (2020b) work was defining a methodology that utilises a wayside monitoring system to detect wheel flats and the frequency of the flats. For that, the methodology using envelope spectrum techniques had to clearly distinguish a healthy wheel from a defective one. The wayside monitoring system consists of 12 strain gauges (SGs) sensors on each rail of the simulated track, located between two sleepers, as can be seen in Figure 2-15.

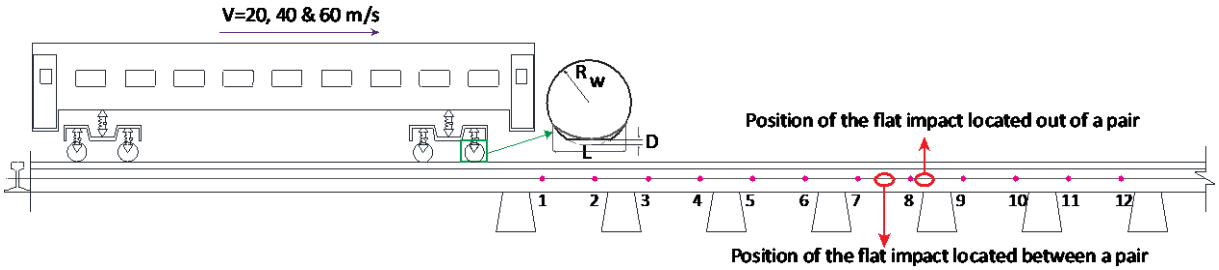

Figure 2-15 - Schematic of a vehicle passing through the six pairs of SGs. Taken from Mosleh et al. (2020b)

The paper also showed that conventional power spectral analysis (FFT) did not reveal the presence of a wheel flat, as can be seen in Figure 2-16. In the figure, both scenarios show insignificant changes between signals evaluated from 12 SGs. When applying the envelope spectrum analysis, the wheel flat becomes clear to detect by observing the lag between the responses of the SGs in a defective wheel. For a healthy wheel, there is no indication regarding the presence of flats in the envelope spectrum analysis approach and the envelope spectrum of the signal obtained by the 12 positions of SGs does not reveal a significant lag when compared with a defective wheel. These comparisons can be easily seen in Figure 2-17.

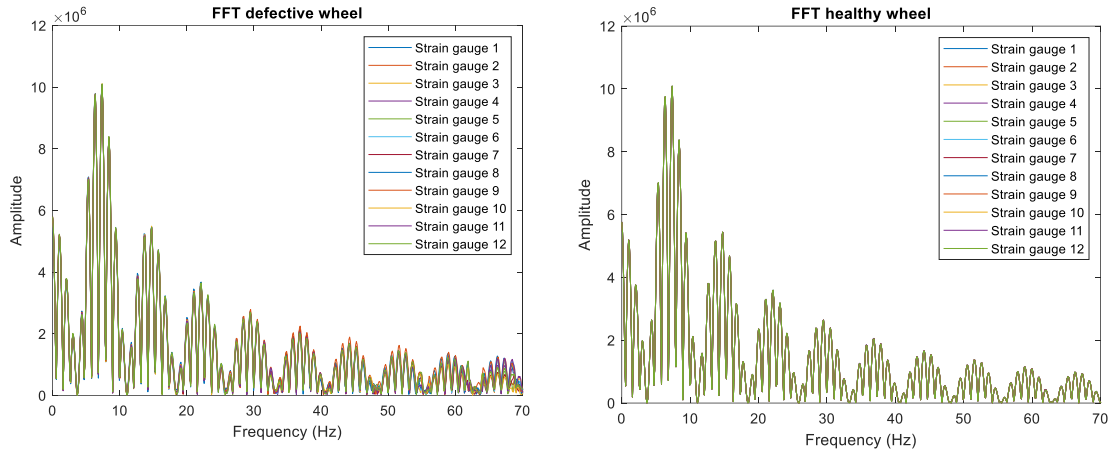

Figure 2-16 - Frequency contents of shear obtained for the 12 SGs for speed *V*=20 m/s: defective wheel with a flat, *L* = 150 mm and *D* = 1.5 mm (left); healthy wheel (right). Taken from Mosleh et al. (2020b)

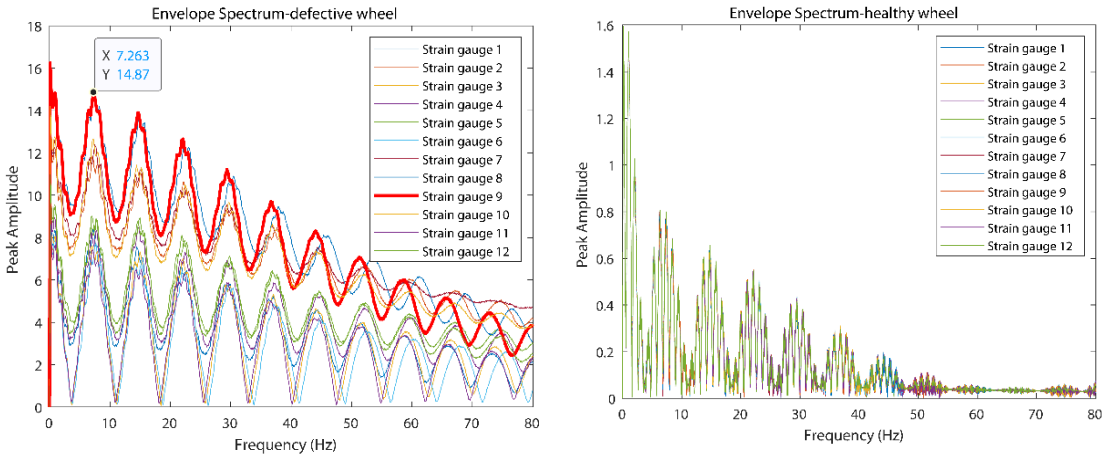

Figure 2-17 - Envelope spectrum analysis for the 12 SGs for speed *V*=20 m/s: defective wheel with a flat, *L* = 150 mm and *D* = 1.5 mm (left); healthy wheel (right). Taken from Mosleh et al. (2020b)

The method also shows positive results in detecting wheel flats in irregular railway tracks, as shown in Figure 2-18. This validates the effectiveness of the methodology analysing wheel flats even in unevenness tracks.

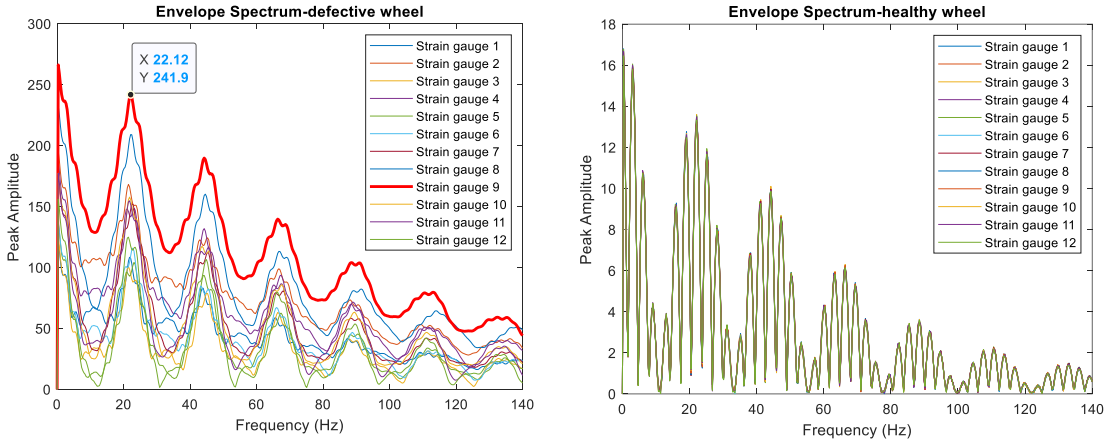

Figure 2-18 - Envelope spectrum analysis for the 12 SGs with unevenness track profile: defective wheel with a flat (left); healthy wheel (right). Taken from Mosleh et al. (2020b)

An important aspect seen in the wheel flat scenarios of both Figure 2-17 and Figure 2-18 is the variation of maximum peak amplitudes ("lag") across the responses from the SGs. Here, SG 9 shows the maximum peak amplitude in both cases. This indicates that SG 9 is the closest sensor to the wheel flat impact.

The article also evaluates other aspects, such as the influence of flat length and flat depth on the dynamic load, that are not in related to the purpose of this dissertation. More information about other conclusions drawn from this research can be found in Mosleh et al. (2020b).

Wheel Flat Detection with Multiple Records using Spectral Kurtosis Analysis

In Mosleh et al. (2021), the method implemented for wheel flat detection can be seen as a continuation of the previous work presented in Mosleh et al (2020b). Here two types of trains were considered: the *Alfa Pendular* passenger train, the same analysed in Mosleh et al. (2020b), and a freight wagon.

The numerical modelling of the train, track, and train-track interactions are equal to the numerical modelling done in Mosleh et al. (2020b). In this article, the wayside monitoring system consisted of 12 SG sensors and 12 accelerometers installed on the rail, between the sleepers, along with 7 accelerometers located on the rail over the sleepers. Figure 2-19 illustrates the layout scheme of the sensor locations.

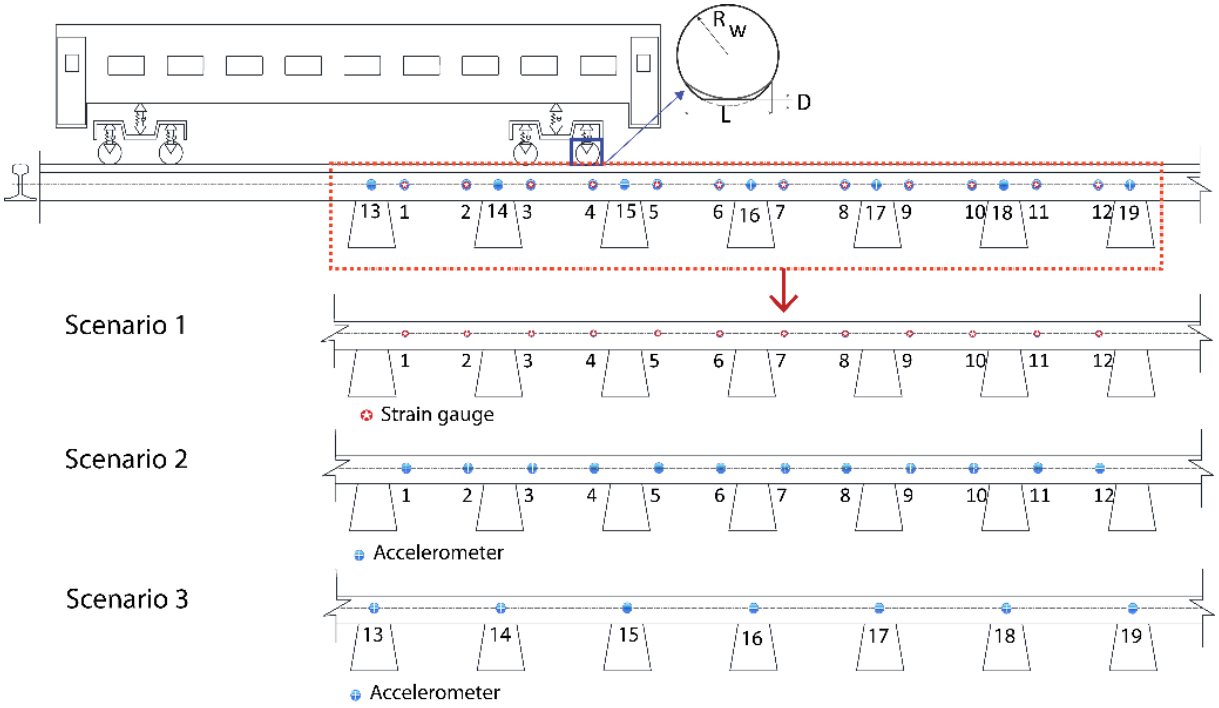

Figure 2-19 - Schematic of the sensors locations with a vehicle passing with a wheel flat. Taken from Mosleh et al. (2021)

The approach of this method for wheel flat detection was to implement the envelope spectrum method implemented in Mosleh et al. (2020b) with spectral kurtosis analysis. This allows the application of low-pass filters to reduce analyses from cases contaminated with noise. An example of a signal with noise contamination and its corresponding kurtogram after realising kurtosis analysis can be seen in Figure 2-20. The procedure is described in subsection 4.2.1, and more information about kurtosis can be found in Mosleh et al. (2021).

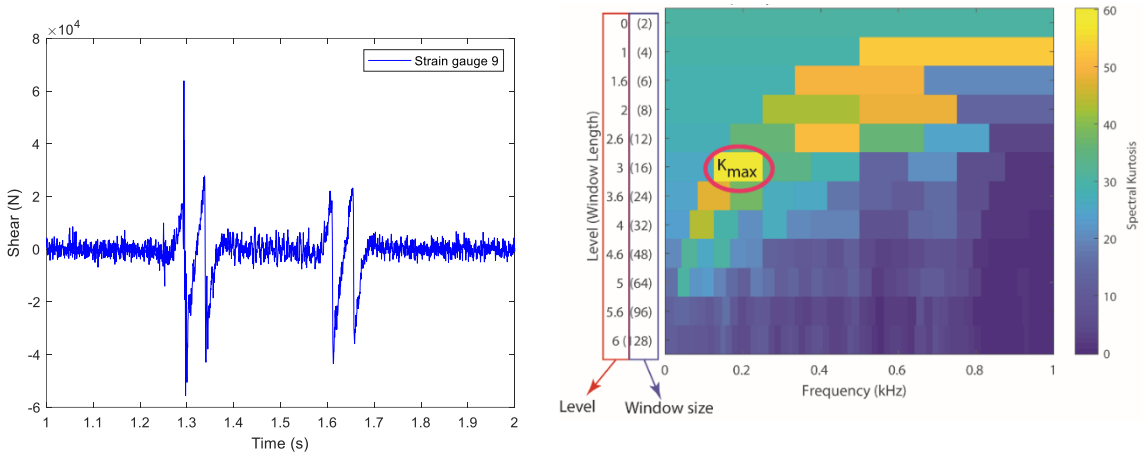

Figure 2-20 - Main signal obtained from strain gauge 9 from the passage of the *Alfa Pendular* vehicle (left) and corresponding spectral kurtosis, with K_{max} = 60.25 Hz, optimal window length = 16, center frequency = 0.1875 kHz, and bandwidth frequency = 0.125 kHz. Taken from Mosleh et al. (2021)

The multisensor decision was made in order to analyse if accelerometers could detect wheel flat in the same manner as strain gauges, since SGs are not suitable for long-term monitoring of wheel flats in part due to their vulnerability to water and electromagnetic interferences. Also, in order to reduce installation and maintenance costs, accelerometers were also considered above each sleeper to analyse if fewer sensors could still lead to positive results.

Figure 2-21 shows the results obtained from the SGs. The accelerometers were able to identify responses from defective wheels in both layout scenarios (between sleepers and on top of sleepers), as can be seen in Figure 2-22 and Figure 2-23. Spectral kurtosis analysis values are also different between healthy and damaged wheel, having higher values for wheel flat, especially if the flat impact is close to the sensors, as can be observed in Figure 2-24. More details about this research can be read in Mosleh et al. (2021).

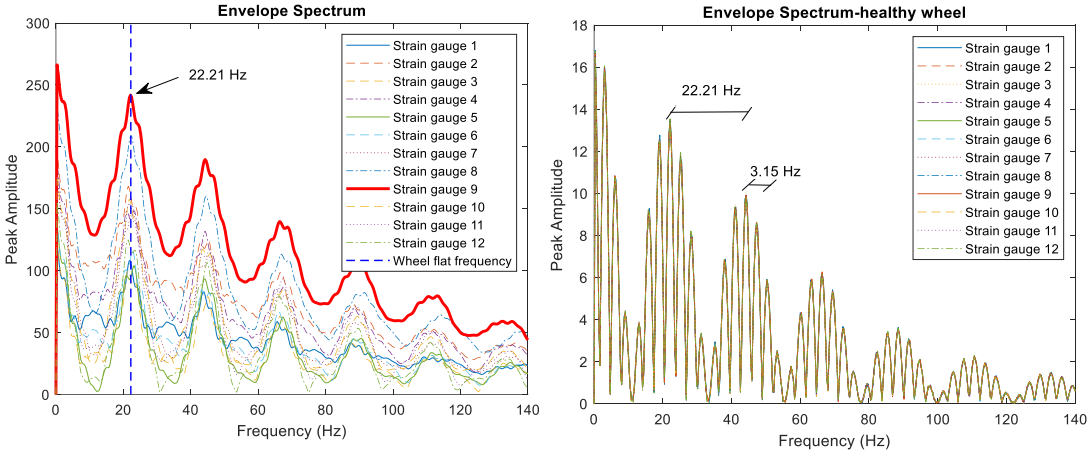

Figure 2-21 - Envelope spectrum analysis for the 12 SGs for the Alfa Pendular considering unevenness profile of the track, with a defective wheel (left), and a healthy wheel (right). Taken from Mosleh et al. (2021)

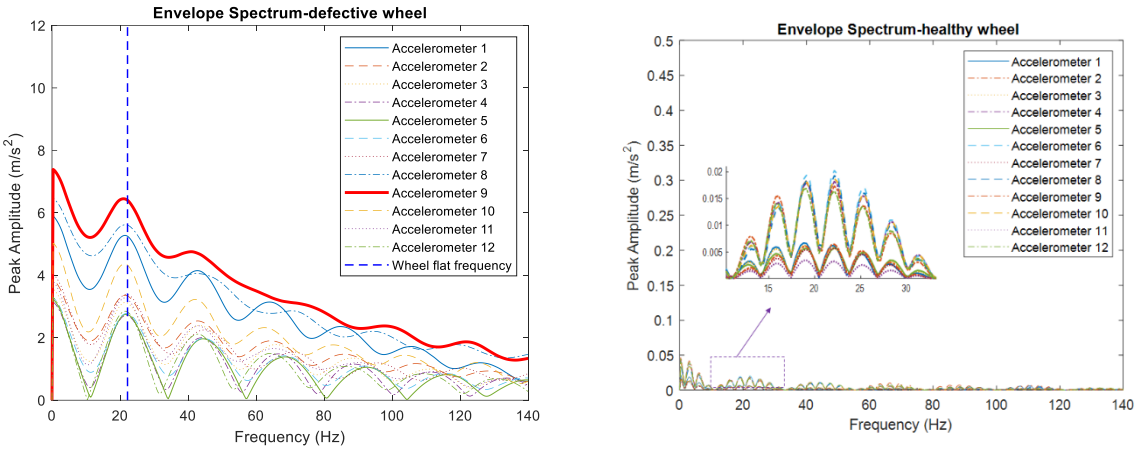

Figure 2-22 - Envelope spectrum analysis for the 12 Accelerometers between the sleepers for the Alfa Pendular considering unevenness profile of the track, with a defective wheel (left), and a healthy wheel (right). Taken from Mosleh et al. (2021)

10% noise

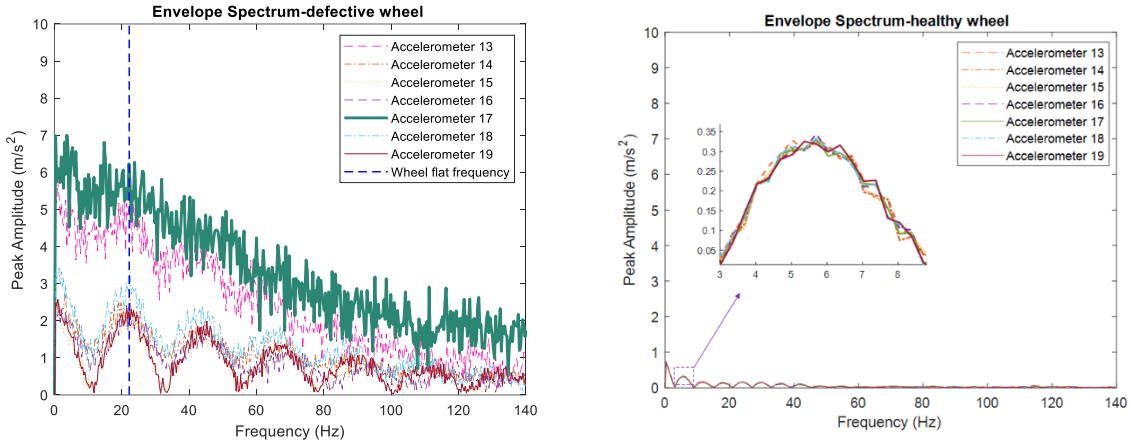

Figure 2-23 - Envelope spectrum analysis for the 7 Accelerometers on top of the sleeper for the Alfa Pendular considering unevenness profile of the track and considering a noise intensity level in the signal of 10%, with a defective wheel (left), and a healthy wheel (right). Taken from Mosleh et al. (2021)

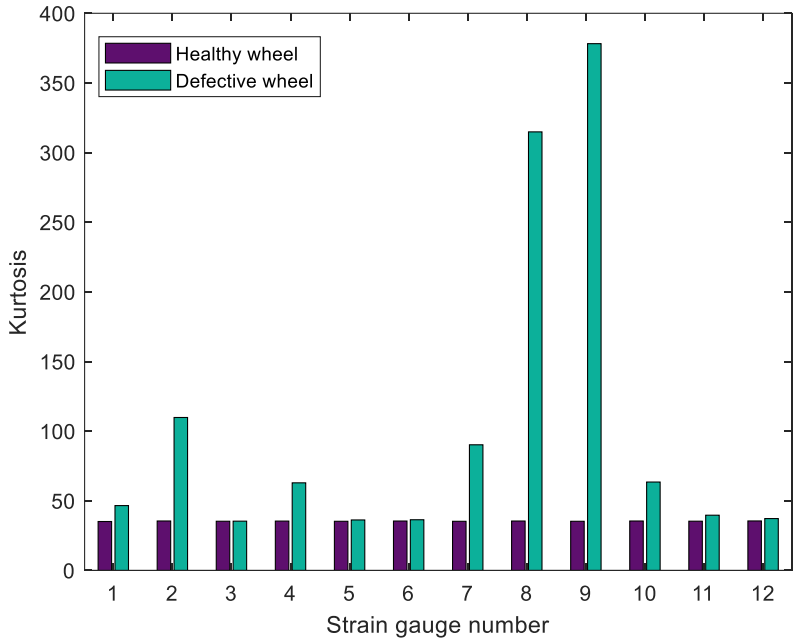

Figure 2-24 - Envelope Kurtosis values for healthy wheel and wheel flat for each SG sensor located on the track for the passage of the *Alfa Pendula*. Taken from Mosleh et al. (2021)

Detection and Evaluation of Wheel Tread Images using Convolution Neural Networks

In Trilla et al. (2021), research was conducted on the implementation of the detection and evaluation of multiple integrated defects of railway wheel tread images using convolutional neural networks. Data of six types of wheel tread, including wheel flat, was collected in a set of 4600 pictures captured from smartphones.

A small sample of rolling contact fatigue defects was small e in order to obtain a more amenable distribution of defect types for direct supervised learning, since this type of tread defect comprised more than 80% of the cases in the database, which could lead toa unfavourable situation for Machine Learning. The resulting dataset was then shortened to 1200 pictures. A pixel-level Image Processing module was formulated to address issues related to the variability of the images taken, such as inconsistent focus, distance to the defect and lighting conditions. These issues originate due to the variety of smartphone models used to take the images, different operators that took the pictures and several times of day in which the pictures were taken. Then, the three colour channels, such as RGB (Red-Green-Blue) colour model, are encompassed into one single intensity channel. The edges of the pictures are trimmed in order to standardised them into squared shapes and the size of the images are downscaled to improve computational performance during processing. Finally, a histogram of the pictures is equalized to increase its contrast.

The multitask system architecture divides the main process task into five specialized data-driven modules, being: i.) defect detection – location (DD-Loc); ii.) defect detection – physical size (DD-Phy); iii.) defect classification (DC); iv.) engineering assessment (EA); and v.) confidence index (CI). A diagram of the process, including auxiliary modules, is presented in Figure 2-25.

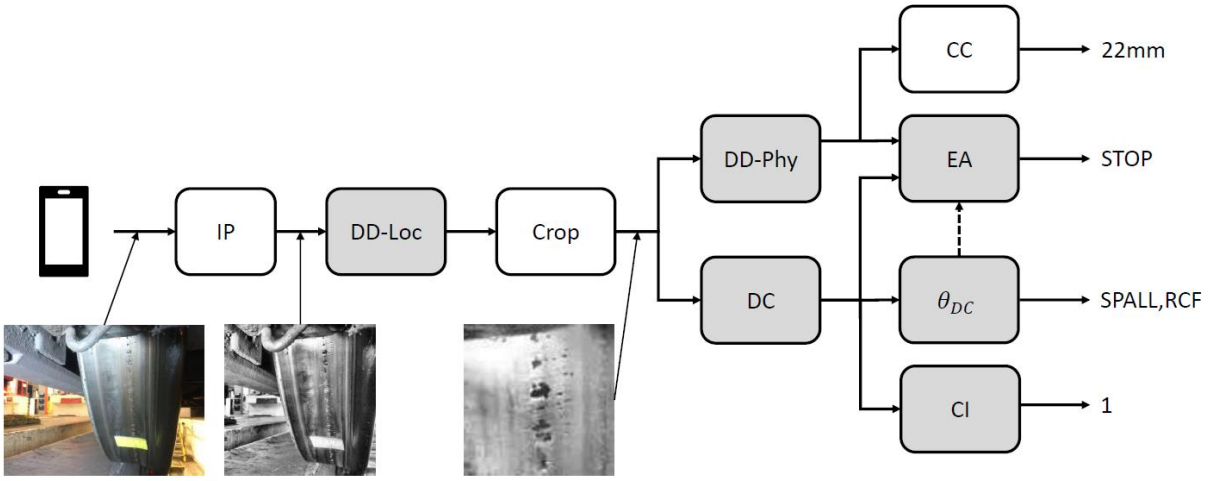

Figure 2-25 - Diagram of wheel tread defect diagnosis. The main modules above described are highlighted in shade of gray. Auxiliary modules Image Processing (IP), Cropping and Circunference Calculation (CC) are shown in white. Taken from Trilla et al. (2021)

The framework layout of the process is based on convolutional neural networks (CNN). CNNs are incredibly good at handling the high dimensionality of an image because they automatically reduce the solution search space (i.e., the number of learnable parameters) using a weight sharing strategy. They do this by employing a number of trainable filters that take advantage of the local surface statistical regularities of the images, as stated in Jo & Bengio (2017), which reduces the likelihood that the entire neural network will overfit the data. By using the same filter kernel repeatedly across the image, which has a translationally invariant structure, this method also makes these networks very resistant to location, identifying the same pattern at various locations in the pictures. In the layout of the CNN architecture design implemented is described, identifying the two learning stages: the feature learning and the task learning.

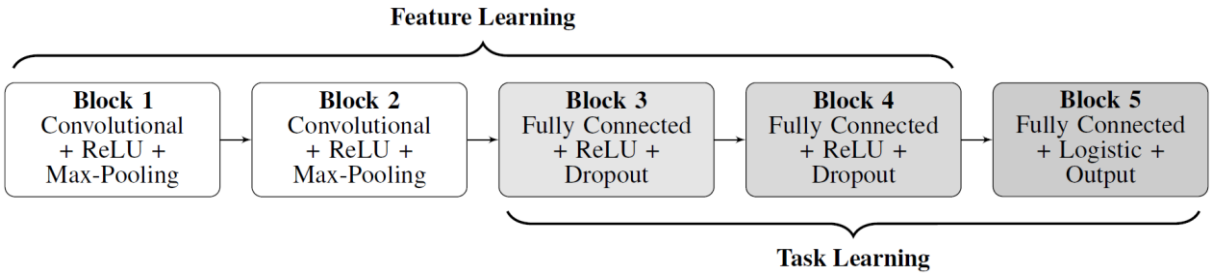

Figure 2-26 - Diagram of the functional blocks of the proposed unified CNN, showing the feature and task learning stages. Taken from Trilla et al. (2021)

The Machine Learning research was conducted with the Python3 programming language. The image processing tasks utilised OpenCV and scikit-image. The computations entailed by Deep Learning were carried out by TensorFlow2 (Guo et al., 2019). The architecture stack of the industrialisation of the solution ran on top of a cluster of machines managed by Kubernetes, a tried-and-true technology for automating, scaling, and ensuring high availability of software. It is further divided into four layers, illustrated in: i.) data layer; ii.) flow layer; iii.) application layer; and iv.) presentation layer.

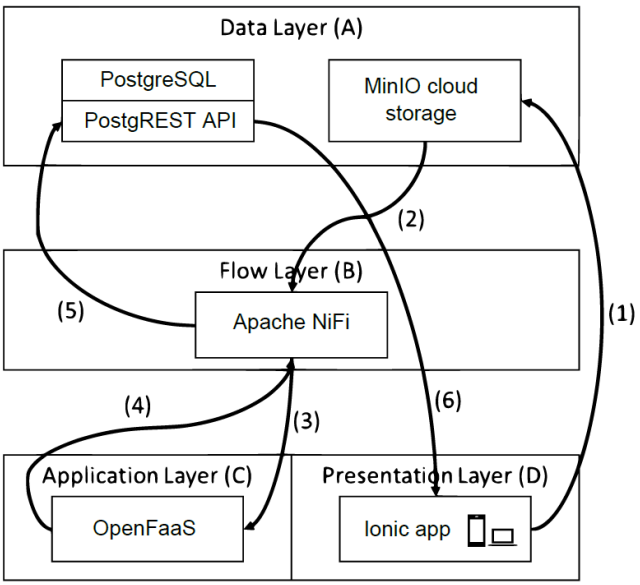

Figure 2-27 - Four layers utilised in the industrialised architecture of the wheel tread diagnosis framework. Taken from Trilla et al. (2021)

The results for DD-Loc demonstrates that the prediction error is centred on the target since there is no bias to the left or right or up or down. Figure 2-28 presents these results, with the location prediction error distribution determined as the difference between the X and Y coordinates. The degree of uncertainty is 9.5 pixels, or 12.66% of the picture size.

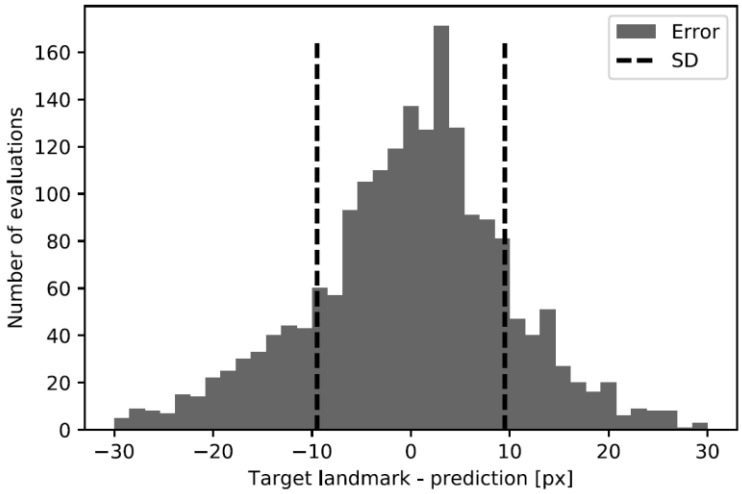

Figure 2-28 - Histogram of the defect location prediction error, with the uncertainty indicates by the 60% confidence interval Standard Deviation (SD). Taken from Trilla et al. (2021)

Regarding DC performance, further operational context is required for evaluation, since the accuracy performance indicator is unreliable when the system is biased toward the defect type that constitutes the majority. In the case of this work, that would be rolling contact fatigue.

In this research it is explained that deep learning and neural networks are two examples of machine learning techniques that may display unanticipated instability when subjected to minor perturbations. As a result, they are vulnerable to adversarial situations, which are deliberately tampered with data and cause the system to confidently output false. Additionally, because some of these minor perturbations are difficult to detect as they exploit edge cases, image processing programmes are particularly targeted by these assaults.

They conclude that identifying defects in railway wheel tread using raster image data is a difficult task that requires different levels of analysis. The comprehensive approach presented in this paper uses several Convolutional Neural Networks to identify the damaged areas in the images, calculate the physical size of visible defects and assess the type and severity of the defects. This proposal outlines a task-division strategy that makes the limitations and drawbacks of the predictive value chain easier to comprehend. The findings illustrated that over half of the present engineering labour devoted to manually identifying possible problems may now be automated, resulting in a shorter lead time for taking an appropriate maintenance action and, ultimately, optimising workforce activities.

More indicators are analysed in this research, regarding engineering assessment, image filters, project management of the methodology, among others. An in-depth description of this stages and future work to improve the methodology can be found in Trilla et al. (2021).

Advanced Acoustic Signal Analysis for Wheel Flat Detection

The works conducted in Komorski et al. (2021) consist of detecting wheel flats on light rail vehicles using advanced acoustic signal analysis. The major component of the experimental investigation consisted of sound measurements made during multiple pass-by tests at the Franowo tram depot in Poznan, Poland. All types of trams returning from service travelled by the area where the measuring equipment was located, close to one of the main lines. For track-side diagnostic systems based on vibroacoustic signals, it is an excellent observation point. The tram moved at a speed of 20 to 40 km/h. The primary objective of the measurements was to create a foundation for the diagnostic approach to locate wheel flat utilising acoustic signals and sophisticated analytical methods.

Figure 2-29 depicts the measurement position. Three microphones (M1, M2 and M3) were placed 2000 mm apart from the exterior rail. The distance between the microphones and the track was 2.04 m, which is equivalent to the circumference of each tram wheel (Komorski et al., 2018). Additionally, the lowest and maximum wheel diameters were around 600 and 654 mm, which is significant for calculating the frequency of wheel rotation. Additionally, photocells were utilised to calculate the average tram speed during the experiments.

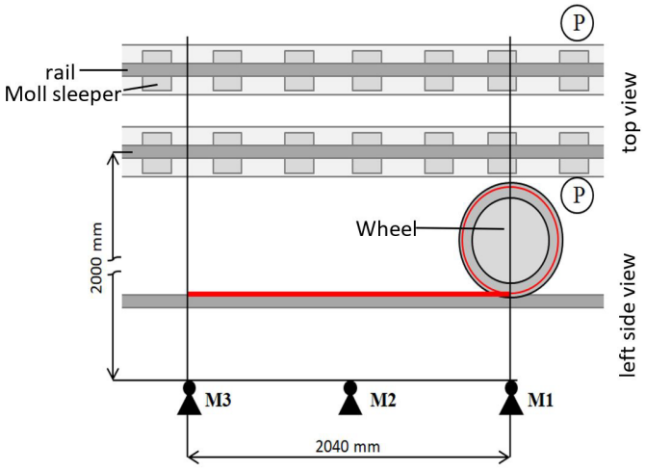

Figure 2-29 - Scheme of the measuring position during accoustic pass-by-tests. M1, M2 and M3 - Microphones; P - Photocells. Taken from Komorski et al. (2021)

The experimental study performed using Brüel & Kjaer equipment. The B&K type 3050-A 060 with 6 input data collection module was utilised. All three B&K 4189-A-021 microphones has a high measuring sensitivity of around 50 mV/ms^{-2}, making them the first accuracy class microphones. Prior to the acoustic testing procedure, transducers were also calibrated.

The measuring spectrum, which was 25,600 Hz, was the first major recording parameter. Regarding acoustic measurements this range should not be less than 20,000 Hz, according to Thompson (2009), and the high sampling frequency, which was 65,536 Hz. As a result, the system offered high-quality audio data with a synchronised recording of all signals. The length of the samples, which varied between 5-7 seconds, depended on the speed of the tram passing through the measuring section.

The analyses were initiated by determining the frequency characteristic of the wheel surface damage, f_{fp}, by implementing the following equation:

$$f_{fp} = \frac{V}{c_w}[Hz] \quad (2)$$

in which:

- V, is the linear speed of the tram in m/s;
- c_w, is the circumference of the wheel in m, which requires *a priori* measurement of the wheel diameter.

By analysing the acoustic signal envelope spectrum with the first three harmonics of the wheel rotation frequencies recorded using three microphones in conjunction with the calculated Root Mean Square values it was found that further research could be conducted with only one microphone, as the difference between describing the audio signal in the frequency domain did not exceed 3 dB. The microphone utilised in further analysis corresponds to M1.

Figure 2-30 displays the FFT from recorded sound pressure signals for trams travelling at speed 30 km/h and 40 km/h with and without wheel flat. With the help of this analysis, it was discovered that the signal needs to be filtered in the 800 Hz±500 Hz before applying envelope analysis. While alternative bands (such as 800 Hz and 4,000 Hz) that also exhibit an increase in amplitude were tested, the choice was

based on one of the visible resonance frequency ranges. Figure 2-31 displays the spectra of the first three harmonics of the rotational frequency of the wheel, observed at 30 km/h and 40 km/h.

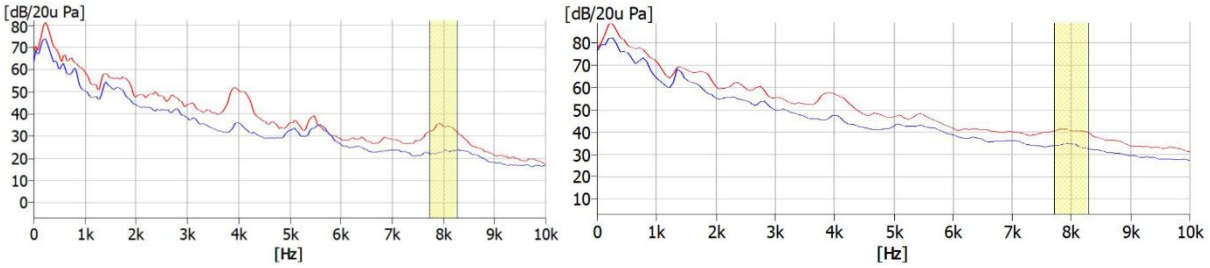

Figure 2-30 - FFT sound pressure spectrum for tram speeds of 30 km/h (left) and 40 km/h (right). Red corresponds to wheel flat and blue corresponds to healthy wheel. Taken from Komorski et al. (2021)

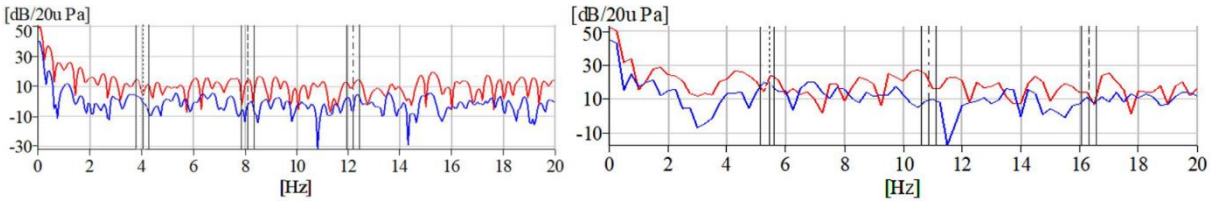

Figure 2-31 - Spectrum of acoustic signal envelopes with the marked band of the first three rotational harmonic frequencies of the wheel for tram speed of 30 km/h (left) and 40 km/h (right). Red corresponds to wheel flat and blue corresponds to healthy wheel. Taken from Komorski et al. (2021)

According to the results of the experiments, an auditory signal captured near to a passing rail vehicle is a very effective carrier of diagnostic data for the identification of flat tyres. Taking into account their influence on travel speed, the determined point measures in the form of sound pressure levels MAX and RMS satisfy the requirements of diagnostic parameters. Due to the Heisenberg uncertainty principle, it also appears that implementing the diagnostic process for lower speeds is a superior approach. Depending on the tram speeds, a given rolling stock operator should calculate the individual limit values of the diagnostic parameters specified. These figures must be related to the overall expenses associated with repairing any damage found during the assessment of external transportation expenses.

Additionally, research has shown that it is possible to reduce the number of measurement locations to a single one, which might help reduce the overall cost of developing a diagnostic system. The proposed approach can be an addition to already established trackside diagnostic equipment in rail vehicle depots. The microphone is one of the measurement tools that can be used to check the technical condition of other components, such as the running gear noise or the detection of unpleasant rattle sounds from loose components. The authors of this paper's future research will go in this direction. More detail on this research and its analyses can be found in Komorski et al. (2021).

2.2.2. Techniques for Periodic Wheel Polygonization Identification

Alongside wheel flat detection investigation, methods developed in order to detect wheel polygonization have been conducted over the last decade (Alemi et al., 2018; P. Wang et al., 2020; Gonçalves et al., 2023). The methods presented for periodic wheel OOR detection in this work are the following:

- Out-of-Roundness Monitoring using Polyvinylidene Difluoride (PVDF) Sensing Technology (Song et al., 2014);
- Out-of-Roundness Detection Method based on Parameter Optimisation (POVMD) and Multinuclear Least Squares-Support Vector Machine (LS-SVM) (Fang et al., 2020);
- Wheel Tread Polygonization Detection Method based on Dynamic Response (Xu et al., 2020);
- Diagnosis Method of Out-of-Round Metro Wheels with Strong Noise (Huang et al., 2021).

Out-of-Roundness Monitoring using PVDF Sensing Technology

In the research conducted by Song et al. (2014) a study on a train wheel OOR monitoring method using Polyvinylidene Difluoride (PVDF) strain gauge technology was investigated. Sensors and measuring devices located on the wayside system have the advantages of being passive to electromagnetic interference (EMI) and non-zero drift. This characteristic is especially useful for the new electrified train system as it protects the sensing network from EMI. The approach also enables in-service and real-time wheel condition monitoring, which is beneficial to the railway sector. The method includes connecting PVDF sensors to the rail web and calculating the contact forces based on changes in measured rail web strain. Since no equipment is required for vehicles, only at designated points, it is possible to inspect all vehicles that pass by the measuring point. A diagram of the working theory is depicted in Figure 2-32.

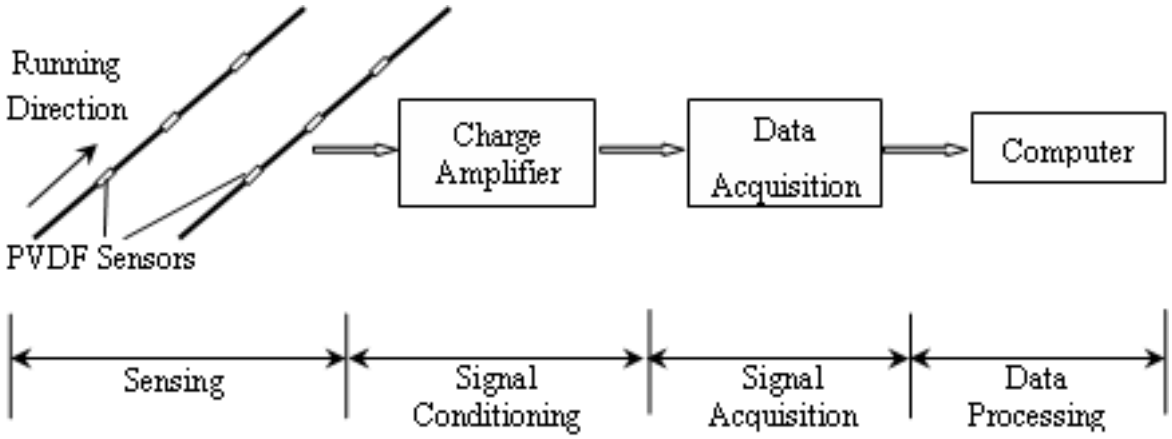

Figure 2-32 - Diagram of the work principle of PVDF OOR detection method. Taken from Song et al. (2014)

By calculating the parameters of the PVDF sensor, the generated charge values can be measured, and the resulting forces can be used to determine the horizontal and vertical wheel/rail force.

Figure 2-33 presents the relationship between the stress and the vertical wheel/rail force at three different curve slope locations. Compared to "Location 1" and "Location 2", "Location 3" has a steeper curve. The PVDF strain sensor was conveniently attached at “Location 3” (50 mm away from the end of the sleeper), and the measurement point was strain-sensitive.

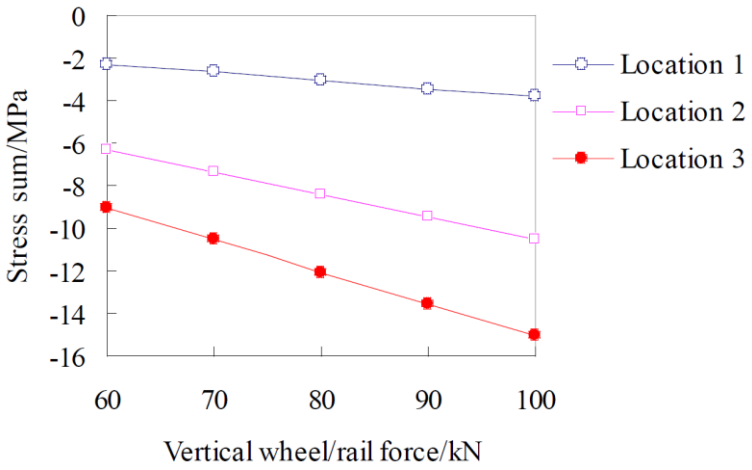

Figure 2-33 - Relation between stress and vertical wheel/rail force. Taken from Song et al. (2014)

Figure 2-34 shows the relationship between curve slope and speed, keeping the vertical wheel/rail force and speed constant. According to simulation results in different horizontal wheel/rail forces, the horizontal wheel/rail force had a negligible effect on the measured curve slope. Figure 2-35 shows the relationship between curve slope and the horizontal wheel/rail force, while maintaining the vertical wheel/rail force. The results point out that the effect on slope of the measured curve from different train speeds is also insignificant. More information of the research can be found in Song et al. (2014).

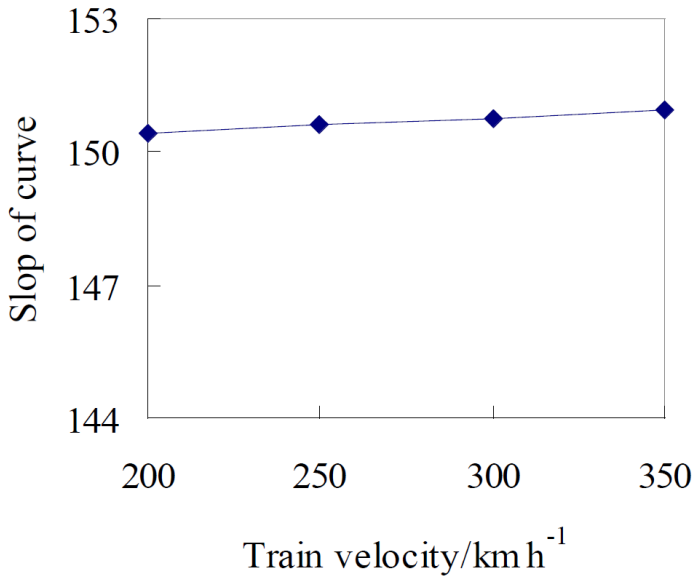

Figure 2-34 - Relation between curve slope and train speed. Taken from Song et al. (2014)

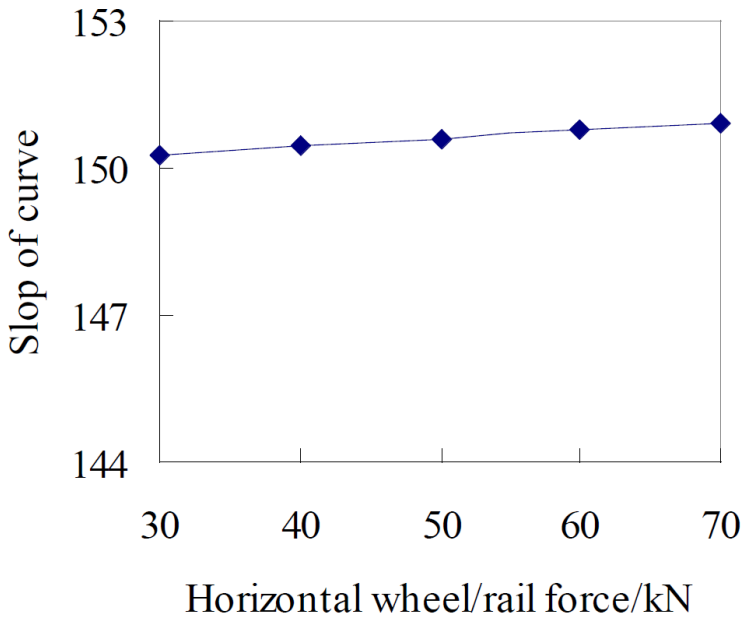

Figure 2-35 - Relation between curve slope and horizontal wheel/rail force. Taken from Song et al. (2014)

Out of Roundness Detection Method based on POVMD and Multinuclear LS-SVM

In the work of Fang et al. (2020) a method for identifying OOR using parameter optimisation (POVMD) and multicore core least squares support vector machine (LS-SVM) was developed. In a normal variational mode decomposition (VMD) algorithm, parameter *K*, further explained in Chapter 4, needs to be set artificially. In order to set more reasonable values for *K* and α, POVMD algorithm was envisioned by combining the VMD algorithm with particle swarm optimisation (PSO) algorithm, described in Kennedy & Eberhart (1995).

The equality constraint is used by LS-SVM to convert the quadratic optimization problem into a set of linear equations, as described in Li et al. (2016). A new kernel function is created by combining various kinds of kernel functions in the multi-core method. Figure 2-36 describes the steps implemented for the developed method.

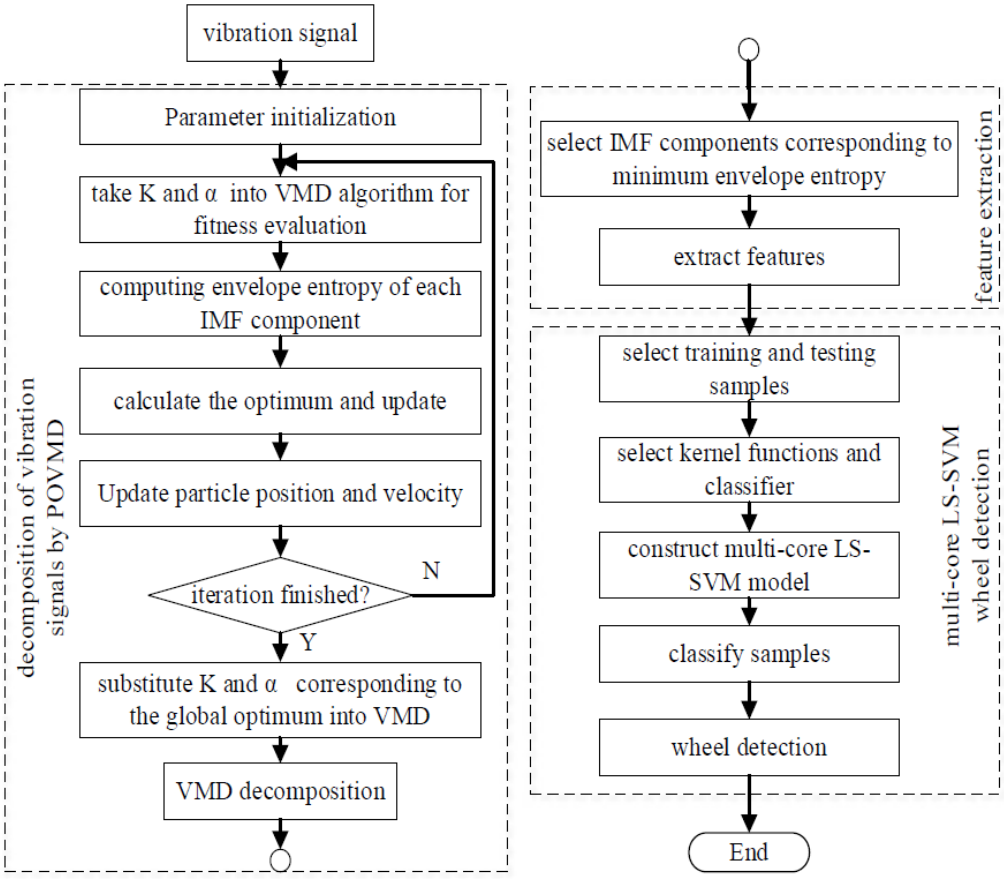

Figure 2-36 - Diagram of wheel non-circular detection method based on POVMD and mult-core LS-SVM. Taken from Fang et al. (2020)

The paper defines non-circular wheels as the division into non-circulars of the first to fourth orders. First-order non-circular describes the eccentricity during production. The second-order non-circular denotes the elliptical shape of the wheels. The third-order non-circular denotes the triangle appearance of the wheels; and fourth-order non-circular shows the rectangular appearance of the wheels.

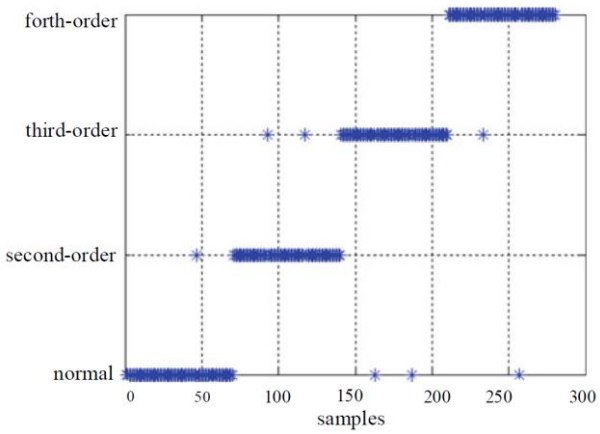

Figure 2-37 - Results from wheel classification analyses. Taken from Fang et al. (2020)

Figure 2-37 presents the results from specific wheel classification. Looking at the values from the sample axis, numbers 1-70 correspond to normal wheels, 71-140 are second-order wheels, while 141-210 and 211-280 are belong to third-order and fourth-order wheels respectively. From the results it can be observed that the best result for regular wheels is 0.9857, while all the results for second- to fourth-order wheels are 0.9714. High accuracy rate for detecting wheel non-circle is obtained by using a multi-core LS-SVM model, which satisfies the actual engineering requirements.

After building the model, data from single-side wheel of four wheels collected from two Guangzhou Metro carriages were analysed. The method was able to identify a second-order non-circular fault on the defected wheel while identifying the remaining wheels as healthy wheels, verifying the method when utilising real wheel data measurements. A more in-depth appreciation of this method, along with detailed results on the analysed wheels, can be consulted in Fang et al. (2020).

Wheel Tread Polygonization Detection Method based on Dynamic Response

In the work of Xu et al. (2020), a detection method for polygonised wheels based on dynamic response was developed. In order to diagnose the polygonization of the wheel, the authors developed a method inspired by the works of Liu et al. (2007) and Hu et al. (2008). In those works, a method using adaptive resonance demodulation and Short-time Fourier Transform (STFT) based vibration signal demodulation was implemented, in order to diagnose bearing faults. The method Xu et al. (2020) elaborated in their paper consists of adaptive resonance demodulation based on synchrosqueezed STFT (SSTFT) in order to analyse the vehicle dynamic response data. Figure 2-38 shows a diagram of the detection method.

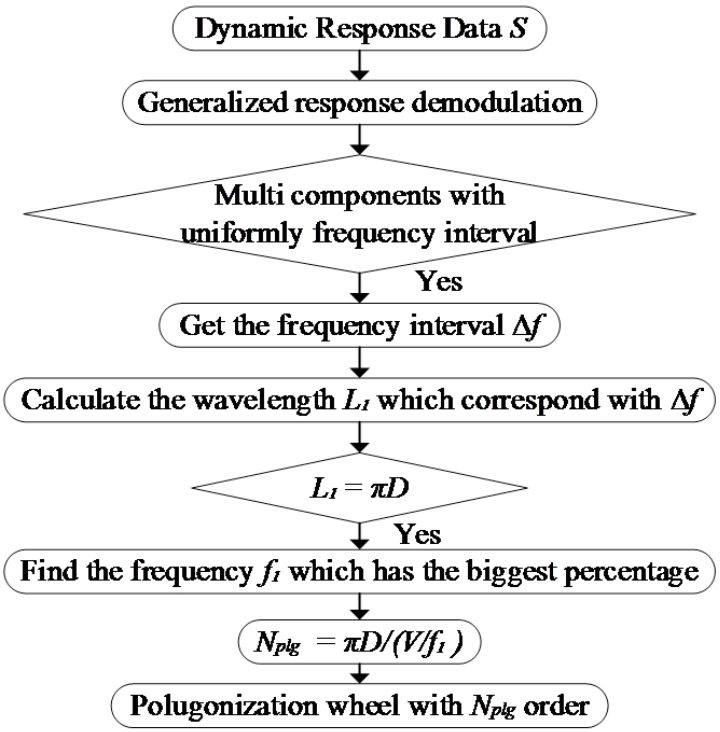

Figure 2-38 – Diagram of the detection method for polygonised wheels based on dynamic response. Taken from Xu et al. (2020)

The numerical results of the method applied to a defective wheel of a high-speed train are presented in Figure 2-39, Figure 2-40, Figure 2-41 and Figure 2-42. By analysing the envelope spectrum of the signal (Figure 2-41, left) the vehicle dynamic response fault frequency and its multiplier can be clearly observed, as the peak interval is equal to the wheel polygonization response, confirmed by Equation (3):

$$\pi D = \frac{V}{\Delta f} \quad (3)$$

in which:

- πD, corresponds to the wavelength (see Figure 2-38);
- V, is the train speed;
- Δf, is the frequency interval.

In contrast, the envelope spectrum signal obtained using a more traditional method (Figure 2-41, right) does not clearly show this feature, especially regarding the components near 70 Hz and 100 Hz.

Looking at the roughness data and polygonization of the wheel in Figure 2-42, it can be observed that the wheel suffers from a 16th order polygonization wear, with a roughness level higher than 10 dB/μm. More information on this developed method can me consulted in Xu et al. (2020).

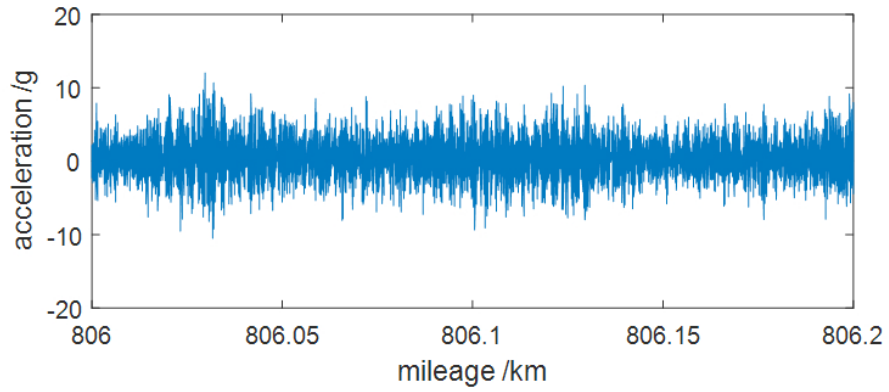

Figure 2-39 - Vehicle axle box acceleration. Taken from Xu et al. (2020)

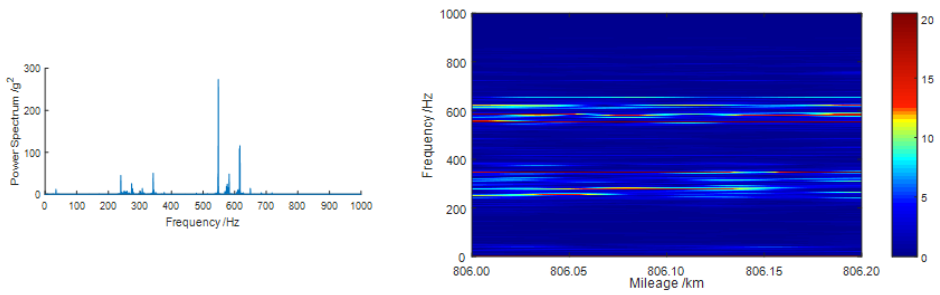

Figure 2-40 - Power spectrum (left) and time-frequency diagram (right). Taken from Xu et al. (2020)

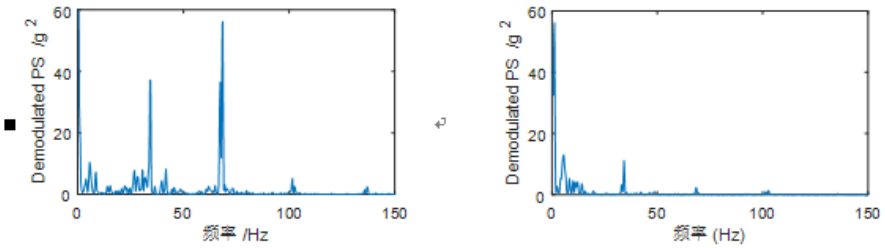

Figure 2-41 - Spectral envelope from the proposed method (left) and the traditional method (right). Taken from Xu et al. (2020)

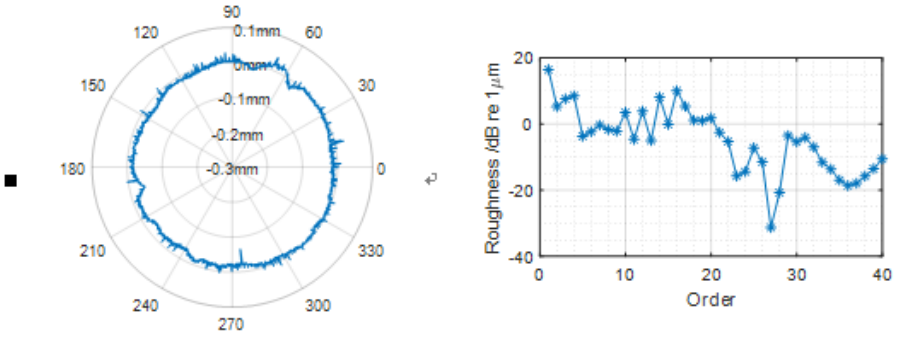

Figure 2-42 - Roughness data of wheel surface: amplitude in polar coordinates (left); polygonization level (right). Taken from Xu et al. (2020)

Diagnosis Method of Out-of-Round Metro Wheels with Strong Noise

In 2021, the work conducted in Huang et al. (2021) proposed a method to detect OOR in metro vehicle wheels with strong noise. This method, known as KPCA-DBN diagnosis model, combines Kernel Principal Component Analysis (KPCA) and Deep Belief Network (DBN) to analyse OOR wheel defect detection.

To record wheel vibration signals more accurately, vibration sensors were placed on the axle boxes of four wheelsets, as illustrated in Figure 2-43. The sensors collected vertical vibration signals from the wheels. During the investigation, three groups of vertical vibration signals were established: normal, incipient OOR fault and serious OOR fault. Wheels showing a signal-to-noise ratio (SNR) below five have incipient or serious OOR faults, as can be seen in Table 2-1.

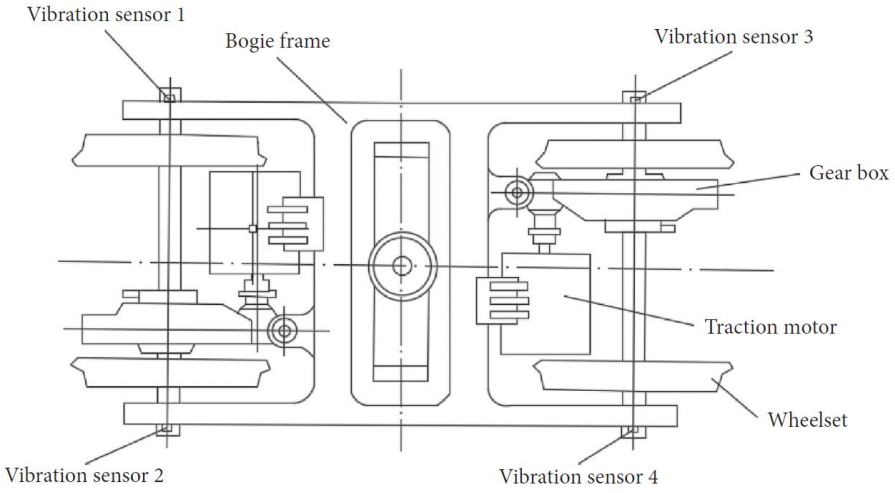

Figure 2-43 - Schematic for the location of the vibration sensors. Taken from Huang et al. (2021)

Table 2-1 - SNR of vibration signals without denoise and extracting principle principal component. Values from Huang et al. (2021)

Normal state	Incipient OOR fault state	Serious OOR fault state
12.67	1.85	3.96

The waves of vibration signal signals are represented in Figure 2-44, Figure 2-45 and Figure 2-46, and the spectra display of vibration signals are shown in Figure 2-47, Figure 2-48 and Figure 2-49. The values of the SNRs vibration signals for incipient and serious OOR faults states gathered from the sensors are bellow four, indicating that they all have low SNR signals with strong noise. SNRs of vibration signals were improved by selecting the wavelet threshold denoising function and setting the ideal number of wavelets de composition layers to remove strong noises, which implies fault information may submerge in strong noise. Then, by contrasting the SNR and root mean square error between the original and denoised signals, the impact of wavelet denoise is assessed.

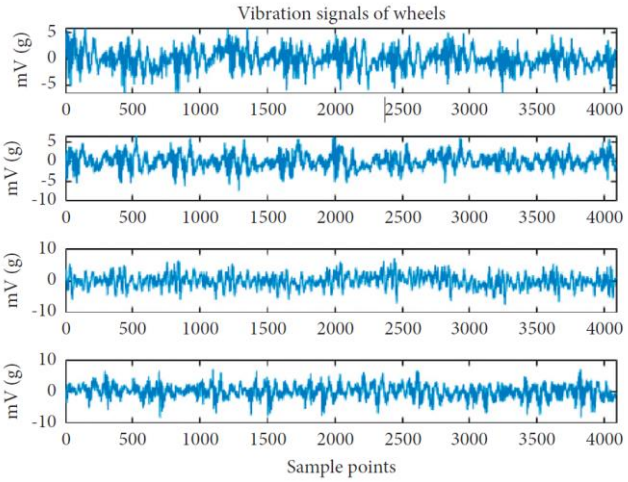

Figure 2-44 - Vibration waves of healthy wheels. Taken from Huang et al. (2021)

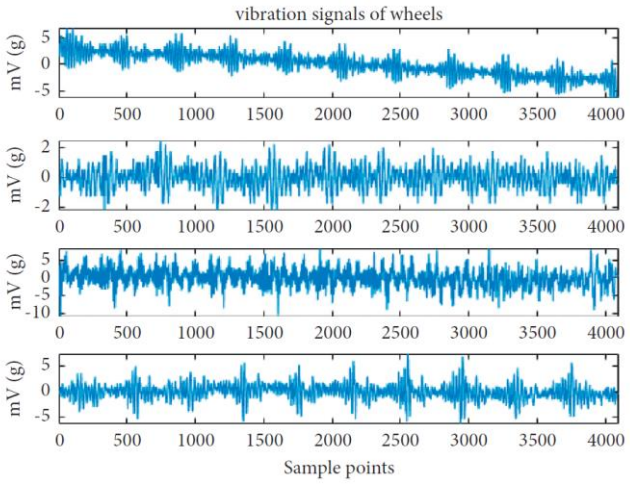

Figure 2-45 - Vibration waves of incipient faults wheels. Taken from Huang et al. (2021)

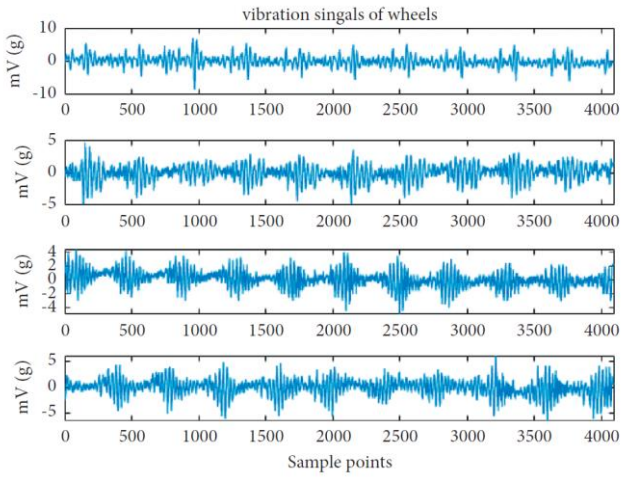

Figure 2-46 - Vibration waves of serious faults wheels. Taken from Huang et al. (2021)

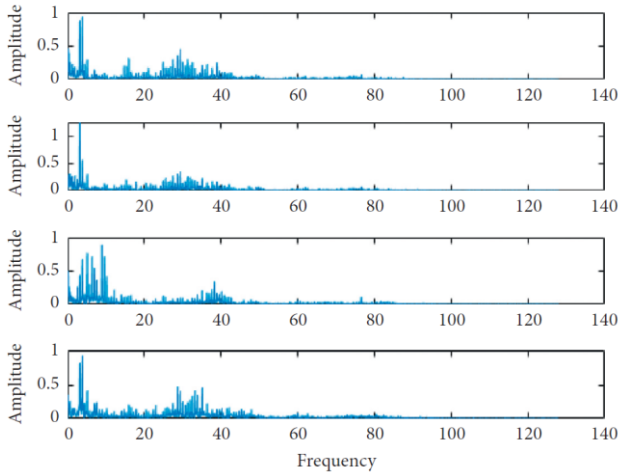

Figure 2-47 - Spectra display of normal signals. Taken from Huang et al. (2021)

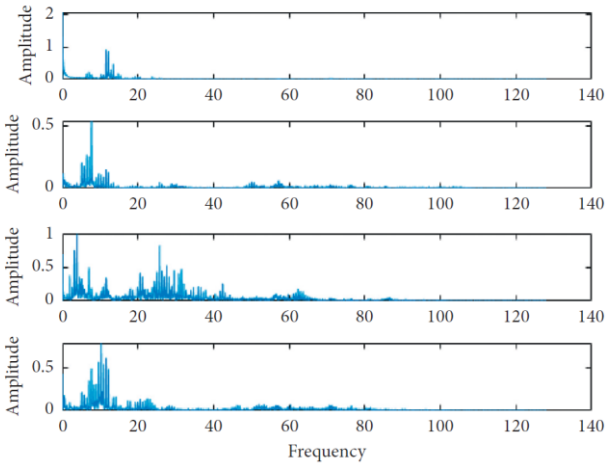

Figure 2-48 - Spectra display of incipient faults signals. Taken from Huang et al. (2021)

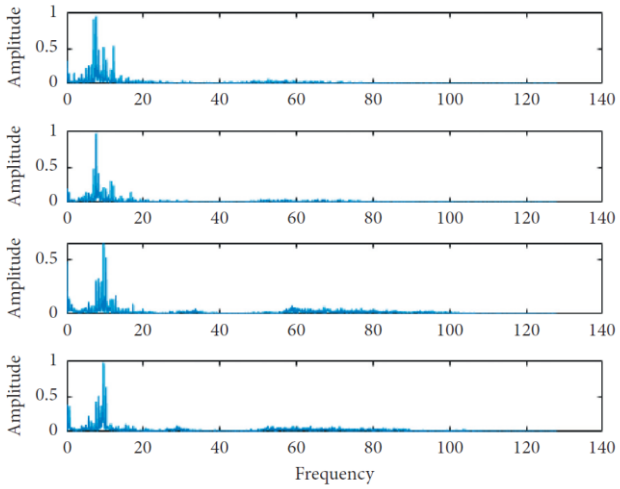

Figure 2-49 - Spectra display of serious faults signals. Taken from Huang et al. (2021)

When Deep Belief Network (DBN) was used to identify wheel defects, the number of layers, number of nodes, and step size were suitably chosen. The procedure can be seen in the diagram presented in Figure 2-50. In order to divide vibration signals into five intrinsic mode functions (IMFs) and minimise noise signals for IMF1 using wavelet, Variational Mode Decomposition (VMD) was applied.

For the fault diagnosis method, Figure 2-51 shows the denoise technique used to minimise the noise in the vibration signals of metro car wheel sensors, which are used as input data for the OOR defect detection model. In an attempt to improve the detection accuracy of wheelset OOR defects, the characteristics of DBN were modified to match the vibration data of metro cars.

Having the optimal DBN parameters and the fault diagnosis model for the OOR fault of metro vehicle wheels, the layer number, node number, the number of records, were modified to fit the data of the metro vehicles. In this way, the model can be used to determine whether or not wheels have OOR defects.

Three groups of metro vehicle vibration data were utilised, including normal, incipient fault, and serious fault wheel vibration signals collected by vibration sensors. Each dataset included 10 sets of vibration signals to test the detection model along with wavelet, VMD, KPCA, and DBN approaches. First, all vibration signals were combined, and then they were once again divided into training dataset and test dataset.

Using wavelet and VMD to minimise the noise in all vibration signals, the dimensions of the signals were decreased by KPCA. There are 1000 iterations with a learning rate of 0.001. Test sets were added to the trained model to determine the diagnosis accuracy, calculated at 0.8611, and training sets were added to the model to detect OOR errors.

A total of six tests were performed. Among them, the outcome of the calculations indicated that the implemented parameters for Test Six settings were the most ideal ones among all the tests. The results of Test Six can be seen in Figure 2-52 and Figure 2-53.

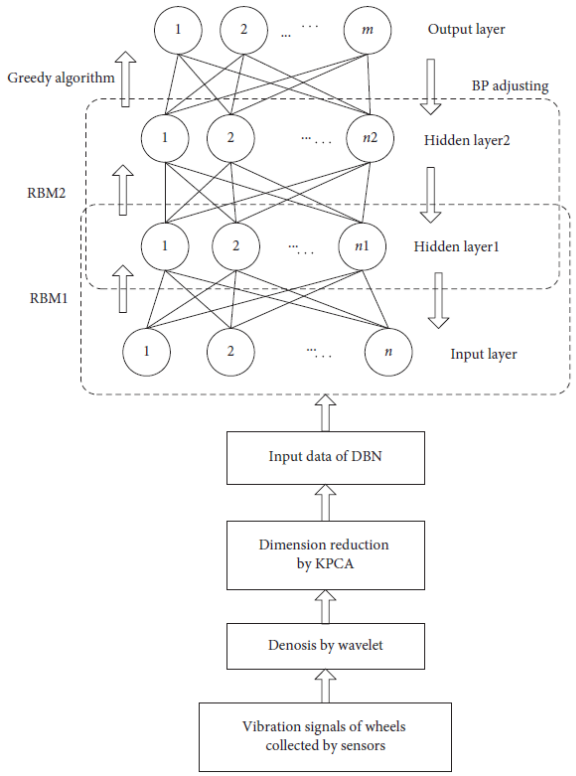

Figure 2-50 - Optimisation of the network using DBN. Taken from Huang et al. (2021)

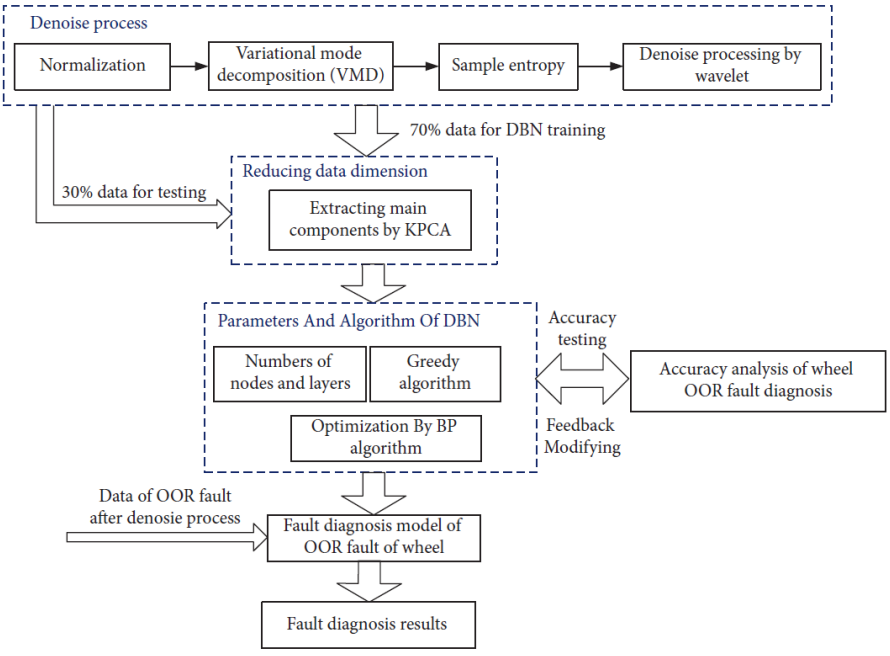

Figure 2-51 - Diagram of the procedure of OOR defect diagnosis for the metro vehicle wheels. Taken from Huang et al. (2021)

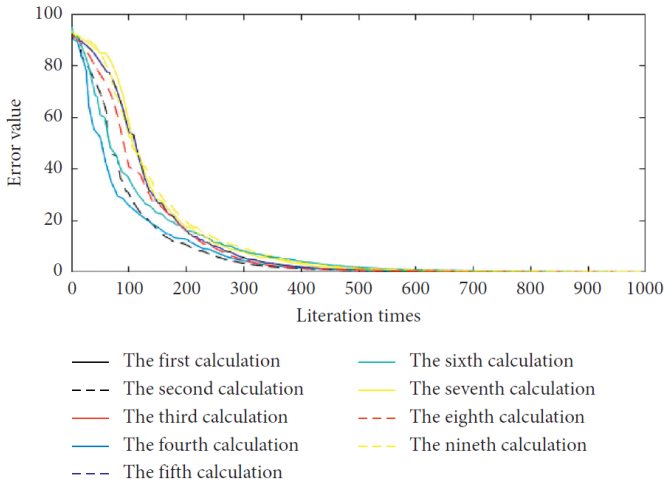

Figure 2-52 - Graph of declining erros with each iteration for Test Six. Taken from Huang et al. (2021)

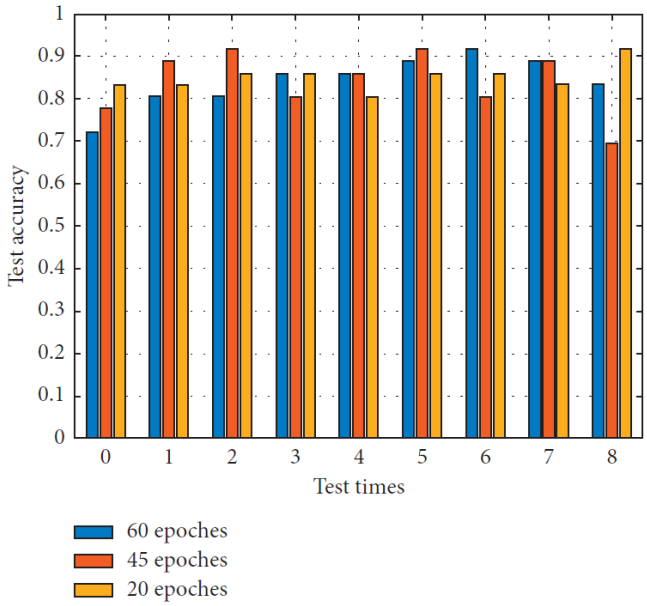

Figure 2-53 - Calculation accuracy with different epochs of Test Six. Taken from Huang et al. (2021)

It was concluded that the KPCA-DBN detection approach may improve SNRs of vibration signals of metro vehicle wheels and identify early OOR problems during metro vehicle operation. The results from the paper show that the average accuracy of the method reaches 0.9136. By applying this method, a realistic maintenance plan can be organised earlier, reduce maintenance cost, shorten train stop times, and increase stability and safety during metro train movement.

The authors add that this technique could be applied to identify OOR problems in high-speed trains. An in-depth look of the research conducted with all the analyses and results extensively detailed can be consulted in Huang et al. (2021).

3
NUMERICAL MODELLING

This Chapter presents: i.) an overview of the elements that compound a ballasted railway track; ii.) a description of the numerical modelling of the track, the train, the train – track interaction and iii.) the modelling procedure to generate track irregularity profiles.

3.1. INTRODUCTION

Rail tracks are the backbone of railway transport. They allow trains to travel in a safer, more reliable way compared to road transport. Furthermore, rail tracks are considered a limited space use compared to the extensive road transport areas. With moderate environmental impact and a high degree of automation and management, they are among the best option especially in densely populated areas. Passenger transport offers a comfort level comparable to automobiles and the possibility of reaching high speeds, competing with planes in the middle range distance (Esveld, 2001).

There are two main types of railway track: ballasted track and non-ballasted track. Ballasted tracks, also called “classic tracks” or “conventional tracks”, as the name suggests, they are the most commonly used type of railway track. They consist of a structure of rails and sleepers supported on ballast, which rests on a sub-ballast layer that serves as the formation's transition layer to the foundation. Since the introduction of high-speed rail cars in Europe in the 1970s, ballasted track of classical design has been used, providing one of the best stiffness-to-damping ratios. Extensive studies have confirmed the possibility for running higher speed trains with speeds of at least 300 km/h in ballasted tracks with an acceptable level of safety is safe, guaranteeing the resistance of the road to laterally applied forces (Fortunato, 2005; Pintão, 2021).

In a non-ballasted track, the rails are firmly connected to specific types of concrete sleepers that are firmly embedded in concrete. They offer some advantages over ballasted tracks, like lower maintenance, high availability, low structure height, and low weight. However, they involve higher construction costs, higher airborne noise reflection, and significant work when altering track position and superelevation. More information comparing ballasted track and non-ballasted track can be found in Esveld (2001).

This Chapter will focus in detail on ballasted tracks. This type of structure will be considered in the analyses. A ballasted track system is used in most Portuguese railway networks, namely the Northern Line which is in analysis in this work. Section 3.2 delves into the constituent elements of a ballasted track in detail.

3.2. CONSTITUENT ELEMENTS OF A RAILWAY TRACK

The general layout of the elements that constitute a ballasted track are depicted in Figure 3-1, showing the rails, railpads/fastening system, sleepers, ballast and sub-ballast layers and the subgrade.

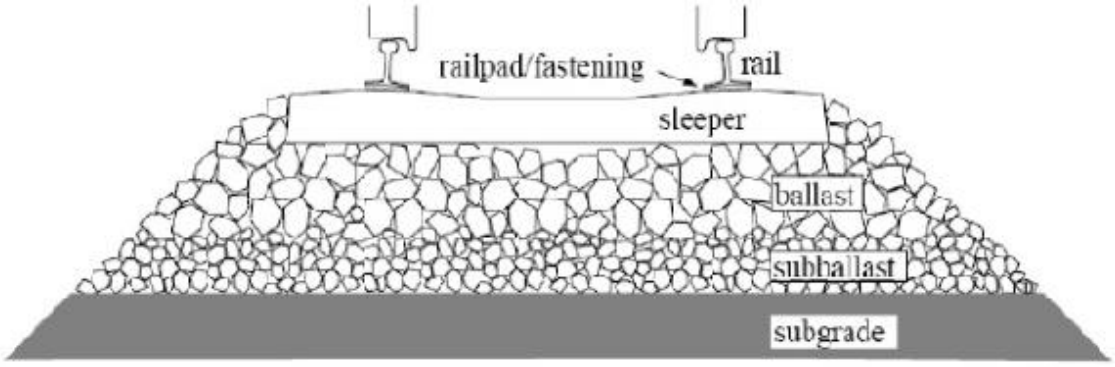

Figure 3-1 - Elements and layers of a ballasted track. Taken from Phanyakit & Satiennam (2018)

3.2.1. RAIL

The rail can be regarded as the most vital element of the track structure, serving the following functions as noted by Esveld (2001):

- it handles the wheel loads and distributes them over the sleepers and support;
- it guides the wheel in a lateral direction, any horizontal transverse forces on the rail head are transferred to and distributed over the sleepers and supports;
- by using adhesion, it creates a smooth-running surface and distributes braking and accelerating forces;
- it serves as an electrical conductor on an electrified line;
- it conducts signal currents.

Many types of rail profiles are used for different scenarios. Some of the more prominent rail profiles, as shown in Esveld (2001) and illustrated in Figure 3-2, include:

- flat-bottom rail profiles, being used as the standard profile in conventional tracks;
- non-standard profiles, like some tracks used in construction sites. They differ from standard profiles mainly by having a wider rail web in order to cater for switch and crossing components, and expansion devices;
- grooved or embedded rail profiles, used in enclosed track structures like roadways and yards;
- block rail profiles or Nikex system, used in some tram networks (Esveld, 1997);
- crane rail profiles, used to support hoisting cranes with high wheel loads.

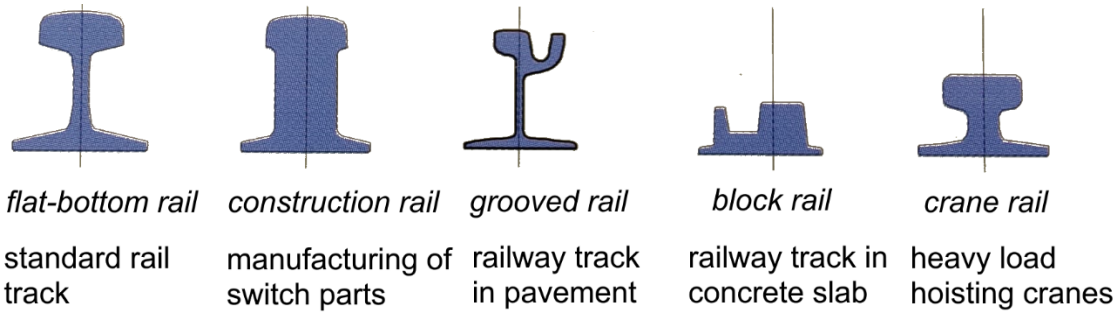

Figure 3-2 - Rail profile types. Adapted from Esveld (2001)

In this study flat-bottom rail is considered for modelling, based on the 54E1 (former UIC 54) and 60E1 (former UIC 60) profiles (EN 13674–1, 2017).

3.2.2. SLEEPERS

In ballasted tracks, the rails are placed on the sleepers, forming the built-up part of the superstructure. They maintain track gauge and rail inclination, support and fix the rail foot and fastenings, maintain rail forces by distributing them evenly across the ballast, and provide sufficient electrical insulation between the two rails (Esveld, 2001). The most common types of sleepers are timber and concrete sleepers and, partly, steel sleepers.

Concrete sleepers have been the most used in railway tracks for modern or renewed tracks. Their advantage over wooden sleepers is that they are less affected by the weather and have a much longer service life under certain conditions. However, concrete sleepers are susceptible to impact loads, especially in the 25-300 Hz frequency range (Esveld, 2001).

3.2.3.FASTENING SYSTEMS

All the parts that constitute the structural connection between rail and sleeper are collectively referred to as fastening systems, or "fastenings" for short. A great variety of fastening systems can be found across the world. Fastening can also be categorized as direct fastenings, where the rail is directly fixed to the sleeper, or indirect fastenings, where the rail is fixed to an intermediate component, like a baseplate, which is then fixated to the sleeper. Figure 3-3 illustrates an example of direct fastenings and indirect fastenings. In general, according to Esveld (2001) fastenings are responsible for:

- absorbing the rail forces elastically and transferring them to the sleeper;
- damp vibrations and impacts caused by traffic as much as possible;
- hold the track gauge and rail inclination within specific tolerances;
- establish electrical insulation between the rails and the sleepers, especially in the case of concrete and steel sleepers.

Figure 3-3 - Examples of direct fastenings (left) and indirect fastenings (right). Taken from Sadeghi et al. (2020)

3.2.4. Rail Pads

The purpose of rail pads is to filter out high-frequency force components when transferring the rail load to the sleeper. High stiffness rail pads reduce these frequencies more effectively. This is particularly important on curve sections of the track to prevent noise and premature wear of the fastening system. Modern rail pads can be found in various forms and materials, such as complete material, rubber bonded cork, foam-structured, grooved surface and studded surface.

3.2.5. Ballast Bed

The ballast bed consists of a layer of loose coarse-grained material that can withstand significant compressive loads due to internal friction between the grains but cannot withstand tensile stresses. The ballast bed has a considerable bearing strength in the vertical direction but is noticeably diminished in the lateral direction. The ballast bed should present a thickness, ideally between 25 and 30 cm measured from the lower side of the sleeper, in order to load the subgrade as uniformly as possible. Besides distributing loads and providing lateral resistance, the ability to drain the ballast bed is essential, as the storage capacity during rainfall should not be underestimated (Esveld, 2001).

In terms of types of ballast used in railway line rail, the most commonly implemented ones, as presented by Esveld (2001):

- crushed stone, composed of broken, solid, or sedimentary rock like porphyry, basalt, granite, gneiss, limestone, and others, and generally have 30/60 mm grading;
- gravel, obtained from rivers, with 20/50 mm grading; and
- crushed gravel, obtained by breaking up large pieces of gravel, with 20/40 mm grading.

3.2.6. Sub-ballast

The sub-ballast acts as an intermediate layer between the ballast bed and the subgrade. It is primarily used to improve filtering, protect against frost, separate the coarse-grain ballast from the fine sand, and provide better load distributions. It consists of a layer of gravel ballast with a thickness of around 10 cm and a grading of 5/40 mm (Esveld, 2001).

3.2.7. SUBGRADE

The formation composing the slopes, edges, ditches, and structures within them, is known as the subgrade or substructure. The subgrade must have sufficient load-bearing strength and stability, and must show reasonable settlement behaviour. The subgrade must exhibit tolerable settlement behaviour, adequate bearing strength and stability, and effective drainage of rainwater and melted snow from the ballast bed. Soil can be enhanced by excavating a trench, mechanically consolidating the soil, or chemically stabilizing the ground if the existing subgrade cannot adequately meet these requirements. The formation needs to be sufficiently robust and well consolidated. Additionally, the profile should not deviate too much from the design profile (Esveld, 2001).

3.3. NUMERICAL TRACK MODEL

The track can be modelled by using various models, like 2D, 2.5D and 3D models. A representation of each model is illustrated in Figure 3-4.

A 2D model simulates track behaviour in the vertical and longitudinal directions. A more in-depth view on 2D track models can be found in Vale & Calçada (2014) and Vale (2021). Figure 3-4(**a**) shows a representation of a 2D track model.

When comparing the results of a discrete support model with the comparable continuous model, the effect of discrete support of the rails is almost minimal, as demonstrated from the research conducted by Vostroukhov & Metrikine (2003) and Takemiya & Bian (2005). Therefore, the rail-foundation mass system can be considered infinite and constant along the longitudinal direction if the discontinuity due to the periodic nature of the sleepers is omitted. Thus, a very effective computational method called 2.5D can be used, which only requires that the problem's cross-section be discretized because it uses a Fourier transform of the spatial variable in the direction of track development. A 2.5D model can thus simulate the dynamic track response, along with its subgroup response. The only difference between a 2.5D model and a fully three-dimensional model lies on the inherent geometric limitations of the 2.5D concept: i.) the structure must be infinite; ii.) the structure has to be invariant in at least one direction (Costa, 2011). Figure 3-4(**b**) illustrates a 2.5D track model.

In order to perform global analyses of the track structure, a more complex 3D model may be used. Using a 3D track model, similar to the model presented in Figure 3-4(**c**), allows the evaluation, for example, track behaviour in curves and on joint areas, and the response of both track and foundation in the vertical and longitudinal directions (Jiang et al., 2019; Montenegro et al., 2020a; 2020b; 2021; Neto et al., 2021).

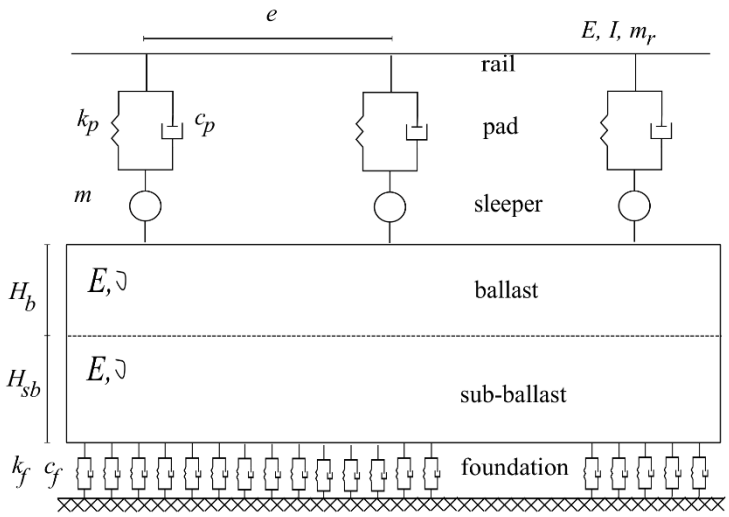

(**a**)

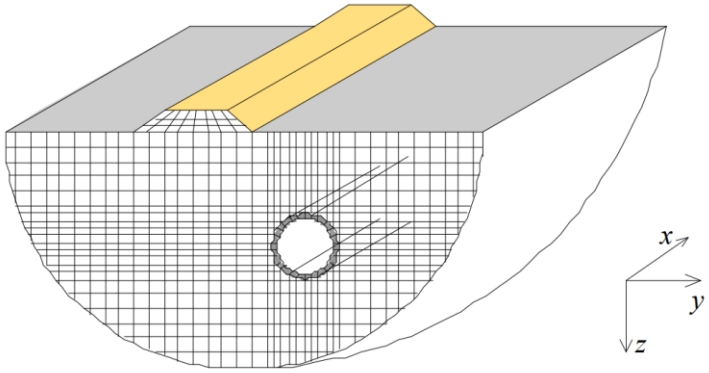

(**b**)

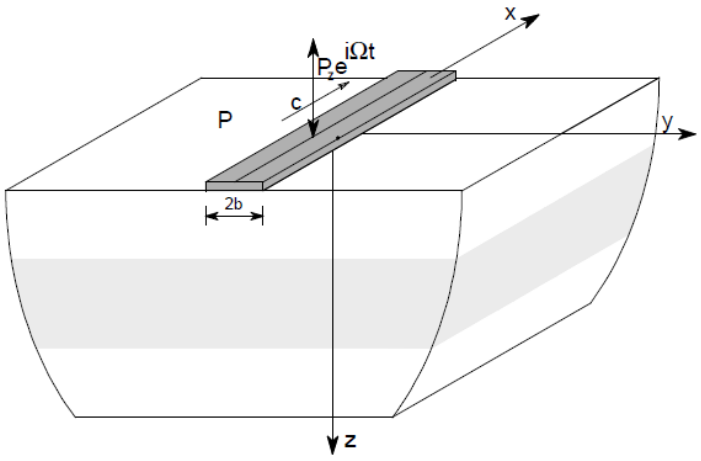

(**c**)

Figure 3-4 - Examples of track models: (**a**) 2D track mode, taken from Vale (2021); (**b**) 2.5D track model, taken from Costa (2011); (**c**) 3D track model, taken from Costa (2011)

In this work, a numerical 3D model based on a section of track from the northern line of the Portuguese Railway Network is developed using the ANSYS® (2018) software. It consists of a three-layer model that simulates the ballast, sleeper and rail elements of the track, connected through spring-dampers simulating the ballast and fastener pads (Mosleh, et al., 2020b). This type of track model uses linear finite elements (Fes), which are widely used in the field of train-track interaction analyses (Yang et al., 2004; W. Zhai et al., 2009, 2013), since it leads to a level of compromise between accuracy and computational efficiency that would not be achieved if more complex and detailed models were adopted (Mosleh et al., 2020b). Figure 3-4(**c**) shows a scheme of the track model, followed by the mechanical properties of the track represented in Table 3-1.

Table 3-1 - Mechanical properties of the track. Values from Mosleh et al. (2020b)

Parameter	Units	Value	Citation
Rail	A_r (m^2)	7.67E-04	European Standard (2002)
	ρ_r (kg/m^3)	7850	European Standard (2002)
	I_r (m^4)	30.38E-06	European Standard (2002)
	v_r	0.28	European Standard (2002)
	E_r (N/m^2)	210E + 09	European Standard (2002)
Rail pad, longitudinal	K_p (N/m)	20E + 06	Zhai et al. (2009)
	C_p (N s/m)	50E + 03	Zhai et al. (2009)
Rail pad, lateral	K_p (N/m)	20E + 06	Zhai et al. (2009)
	C_p (N s/m)	50E + 03	Zhai et al. (2009)
Rail pad, vertical	K_p (N/m)	500E + 06	ERRI D 214/RP 5 (1999)
	C_p (N s/m)	200E + 03	ERRI D 214/RP 5 (1999)
Sleeper	ρ_s (kg/m^3)	2590	
	v_s	0.2	
	E_s (N/m^2)	40.9E + 09	
Ballast, longitudinal	$K_{b,x}$ (N/m)	9000E + 03	UIC 774-3-R (2001)
	$C_{b,x}$ (N s/m)	15E + 03	Wu & Yang (2003)
Ballast, lateral	$K_{b,y}$ (N/m)	2250E + 03	ERRI D 202/RP 11 (1999)
	$C_{b,y}$ (N s/m)	15E + 03	Wu & Yang (2003)
Ballast, vertical	$K_{b,z}$ (N/m)	30E + 06	ERRI D 202/RP 11 (1999)
	$C_{b,z}$ (N s/m)	15E + 03	Wu & Yang (2003)
Foundation, longitudinal	$K_{f,x}$ (N/m)	20E + 06	Auersch (2008)
	$C_{f,x}$ (N s/m)	5.01E + 02	Auersch (2008)
Foundation, lateral	$K_{f,y}$ (N/m)	20E + 06	Auersch (2008)
	$C_{f,y}$ (N s/m)	5.01E + 02	Auersch (2008)
Foundation, vertical	$K_{f,z}$ (N/m)	20E + 06	Auersch (2008)
	$C_{f,z}$ (N s/m)	5.01E + 02	Auersch (2008)

In real conditions, the profile of rails is not perfect, presenting a set of irregularities along their profiles. This affects the wheel-rail forces resulting from the passing train. For the analyses performed in this work several track irregularity profiles were used to determine the dynamic wheel responses on the tracks. These irregularity profiles are based on the rail quality classification system defined by the Federal Railway Administration (FRA), nominated as specific track classifications. The order of classes ranges from class 1 to class 6, starting with the most irregular profile. The classification of railway tracks dictates specific construction details. These tolerances also determine the speed limit for trains. For the cases studied in this dissertation, inferior classes ("classes" 1 and 2) were disregarded.

A stationary stochastic process characterized by a power spectral density (PSD) function could simulate artificial unevenness profiles. The generation of the unevenness profiles is made using the PSD function

suggested by the FRA which, according to Hamid & Yang (1982) and Fries & Coffey (1990), is written as:

$$S(K_1) = \frac{10^{-7} A K_3^2 (K_1^2 + K_2^2)}{K_1^4 (K_1^2 + K_3^2)} \quad (4)$$

in which:

- K_2 and K_3, are constants assuming the values of 0.1465 and 0.8168 rad/m, respectively;
- A, is a parameter related to track quality, shown in Table 3-2;
- K, is wave number dependent on the cyclic spatial frequency of irregularity, given as $2\pi/\lambda$ and varying between $2\pi/30$ and 2π.

Table 3-2 - Roughness parameter for the FRA track classes. Values from Mosleh et al. (2020a)

Class	1	2	3	4	5	6
A (m^3/rad)	660.079	376.229	208.841	116.856	65.929	37.505
FRA: Federal Railroad Administration						

Additionally, to the generated six profiles, two more cases were considered: i.) a real track irregularity measured on the Portuguese Northern Line (nominated as "class 7"), ii.) a track profile without irregularities, representing a theoretical "perfect track" (nominated as "class 8"). Figure 3-5 shows the track irregularity profiles for classes 3 to 8.

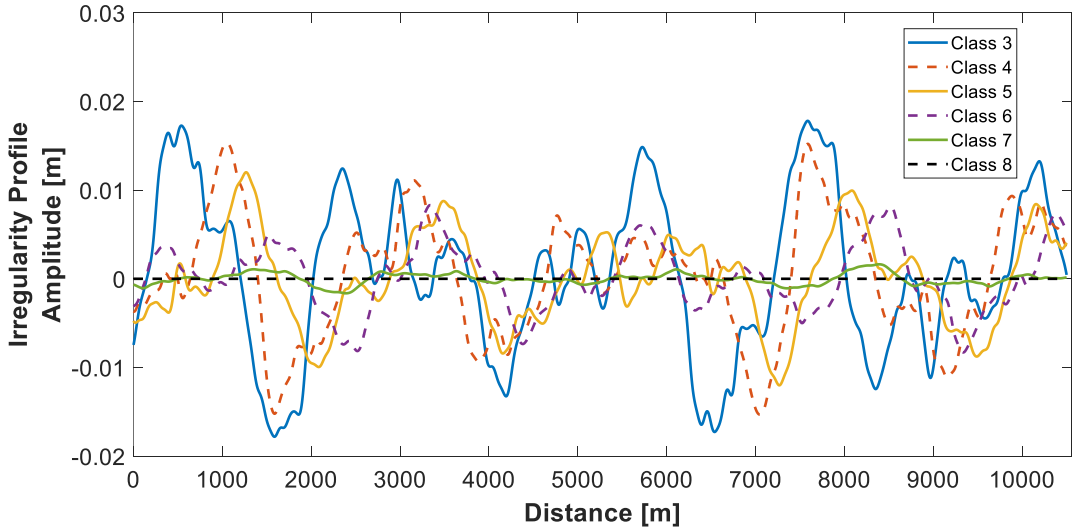

Figure 3-5 - Track irregularity profiles for classes 3 to 8. Adapted from Gonçalves et al. (2023)

As Figure 3-5 shows, lower irregularity profile classes present higher amplitudes and lower wavelengths as expected. Of particular interest are the differences between classes 6 and 7 and classes 7 and 8. The vast difference in amplitudes between these first two classes is noticeable compared to other consecutive classes, such as classes 3 and 4 or 5 and 6. Between classes 7 and 8 (theorical perfect track), it is remarkable how close the maximum amplitudes of the Northern Line profile track sample are to the

graphical representation of a theoretically perfect track throughout most of the development of the profiles.

3.4. NUMERICAL TRAIN MODEL

The train used for this study is the *Alfa Pendular* train that runs on the Portuguese Northern Line. The model for the train was developed using ANSYS® (2018), utilizing rigid beam FEs to model the various components of the car. These include the car body, the bogies and the wheelsets, each having mass elements to simulate the properties of those components in terms of mass and rotary inertia, and spring-dampers to model the suspensions.

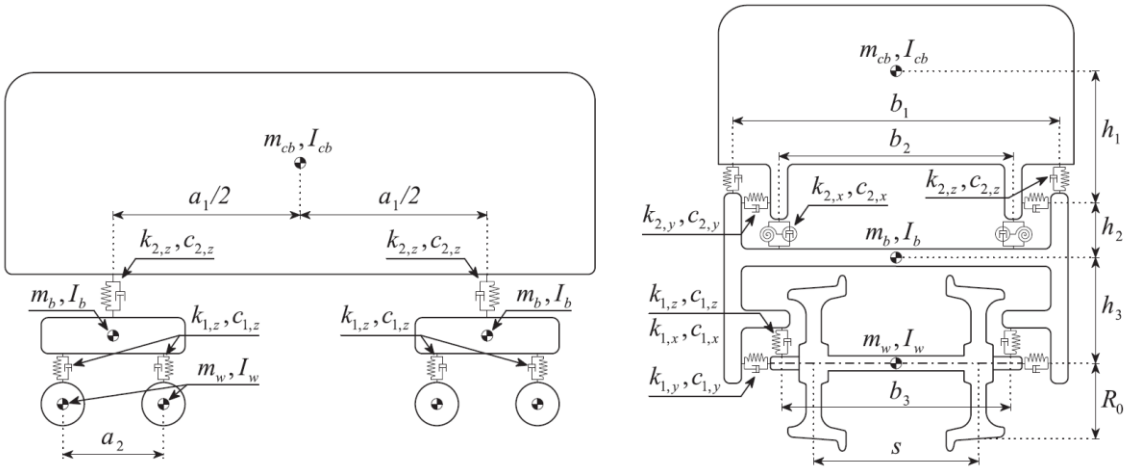

Figure 3-6 - Dynamic model of the railway vehicle lateral view (left) and front view (right). Taken from Mosleh et al. (2020b)

In Figure 3-6 a graphical representation of the train's dynamic model is presented. The stiffness, damping, concentrated mass, and rotational inertia of the train are respectively represented by the letters *k*, *c*, *m*, and *I*. The car body, the bogies, and the wheelsets are signalized by the subscripts *cb*, *b*, and *w*, respectively. Figure 3-6 also shows the longitudinal *a*, transversal *b*, and vertical *h* distances, as well as the gauge *s*, and nominal wheel radius R_0. For this work, only one car was considered in the calculations, but, in the future, more cars can be used.

3.5. TRAIN-TRACK INTERACTION

The train-track coupled model is the most fundamental aspect when analysing the interaction between the train and track. A significant number of models for this type of interaction are present in many literature arts, varying in complexity. Nonetheless, they generally share the same basic framework, consisting of coupling the train to the track using a wheel-rail contact model. In order to solve the dynamic interaction coupling system for the train-track model, the numerical tool "VSI-Vehicle-Structure Interaction Dynamic Analysis" is utilized, using the ANSYS® (2018) software. This tool is based on the Lagrange multipliers method, in which the constraint equations that connect the train displacements with the nodal displacements of the track, including the track irregularities, are added to

the equilibrium equations to form a single system that defines the coupling between the two sub-structures (Mosleh et al., 2021).

It should be noted that the analysis is greatly simplified when the track irregularities are included in the constraint equations rather than having to be explicitly included in the FEM model. It is also conceivable to add the profile of the wheel (wheel flat/wheel polygonisation) as a periodic rail irregularity, as explained later. A formulation created initially by Neves et al. (2012) and expanded in Montenegro et al. (2013) and Neves et al. (2014) was made to address the train structure separation. Later, Montenegro et al. (2015) revised the methodology to take into consideration the lateral interaction while taking into account the shape of the wheel and rail and their contact model.

For the wheel-rail contact model adopted in the numerical model mentioned above, a specially developed finite contact element considering the geometry of the contact interface serves as a basis. This is achieved by parameterising the wheel and rail profiles with cubic splines (Mosleh et al., 2021). The model was verified according to numerical examples and experimental data, as can be seen in Neves et al. (2012, 2014) and Montenegro et al. (2013, 2015). The element uses the Lagrange multipliers method and can result in the wheel-rail detachment, but also ensures coupling between the train and the track construction when contact happens. The contact formulation used in this contact element may be broken down into three main steps, namely:

- geometrical analysis;
- normal contact analysis;
- tangential contact analysis.

The contact points between the wheel and the rail are located using geometric analysis of the wheel and rail profiles that were previously parameterized using cubic splines. The contact search is then carried out utilizing a few nonlinear equations whose solutions guarantee the compatibility of the two interacting bodies. Montenegro et al. (2015) provides a thorough description of these procedures.

The dynamic coupling formulation used in this thesis was programmed in MATLAB® (2018) by importing the structural matrices of both the track and the train modelled in the FEM package ANSYS® (2018). Figure 3-7 shows a graphical representation of the train-track interaction numerical model, detailing which components were modelled in the ANSYS® (2018) software and in the MATLAB® (2018) software. A detailed description and validation of the interaction model can be found in Montenegro (2015) and Montenegro et al. (2015).

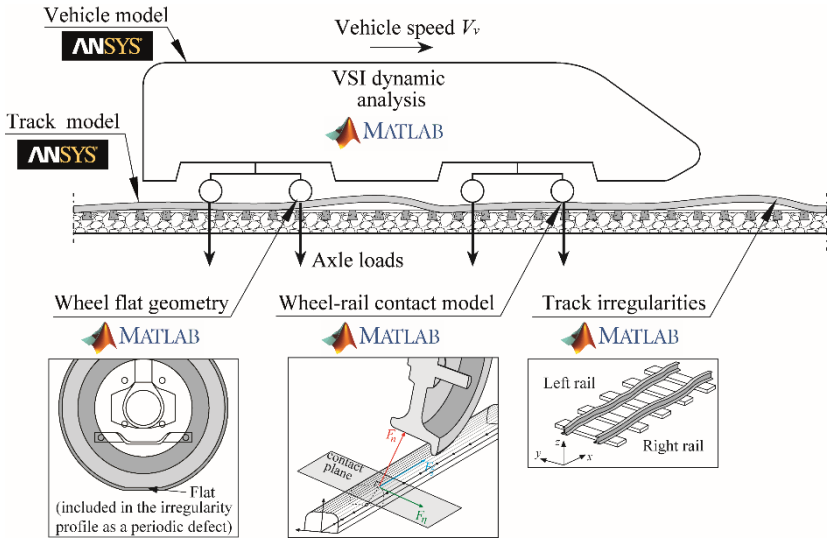

Figure 3-7 - Graphical representation of the the train-track interaction numerical model. Taken from Mosleh et al. (2022b)

4
ALGORITHM FOR WHEEL OOR DETECTION

This Chapter presents a description of the methodology utilised for the detection of defective wheels.

4.1. INTRODUCTION

As extensively mentioned in Section 2.2, a great number of methods to determine wheel OOR have been developed. The method implemented in this dissertation is based on an algorithm constructed in MATLAB® (2018) created for wheel flat detection with multiple records using spectral kurtosis analysis as proposed by Mosleh et al. (2021).

This algorithm analyses OOR of a moving train in a track, both modelled in ANSYS® (2018) and imported to MATLAB® (2018) as described in the previous Chapter, and it can be applied to a monitoring system composed by a set of strain gauges (SGs) or accelerometers installed along a specific stretch of a rail track.

4.2. METHODOLOGY FOR WHEEL DEFECT DETECTION

4.2.1. DEFINITION OF KURTOSIS

The relative intensity of the signal in comparison to a Gaussian distribution, measured by the non-dimensional quantity, is known as kurtosis. High kurtosis (K) levels are produced by signals that exhibit impulsive behaviour. According to Brandt (2011), it is defined as the fourth central moment (μ_4) divided by the square of variance (μ_2^2):

$$K = \frac{\mu_4}{\mu_2^2} \quad (5)$$

The kurtosis value for signals with impulsive features can be very high. As a result, a high amount of kurtosis indicates spikes in the data (Entezami et al., 2020). A method of detecting a defect in a wheel is to calculate the kurtosis for various frequency bands rather than the original signal, since a defect in the wheel causes a spike in the signal.

4.2.2. Detecting a Wheel Defect using the Envelope Spectrum Approach

As seen in Hasan (1983), the complex demodulation method known as envelope spectrum detection is used by shifting each frequency to zero and then applying a low-pass filter. To perform a complex signal deformation, the signal is multiplied by the following factor:

$$X(t) = R(t)exp\left(2\pi i\, f_0 t\right) \quad (6)$$

in which:

- f_0, is the centre frequency of the band.

After the frequency band with the highest kurtosis level is calculated, to obtain a higher impulse signal to analyse the envelope spectrum, a passband filter is applied to the raw signal. Figure 4-1 illustrates the procedure for detecting a damaged wheel. The method to detect a wheel flat is shown in this figure with two main blocks. In the first block of the flowchart, marked in green, the necessary equations and explanations to evaluate the envelope spectrum for each sensor of the installation system are explained. Moreover, in the second block, marked in blue, the wheel defect is identified based on the following criteria. If the responses obtained from all sensors are coincident, the amplitude of the envelope spectrum is the same and indicates the passage of a healthy wheel through the system. However, a significant lag in the amplitude of the envelope spectrum infers a passage of a defective wheel. More details regarding the algorithm in order to detect a defective wheel are provided by Mosleh et al. (2020b; 2021).

Demodulation band selection for envelope analysis of a defective wheel is often performed by comparing the spectrum of a healthy wheel to select specific frequencies where the greatest change has occurred as a result of the fault. It has been discovered that the spectral kurtosis (SK) gives a very similar indication of the band being demodulated without the need for historical data. The spectral kurtosis of a signal is obtained by dividing the original signal into different frequency bands and obtaining the kurtosis for each frequency band (Antoni, 2007). This shows how the peak of the signal changes with frequency and can be used to identify the frequency band where the signal has the most impulse behaviour. This information is needed to select the optimal frequency band for demodulation and perform an envelope analysis on the recorded signals. A combination of centre frequency and optimal bandwidth of a bandpass filter to maximize the kurtosis is described by a kurtogram (Antoni, 2006).

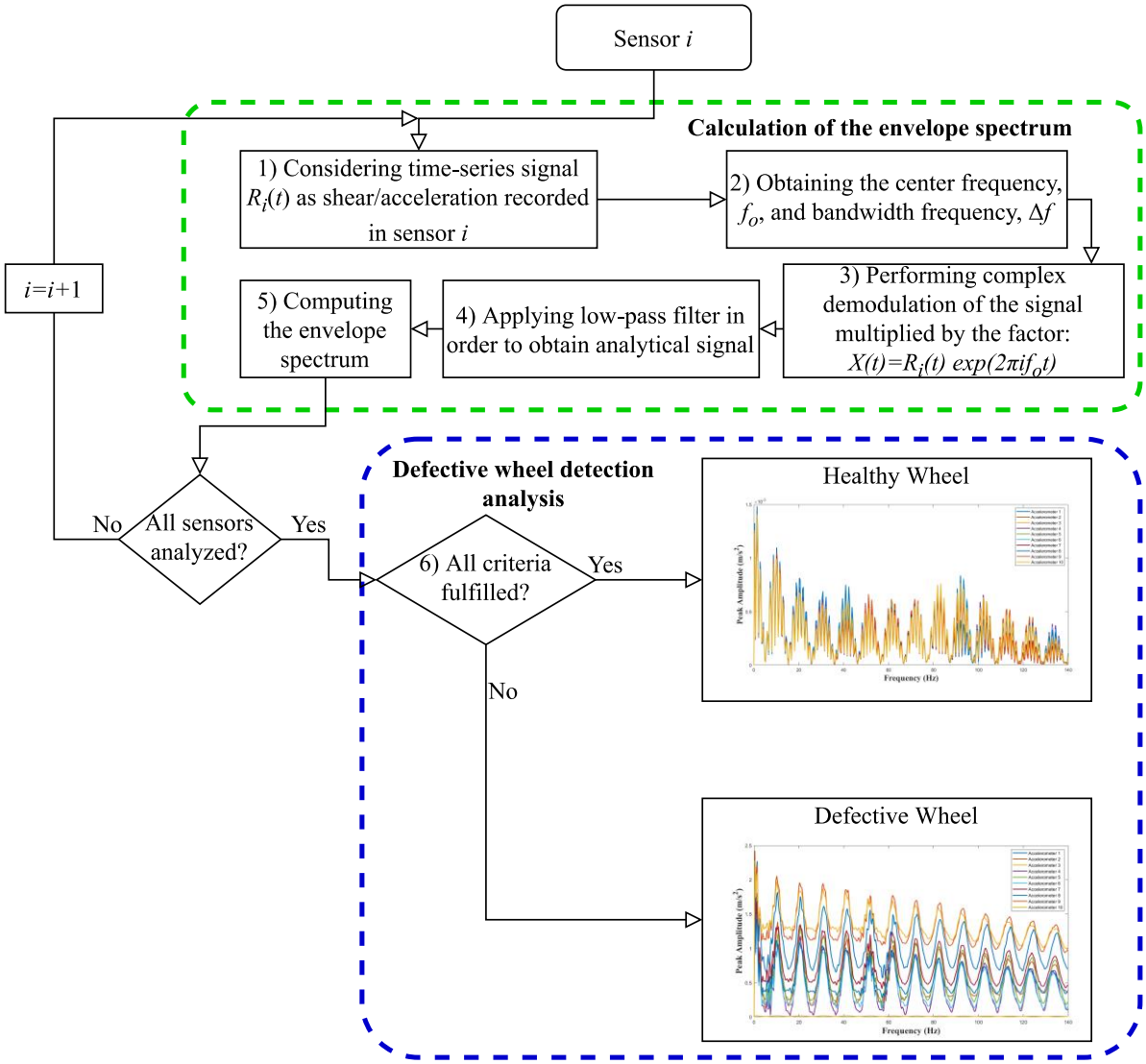

Figure 4-1 – Diagram of the methodology for identifying a defective wheel

The kurtogram is used to depict the spectral kurtosis and displays the kurtosis results for a variety of window lengths and frequencies. The multirate filter-bank structure is the foundation for the proposed approach to obtain the kurtogram (Antoni, 2006, 2007). First, the algorithm is explained for a binary tree structure, and then it is expanded to include a 1/3-binary tree structure. The procedure to perform a kurtogram is described in Mosleh et al (2021). Furthermore, the following equations, according to Antoni (2006, 2007), can be used to determine the centre frequency and bandwidth frequency for the level with the largest kurtosis:

$$\Delta f = 2^{(-l-1)} F_s \quad (7)$$

$$f_0 = (i + 0.5)\Delta f \quad (8)$$

in which:

- Δf, is the bandwidth;
- l, is the level of the coefficient series;
- F_s, is the sampling frequency;
- f_0, is the centre frequency;
- i, is the number of filters applied at level l.

Figure 4-2 shows the kurtogram using the above framework for a shear signal corresponding to the passage of the Alfa Pendular train. The maximum kurtosis is obtained as 3,204.5107 at level 2.6, corresponding to the band frequency $[\frac{1}{12}\ \frac{1}{6}]$. Therefore, the centre and bandwidth frequencies for the corresponding signal, taking into account Equations (7) and (8), are determined as follows:

$$\Delta f = 2^{(-2.6-1)} * 10000 = 824.69\ Hz$$
$$f_0 = (1 + 0.5) *\ 824.69 = 1237.03\ Hz$$

where the sampling frequency F_s is 10,000 Hz, the bandwidth frequency, Δf, is 824.69 Hz and the centre frequency, f_0, is 1,237.03 Hz. More details regarding the envelope spectrum approach for wheel flat detection are presented in Mosleh et al. (2020b; 2021).

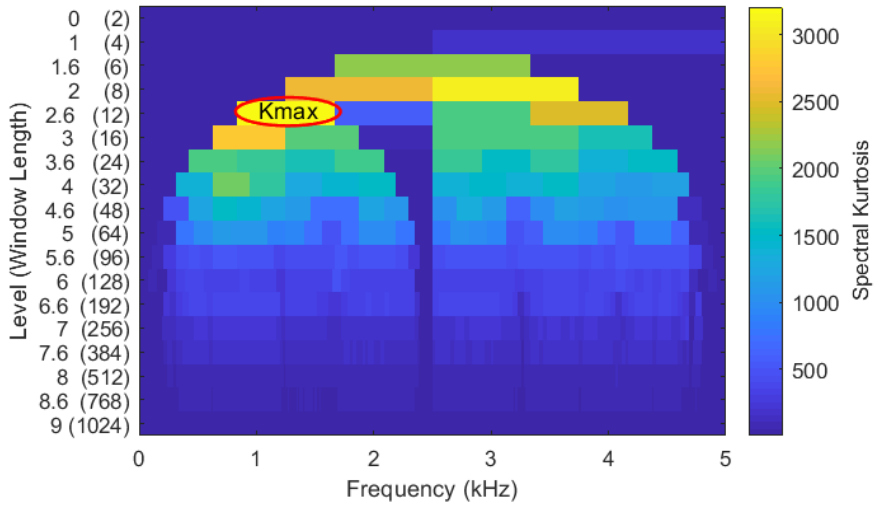

Figure 4-2 - Spectral kurtosis for a shear signal corresponding to the *Alfa Pendular* train, showing the maximum kurtosis, optimal window length, centre frequency, and bandwidth frequency

5
CASE STUDIES

This Chapter presents: i.) a description of the geometrical and mechanical properties of the *Alfa Pendular* train utilised in the analyses; ii.) a description of the multi-sensor array layout of the monitoring system; iii.) the geometry and modelling of a wheel flat and a polygonised wheel; iv.) the analysed conducted to detect wheel flats and polygonised wheels for the passage of mentioned train; v.) a comparison between the analyses realised; and vi.) commentary on the results obtained from the analyses.

5.1. INTRODUCTION

The analyses conducted in this study involve a passage of one vehicle of *Alfa Pendular* train passing through a section of track at different speeds. The track segment meanwhile presents the irregularity profiles of the rail shown in Figure 3-5. Only the right wheel of the first wheelset is considered as a defective wheel for the purposes of the analyses. Three layout schemes were taken into consideration in this study. The track section has a total length of 150 metres. The virtual sensors are located along a slight stretch of 3.00 metres.

Table 5-1 displays the geometrical and mechanical characteristics of the vehicle used in the analyses, whose parameters are represented in Figure 3-6. The values in the table were adopted from Mosleh et al. (2020b; 2021).

Table 5-1 - Geometrical and mechanical properties of the *Alfa Pendular* train. Values from Mosleh et al. (2020b; 2021)

Parameter	Value
Car body mass, m_{cb}	35,640 kg
Car body roll moment of inertia, $I_{cb,x}$	55,120 kg m^2
Car body pitch moment of inertia, $I_{cb,y}$	1,475,000 kg m^2
Car body yaw moment of inertia, $I_{cb,z}$	1,477,000 kg m^2
Bogie mass, m_b	2829 kg
Bogie roll moment of inertia, $I_{b,x}$	2700 kg m^2
Bogie pitch moment of inertia, $I_{b,y}$	1931.49 kg m^2
Bogie yaw moment of inertia, $I_{b,z}$	3878.76 kg m^2
Wheelset mass, m_w	1711 kg
Wheelset roll moment of inertia, $I_{w,x}$	733.4303 kg m^2
Wheelset yaw moment of inertia, $I_{w,z}$	733.4303 kg m^2
Stiffness of the primary longitudinal suspension, $k_{1,x}$	44,981,000 N/m

Stiffness of the primary transversal suspension, $k_{1,y}$	30,948,200 N/m
Parameter (cont.)	Value (cont.)
Stiffness of the primary vertical suspension, $k_{1,z}$	1,652,820 N/m
Damping of the primary vertical suspension, $C_{1,z}$	16,739 N s/m
Stiffness of the secondary longitudinal suspension, $k_{2,x}$	4,905,000 N/m
Stiffness of the secondary transversal suspension, $k_{2,y}$	2,500,000 N/m
Stiffness of the secondary vertical suspension, $k_{2,z}$	734,832 N/m
Damping of the secondary longitudinal suspension, $C_{2,x}$	400,000 N s/m
Damping of the secondary transversal suspension, $C_{2,y}$	17,500 N s/m
Damping of the secondary vertical suspension, $C_{2,z}$	35,000 N s/m
Static load transmitted by each wheel	64,000 N
Longitudinal distance between bogies, a_1	19 m
Longitudinal distance between wheelsets, a_2	2.7 m
Transversal distance between vertical secondary suspensions, b_1	2.144 m
Transversal distance between longitudinal secondary suspensions, b_2	2.846 m
Transversal distance between primary suspensions, b_3	2.144 m
Vertical distance between car body centre and secondary suspension, h_1	0.936 m
Vertical distance between bogie centre and secondary suspension, h_2	0.142 m
Vertical distance between bogie centre and wheelset centre, h_3	0.065 m
Nominal rolling radius, R_0	0.43 m
Gauge, s	1.67 m

The analyses are divided into three groups: i.) analyses for wheel flat detection, presented in section 5.2; ii.) analyses for wheel polygonization detection, shown in section 5.3 and iii.) influence of one defective wheel in a wheelset on both rails of the track.

5.1.1. Layout of the Multi-Sensor Array of the Monitoring System

In the last few decades, several academics have suggested various in-service techniques for assessing wheel problems, including onboard and wayside tests. The majority of onboard methods rely on vibration, acoustic, image detection, and ultrasonic technology (Amini, Entezami, & Papaelias, 2016; Bosso et al., 2018; Cavuto et al., 2016; Zhang et al., 2017). However, for comprehensive diagnosis and effective wheel management, sensors must be installed on all wheels.

Due to cost and maintenance concerns, sensors installed on wheels are rarely employed; instead, onboard detection techniques are frequently used to monitor the status of the track rather than the condition of the wheels. In contrast, wayside measurement systems are currently an ideal solution to detect wheel defects, as the condition of all wheels evaluates during the passage of trains (Alexandrou et al., 2016; Amini et al., 2016; Colaço et al., 2016; Kouroussis et al., 2016; Meixedo et al., 2016; Neves et al., 2019; Mosleh et al., 2019; 2020a; Gonçalves et al., 2023). A quantitative decision-making method based on wheel impact data that depicts the real state of the wheels was proposed by Stratman et al. (2007).

The algorithm used in this research considers the measurements of a monitoring system composed of a sensor array that evaluates shear and accelerations in the rail when a defective wheel passes through it. The monitoring system considers a total of 16 positions where the sensors are located in the track, as illustrated in Figure 5-1.

In Figure 5-1 the sensors are also split into 3 different layouts in order to visualise the location of the SGs and de accelerometers. The numbers 1 to 10 represent the rail-mounted sensors that simulate the position of the SGs shown in layout 1 and the accelerometers shown in layout 2. These points evaluate shear force and acceleration. Numbers 11 to 16 represent only acceleration measurement points (layout scheme 3), which represent the position of the accelerometers installed on the rail over the sleepers.

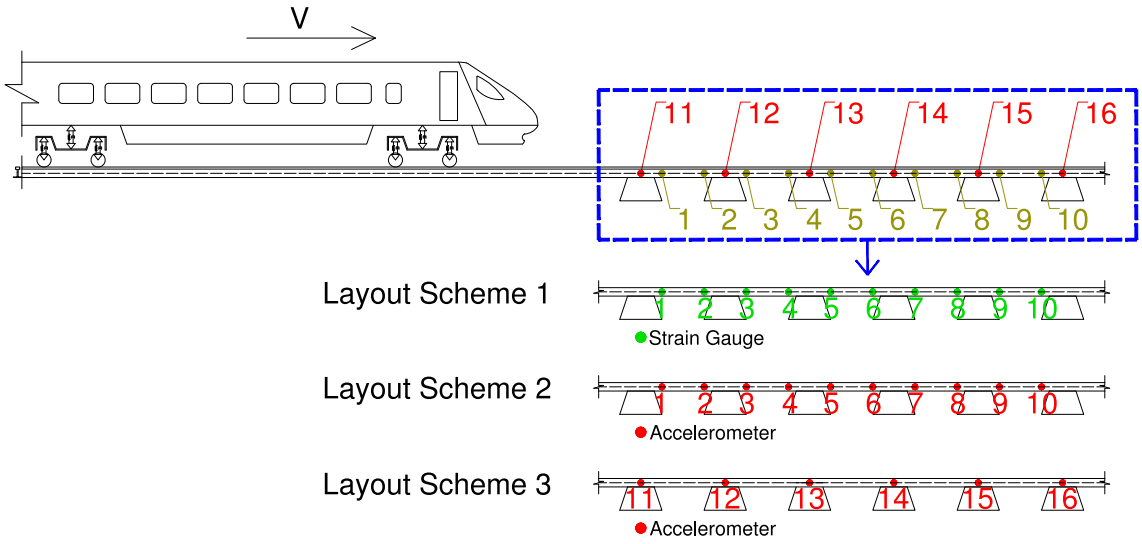

Figure 5-1 - Schematics of a train containing a defective wheel and the SG and Accelerometer sensors locations. Adapted from Gonçalves et al. (2023)

Wheel defects were detected through the envelope spectrum approach by considering the evaluated shear and the accelerations as inputs, obtained by the strain gauge and accelerometer sensors located on the track section.

5.1.2. WHEEL DEFECT GEOMETRY

Figure 5-1 shows a train passing through the virtual sensors. The front wheel of the vehicle has a defect that is expected to be detected by the sensors during the analysis. The type of wheel defect can be either: i.) a wheel flat; ii.) a wheel with a degree of polygonization.

Flat Geometry

A wheel flat is mainly characterised by the wheel flat length (L) and the flat depth (D), calculated according to Equation (9) (Zhai et al., 2001).

$$D = \frac{L^2}{16 r_w} \quad (9)$$

in which r_w is the radius of the wheel.

The wheel flat vertical profile deviation (Z) is defined as:

$$Z = -\frac{D}{2}\left(1 - cos\frac{2\pi x}{L}\right)H\left(x - (2\pi r_w - L)\right), 0 \leq x \leq 2\pi r_w \quad (10)$$

in which H stands for the Heaviside function.

Figure 2-6 depicts an illustration of a wheel flat showing the flat length and depth. When a defective wheel rotates, the flat of the wheel causes a periodic impulse to be applied to the track with a particular frequency. The frequency of the periodic impulse corresponding to the flat impact frequency (f_f) can be determined as follows:

$$f_f = \frac{V}{(2\pi r_W)} \quad (11)$$

in which:

- V, is the train speed;
- r_w, is the radius of the wheel.

Polygonization Geometry

In order to replicate the effects of wheel polygonization, the circumferential irregularity for the wheel has to be modelled. The wavelengths λ_θ correspond to the lowest 20 harmonic orders of a polygonised wheel and can be defined, as noted in the work of Johansson & Andersson (2005), as:

$$\lambda_\theta = \frac{2\pi r_w}{\theta}, (\theta = 1, 2, 3, \ldots, 20) \quad (12)$$

in which θ is the integer harmonic order, and r_w is the wheel radius.

The OOR will cause a simultaneous wheel-rail excitation at many frequencies in a specific frequency range, depending on the train speed. The following formula determines the wheel irregularity level spectrum L_w (in dB re 1 μm):

$$L_w = 20\log_{10}\left(\frac{\hat{w}}{w_{ref}}\right) \quad (13)$$

in which $\hat{w}$ is the root mean square value of the irregularity profile $w(x_w)$, evaluated for wavelengths corresponding to each OOR order, and w_{ref} = 1 μm. Figure 5-2 depicts examples of polygonised wheels with 2, 3 and 4 harmonic orders.

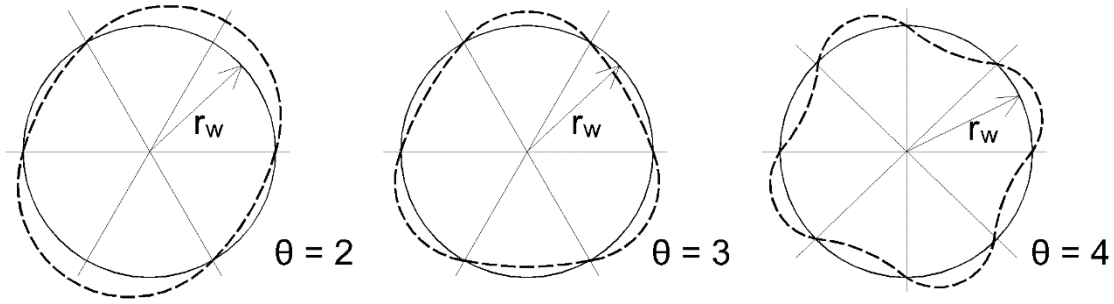

Figure 5-2 - Schematics of wheel polygonization with 2 harmonic orders (left), 3 harmonic orders (middle), and 4 harmonic orders (right). r_w is the radius of the wheel

The initial irregularity profile is modelled as a sum of sine functions (M = 20):

$$w(x_w) = \sum_{\theta=1}^{M} a_\theta \sin\left(\frac{2\pi}{\lambda_\theta} x_w + \psi_\theta\right) \quad (14)$$

The initial wheel irregularity level spectrum used in the simulations is chosen to roughly match an empirical formula identified by measured data from new wheels as follows:

$$L_{w\theta} = 24.7 \log_{10}(\lambda_\theta) + 8.47 \quad (15)$$

The amplitude of the sine function for each wavelength is obtained as:

$$a_\theta = \sqrt{2} * 10^{\frac{L_{w\theta}}{20}} * w_{ref} \quad (16)$$

Different wheel irregularities defined by the same spectrum are generated by assuming phase angles to the sine functions that are uniformly and randomly distributed between 0 and 2π. The generated polygonization is then applied to the elements defining the geometry of the wheel surface.

5.2. WHEEL FLATS

The variables studied for wheel flat detection were: i.) speed of the train; ii.) wheel flat geometry and iii.) track profile irregularity. Three-wheel flat profiles were analysed in this study, along with a healthy wheel profile. The values of *L* and *D*, as defined in Figure 2-6, for the three-wheel flats are as follows:

- for the first wheel flat profile, nominated as *wf1*, *L*=20 mm and *D* = 0.058 mm;
- for the second wheel flat profile, nominated as *wf2*, *L*=80 mm and *D* = 0.93 mm;
- for the third wheel flat profile, nominated as *wf3*, *L*=140 mm and *D* = 2.80 mm.

By analysing the wheel flat profiles, it was possible to determine the location of the flat impact within the stretch of track analysed. Figure 5-3 shows the areas of the flat impact for the three wheel flat profiles studied.

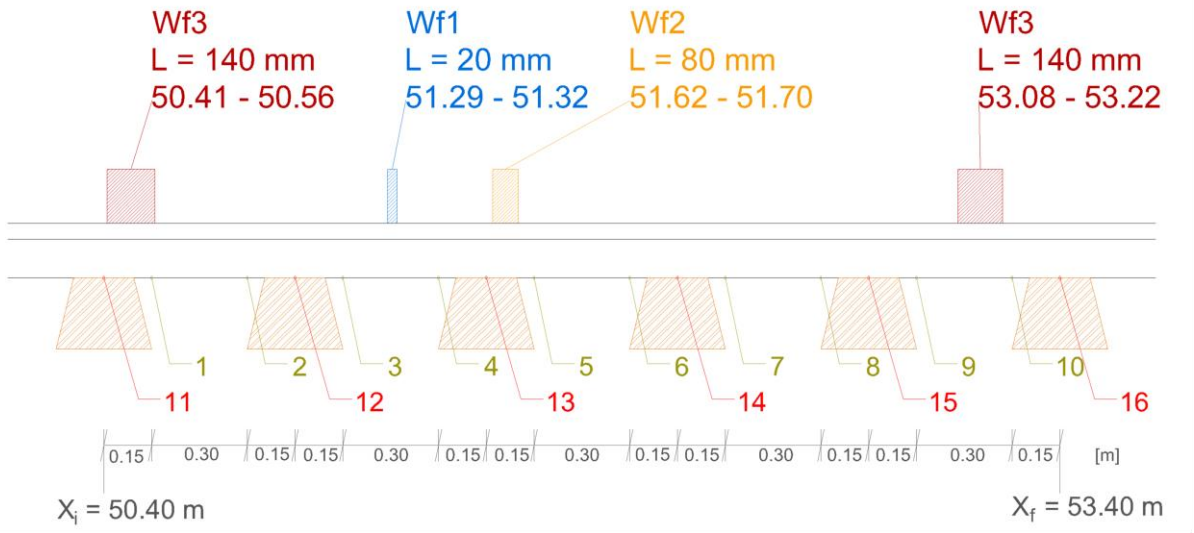

Figure 5-3 - Scheme of the wheel flat impact areas within the track section, as well as the location of each sensor. X_i is the beginning of the track section, X_f is the end of the track section

The track irregularity profiles are the same as the ones presented in Figure 3-5, from classes 3 to 8. The train speeds, *V*, analysed were 60 km/h, 100 km/h, and 140 km/h. Due to speed restrictions imposed for each track irregularity profile according to the FRA, the following track unevenness profiles were considered for each speed (Mosleh et al., 2020a):

- for a train speed *V*=60 km/h, all the irregularity profile classes were used (classes 3 to 8);
- for a train speed *V*=100 km/h, classes 4 to 8 were analysed;
- for a train speed *V*=140 km/h, only classes 6, 7 and 8 were considered.

5.2.1. Wheel Flat Detection by the Response Obtained from the Accelerometers

The following figures present the acceleration responses of the envelope signal for the defective and healthy wheels corresponding to the 16 accelerometers evaluated on the rail (positions 1 to 10 of layout scheme 2 and positions 11 to 16 of layout scheme 3 shown in Figure 5-1). The use of strain gauges for long-term monitoring of wheel flat is inappropriate because of their susceptibility to water and electromagnetic interferences. Thus, accelerometers and SGs were both set up in the same location to compare track responses, as shown in layout scheme 1 and 2 from Figure 5-1.

It was crucial to minimize the number of sensors without compromising the quality of output results in order to reduce installation and maintenance costs. Furthermore, it was critical to show that the system consistently detects wheel defects independent of the sensors location. Therefore, six additional accelerometers (positions 11 to 16 indicated in Figure 5-1) were considered on the rail above each sleeper (layout scheme 3 from Figure 5-1).

Influence of the Train Speed and the Track Irregularity Profiles

Figure 5-4 to Figure 5-6 show the influence of train speed in wheel flat detection. Six rail unevenness profiles (classes 3-8) are considered and the wheel flat present in the train is "*wf1*". Figure 5-4 presents the envelope spectrum analyses for the 10 Accelerometers between the sleepers for the *Alfa Pendular*, considering train speed *V*=60 km/h. Figure 5-5 shows the envelope spectrum analyses for the 10 Accelerometers considering train speed *V*=100 km/h. Finally, Figure 5-6 illustrates the envelope spectrum analyses considering train speed *V*=140 km/h.

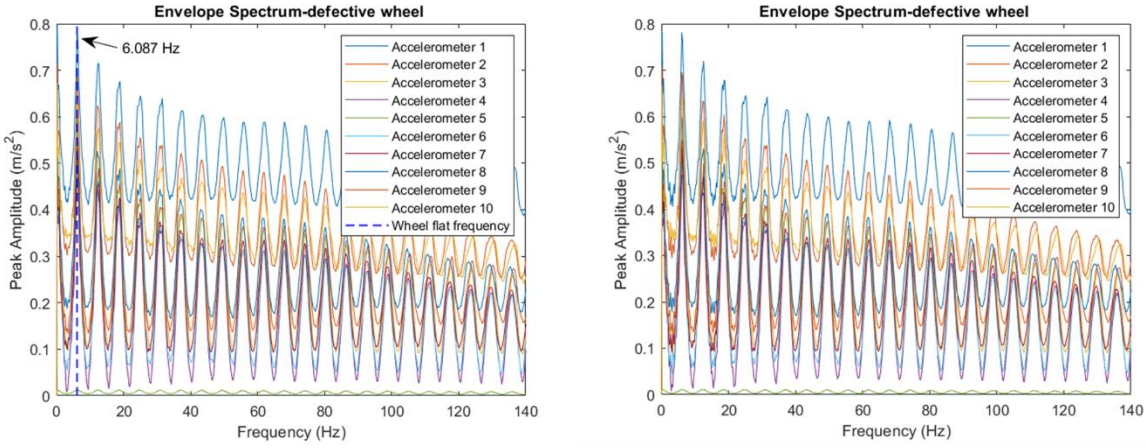

(**a**) (**b**)

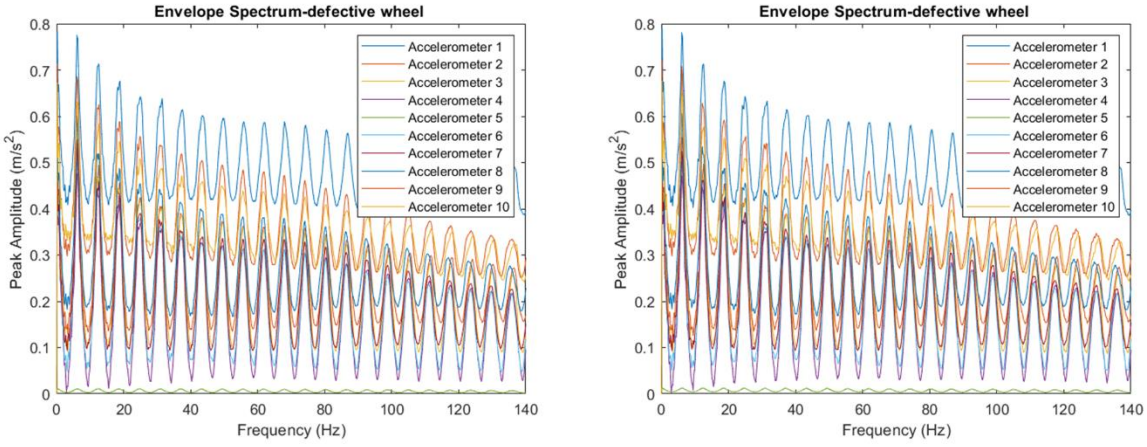

(**c**) (**d**)

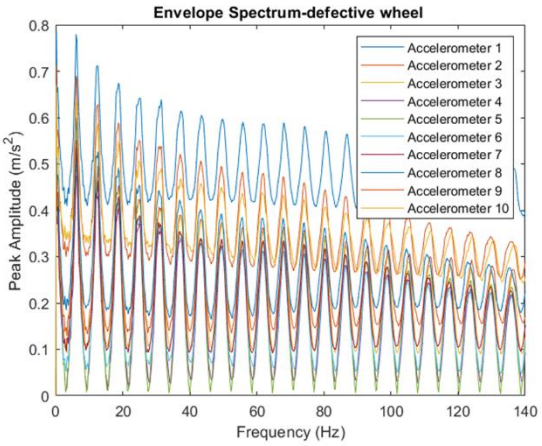

(**e**)

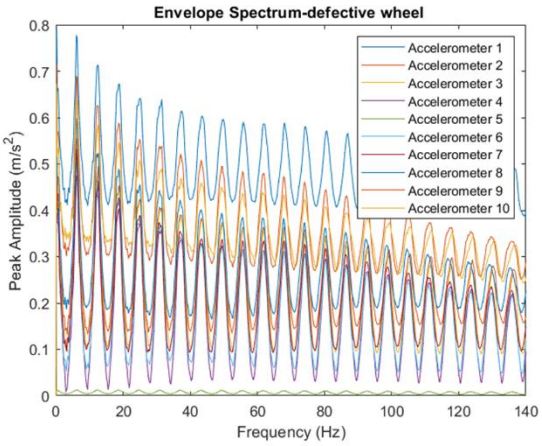

(**f**)

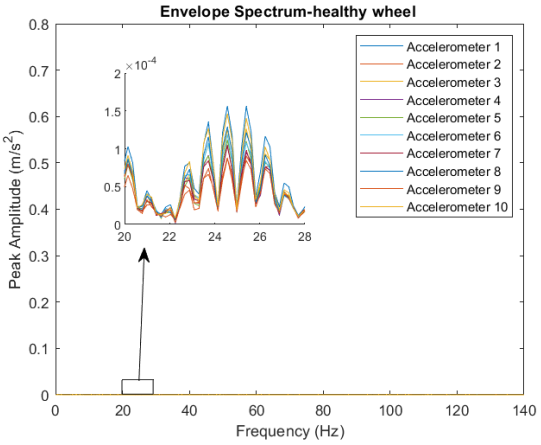

(**g**)

Figure 5-4 - Envelope spectrum analyses for the 10 Accelerometers between the sleepers (layout scheme 2) for the *Alfa Pendular*, considering train speed ***V*=60 km/h** and *wf1* wheel flat profile: (**a**) class 3 track irregularity profile; (**b**) class 4 track irregularity profile; (**c**) class 5 track irregularity profile; (**d**) class 6 track irregularity profile; (**e**) class 7 track irregularity profile; (**f**) class 8 track irregularity profile; (**g**) control analyses with: train speed ***V*=60 km/h**, class 8 irregularity profile, and healthy wheel

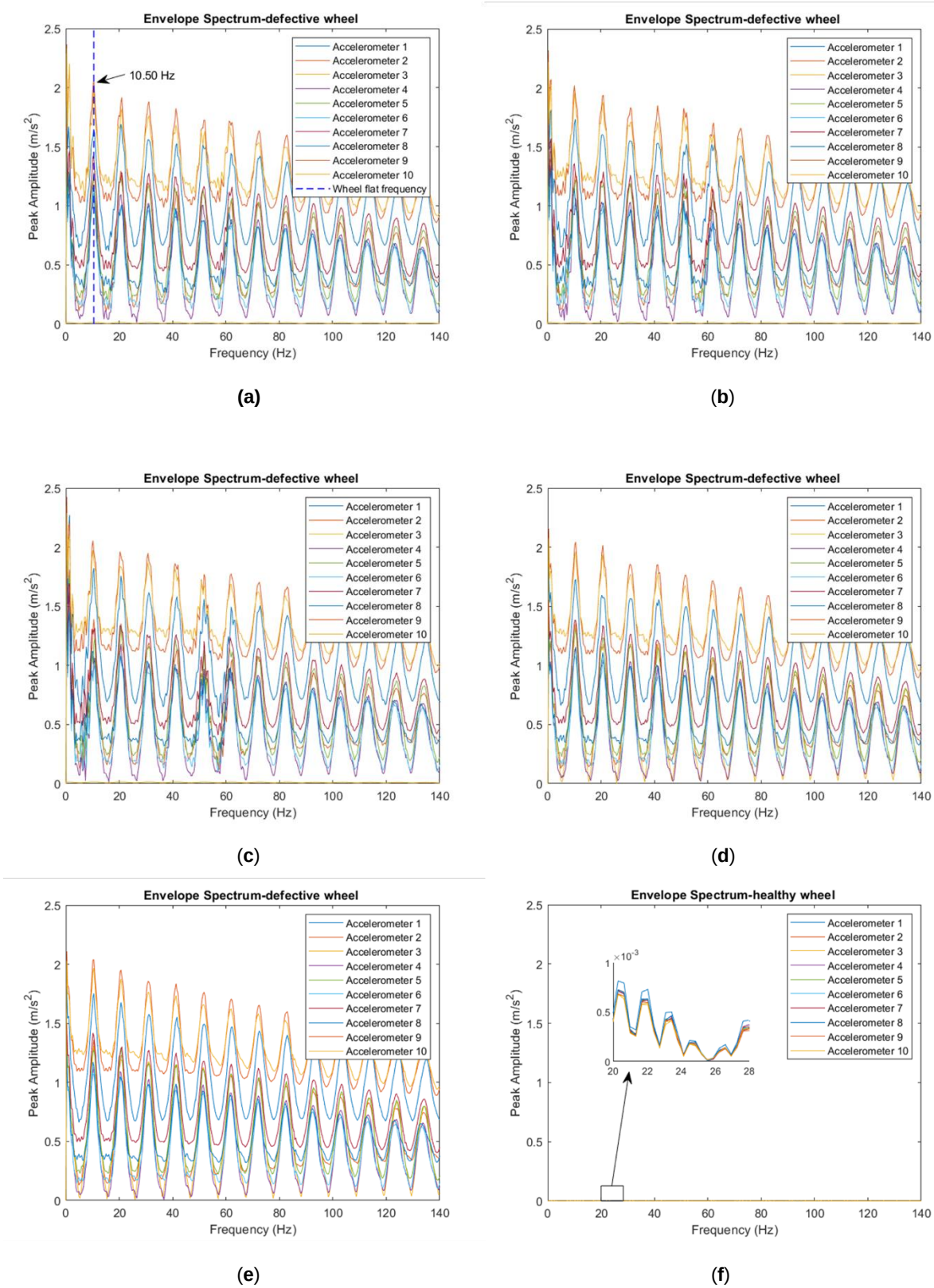

Figure 5-5 - Envelope spectrum analyses for the 10 Accelerometers between the sleepers (layout scheme 2) for the *Alfa Pendular*, considering train speed ***V*=100** km/h and *wf1* wheel flat profile: (**a**) class 4 track irregularity profile; (**b**) class 5 track irregularity profile; (**c**) class 6 track irregularity profile; (**d**) class 7 track irregularity profile;

(**e**) class 8 track irregularity profile; (**f**) control analyses with: train speed ***V*=100 km/h**, class 8 irregularity profile, and healthy wheel

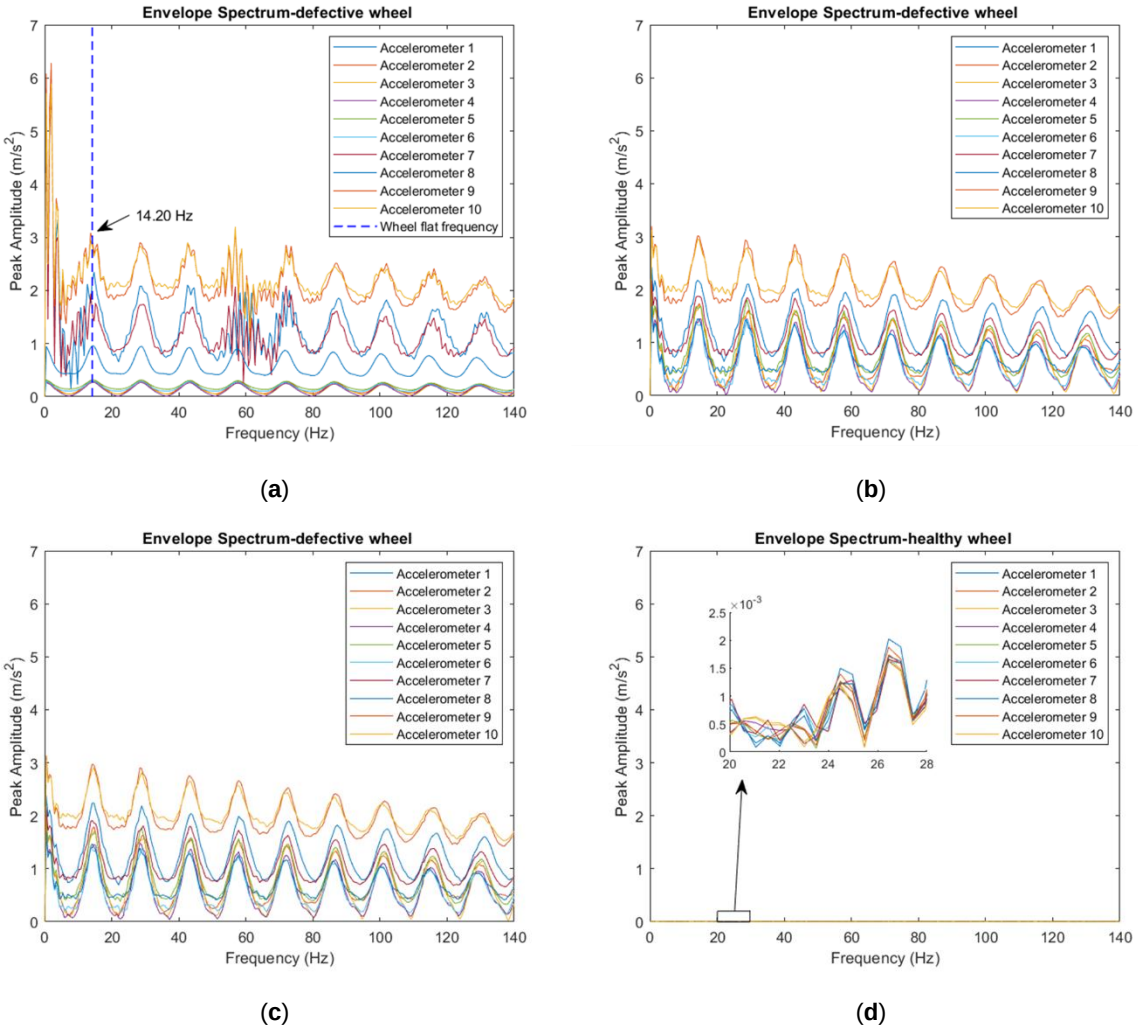

Figure 5-6 - Envelope spectrum analyses for the 10 Accelerometers between the sleepers (layout scheme 2) for the *Alfa Pendular*, considering train speed ***V*=140 km/h** and *wf1* wheel flat profile: (**a**) class 6 track irregularity profile; (**b**) class 7 track irregularity profile; (**c**) class 8 track irregularity profile; (**d**) control analyses with: train speed ***V*=140 km/h**, class 8 irregularity profile, and healthy wheel

The responses of each accelerometer regarding envelope spectrum (Figure 5-4, Figure 5-5 and Figure 5-6) show a significant lag for the scenarios where a wheel flat is present. This is expected for all occurrences of wheel flat analyses. When a healthy wheel is present, the response lag is insignificant. This indicates that there is no defective wheel present in the analyses. Looking at Figure 5-4, Figure 5-5 and Figure 5-6 it appears that the track quality generally does not influence in the detection of wheel flat, as the amplitude differences between different track irregularity profiles for the same train speed, *V*, and wheel flat are insignificant, with the exception of Figure 5-6(**a**). Train speed influenced the accelerometer responses, as higher speeds lead to higher peak amplitude values.

Another indicator that demonstrates the presence of a wheel flat is the amplitude variation of the envelope spectral signal. Disregarding the first peak on the control analyses, the amplitude variation of the envelope spectral signal of a defective wheel is higher than a healthy one. According to Equation (11), for a train speed of 60, 100 and 140 km/h, the flat impact frequency is calculated as 6.17, 10.28 and 14.4 Hz. Comparing the theoretical values to the ones obtained from the analyses (6.087, 10.50 and 14.20 Hz, respectively), as indicated in the above figures, they are very similar, validating the accuracy of the algorithm.

Influence of the Wheel Flat Profiles

Figure 5-7 compares accelerometer amplitude responses using different wheel flat profiles. Vehicle speed is considered as V=100 km/h and the track irregularity profile belong to "class 7".

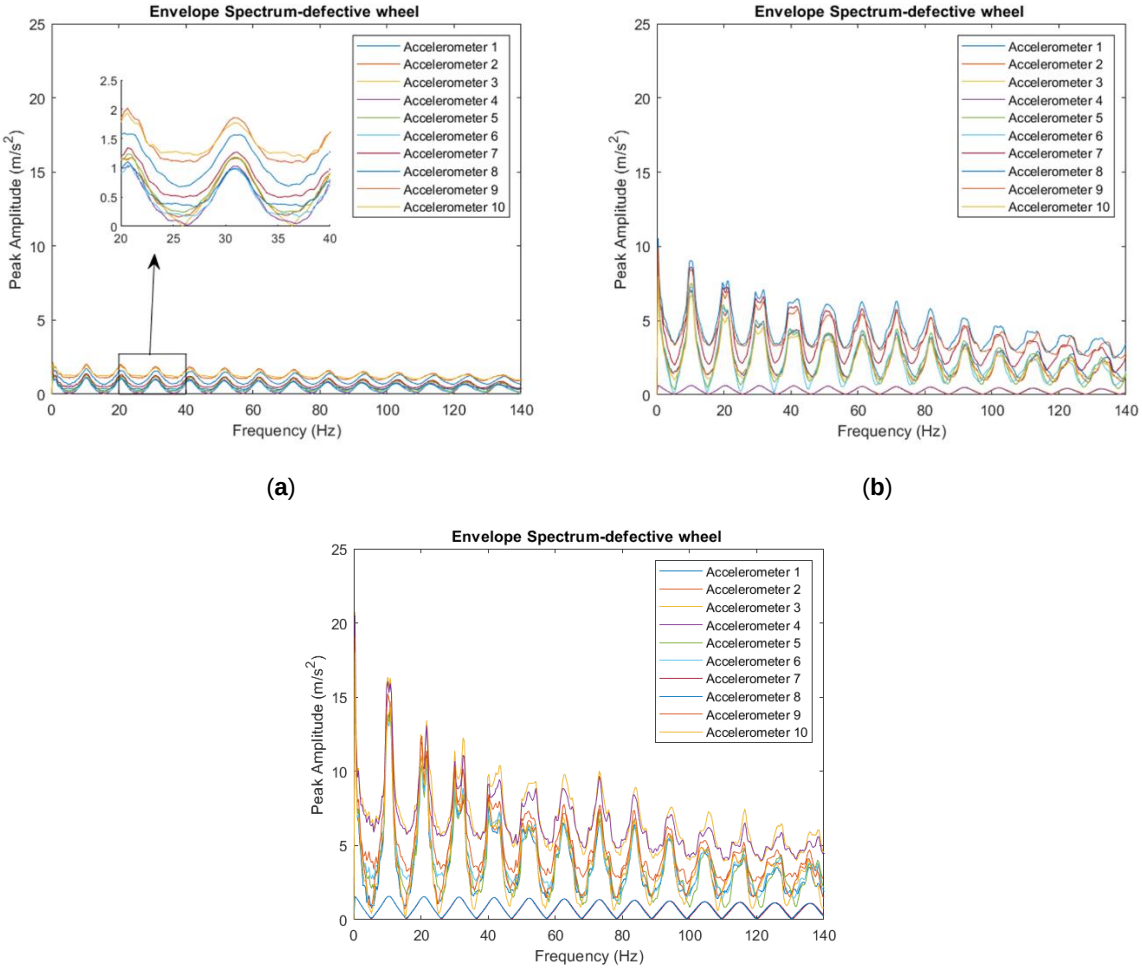

(**a**) (**b**)

(**c**)

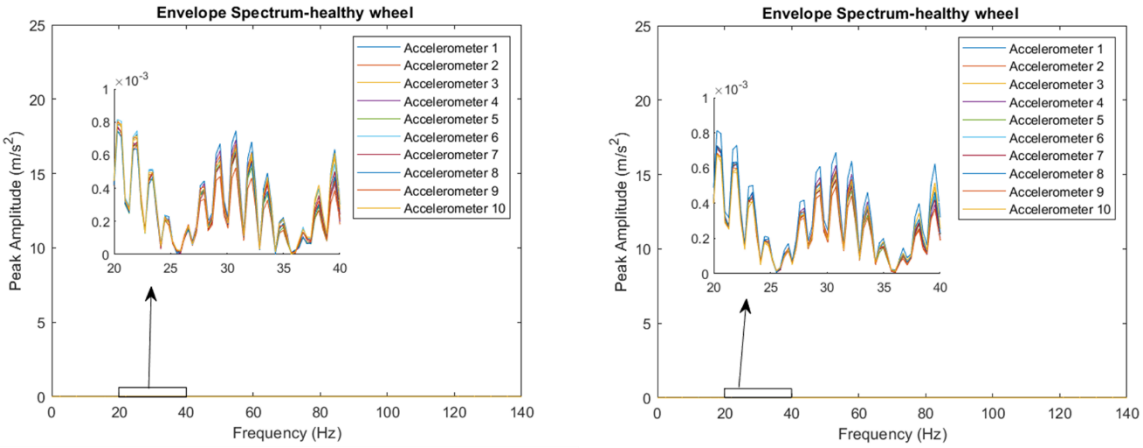

(**d**) (**e**)

Figure 5-7 - Envelope spectrum analyses for the 10 Accelerometers between the sleepers (layout scheme 2) for the Alfa Pendular, considering train speed V=100 km/h and class 7 track irregularity profile: (**a**) ***wf1*** wheel flat profile; (**b**) ***wf2*** wheel flat profile; (**c**) ***wf3*** wheel flat profile; (**d**) control analyses with: train speed *V*=100 km/h, class 7 irregularity profile, and **healthy wheel**; (**e**) control analyses with: train speed *V*=100 km/h, class 8 irregularity profile, and **healthy wheel**

The accelerometers shown in Figure 5-7 reveal that larger wheel flat (*L*) leads to higher peak amplitude responses, while in the healthy wheel, all signals coincide. Results from Figure 5-7(**d**) (Portuguese railway irregularity profile/"class 7" and healthy wheel) were very similar to the ones seen in Figure 5-7(**e**) prefect class ("class 8"), also with healthy wheel, having all signals coincide.

Influence of the Accelerometer Position

As mentioned before, six additional accelerometers (places 11 to 16 indicated in Figure 5-1) were taken into consideration on the rail on top of the sleepers in addition to the 10 positions chosen on the rail between two sleepers (layout scheme 3). The envelope spectrum approach is used to verify the sensitivity of layout scheme 3, considering the unevenness profile "class 7", the irregularity profile derived from a Northern Line track section. The vehicle speed is considered as 100 km/h.

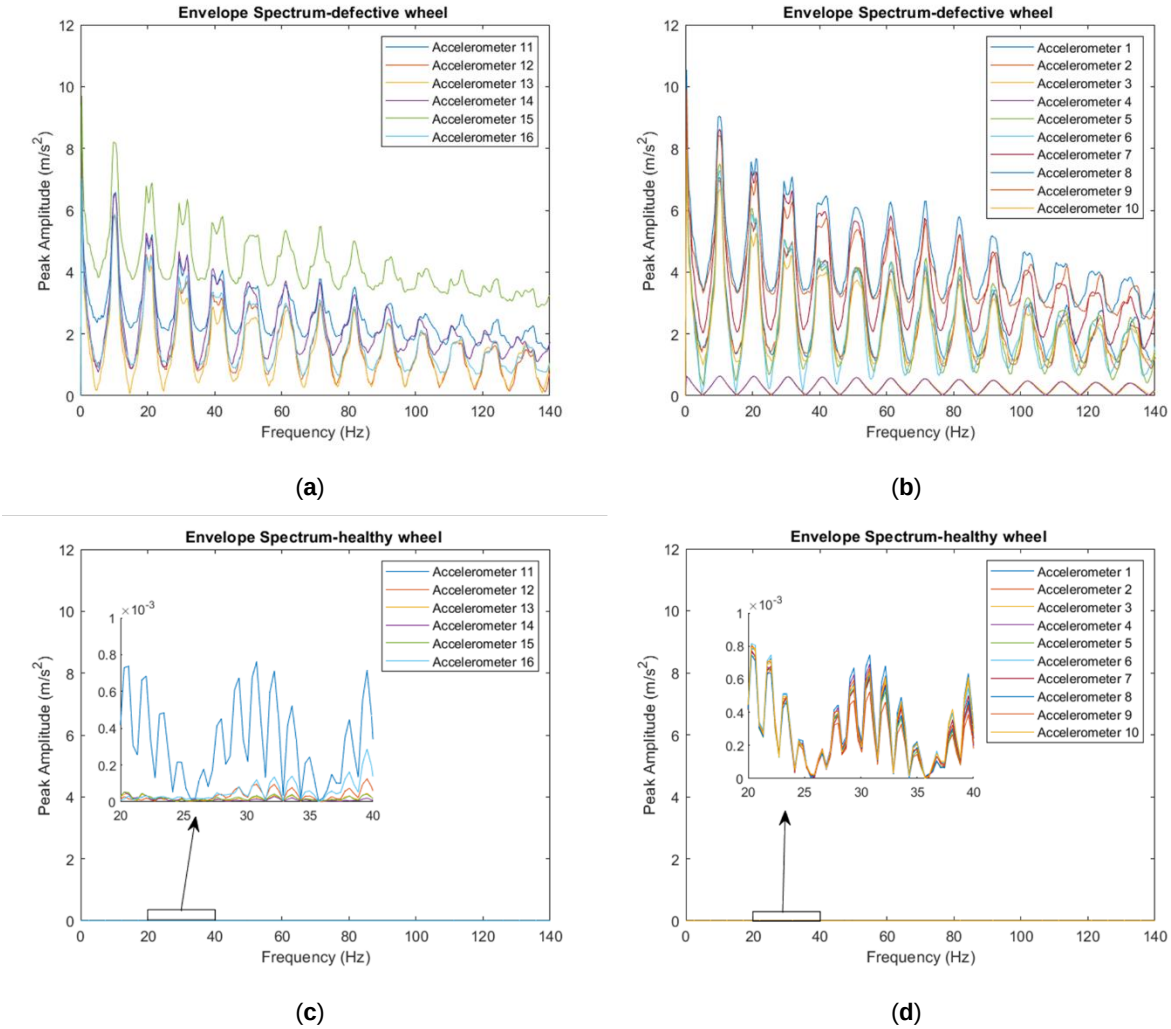

Figure 5-8 - Comparison between envelope spectrum analyses for the Accelerometers located on the sleepers (layout scheme 3) and for the Accelerometers located between the sleepers (layout scheme 2) for the Alfa Pendular, considering train speed V=100 km/h and class 7 track irregularity profile: (**a**) **layout 3** and *wf2* wheel flat profile; (**b**) **layout 2** and *wf2* wheel flat profile; (**c**) control analyses from **layout 3** with: train speed V=100 km/h, class 7 irregularity profile, and healthy wheel; (**d**) control analyses from **layout 2** with: train speed V=100 km/h, class 7 irregularity profile, and healthy wheel

Figure 5-8 illustrates a comparison with the envelope spectrum detection analyses for six accelerometers located on the rail above sleepers (layout 3) and he 10 accelerometers placed on the rail between 2 sleepers (layout 2) for a healthy wheel and a defective one. The outcomes are in line with what was discovered in earlier parts. The maximum peak amplitudes shown for the accelerometers installed on top of the sleepers (Figure 5-8(**a**)) were slightly lower than those observed for the accelerometers located between the sleepers (Figure 5-8(**b**)). This is due the damping effect of the sleepers themselves, which absorb some of the impact forces. Values for healthy wheel (Figure 5-8(**c**),(**d**)) are also in accordance with each other. It can be concluded that the position of the accelerometers does not affect in a significant way the detection of wheel flats.

5.2.2. Relation Between Wheel Flat Profile, Train Speed and Maximum Acceleration Peak Amplitude

To summarize the results from the analyses shown above, Figure 5-9 presents, for the Portuguese Northern Line track profile, the relation between train speed, *V*, wheel flat profile and maximum peak amplitude response obtained across all the accelerometers from layout scheme 2.

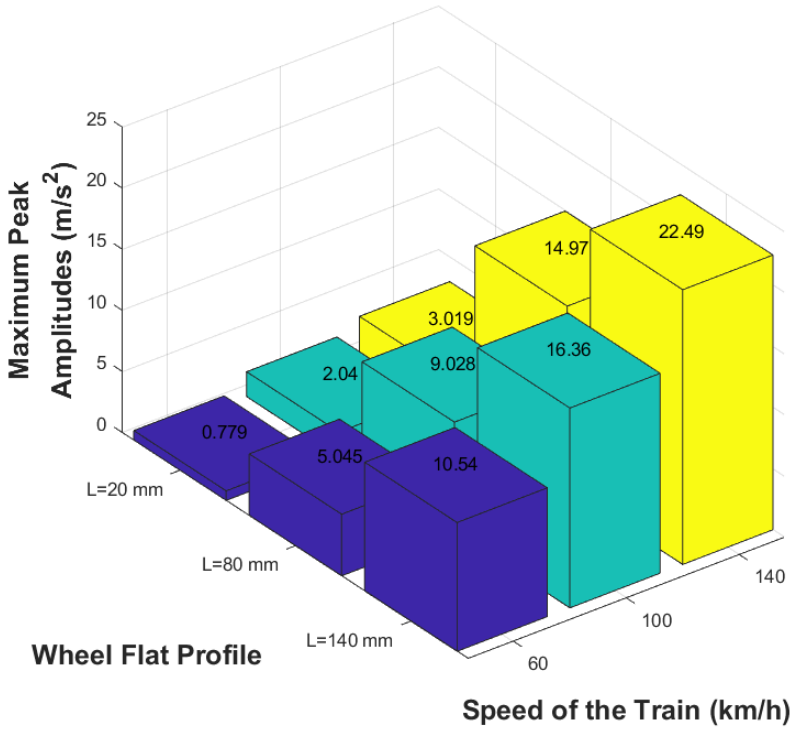

Figure 5-9 - Relation between train speed, *V*, wheel flat profile and maximum peak amplitude obtained from the Accelerometers (layout scheme 2) responses, using class 7 track irregularity profile

From the results visible in Figure 5-9 and as observed in subsection 5.2.1, higher train speeds and greater wheel flat lengths and depths generate higher peak amplitude responses. Even the "best case scenario" (*wf1* wheel profile with train speed *V*=60 km/h) generates much higher responses in the Accelerometers that the values obtained for healthy wheels. Therefore, the algorithm is capable to assess the train wheel condition and distinguish a defective wheel from a healthy one.

5.2.3. Wheel Flat Detection by the Response Obtained from the Strain Gauges

The following figures present the envelope spectrum of the signal to detect a defective wheel corresponding to the 10 virtual strain gauges evaluated on the rail (positions 1 to 10 shown in Figure 5-1, corresponding to layout scheme 1).

Influence of the Train Speed and the Track Irregularity Profiles

In order to evaluate the effects of train speed and track unevenness profile in the wheel flat detection by the signals evaluated from SGs, the wheel flat profile is considered as *wf1* profile. The envelope spectrum approach is utilized to verify the sensitivity of layout scheme 1, considering the unevenness profiles 3 to 8 depicted in Figure 5-10. The train speed considered as 60 km/h. Figure 5-11 presents the results for the same type of analyses regarding a train speed V=100 km/h and track irregularity profiles from classes 4 to 8, as mentioned in section 5.2. Finally, analyses performed for train speed V=140 km/h is depicted in Figure 5-12, analysing only classes 6, 7 and 8 of track irregularity profile according to what is stated at the beginning of section 5.2. All the analyses were also compared with "control case" with the corresponding train speed for each scenario group, a theoretical "perfect track" profile (class 8) and a healthy wheel.

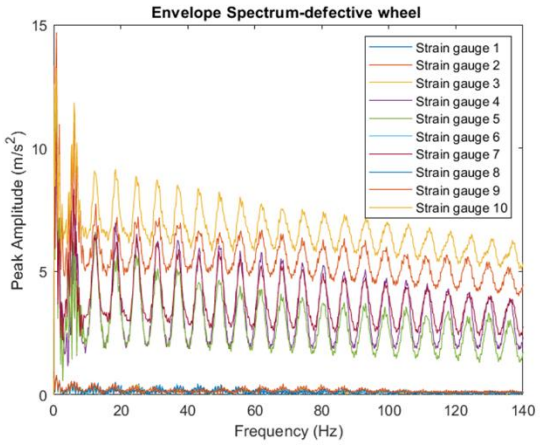

(**a**)

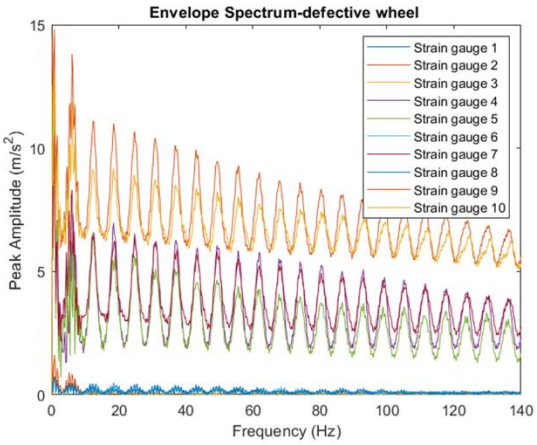

(**b**)

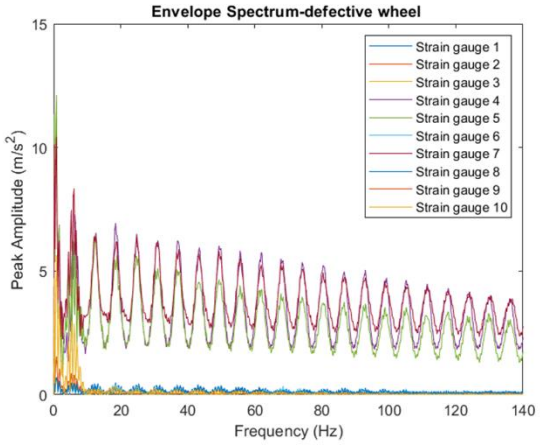

(**c**)

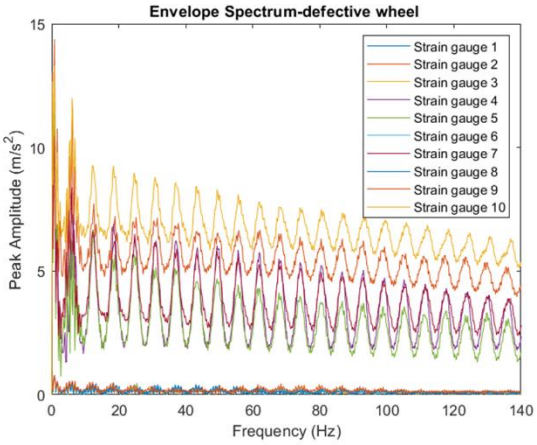

(**d**)

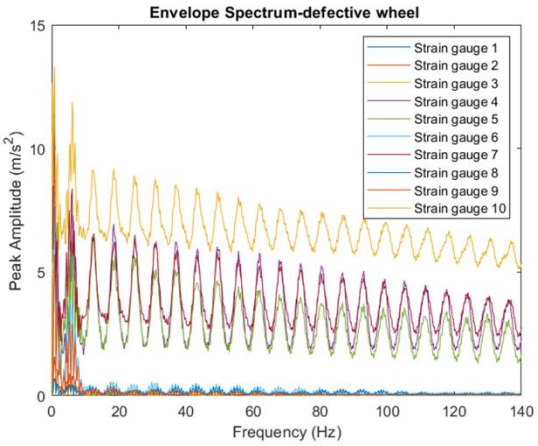

(**e**)

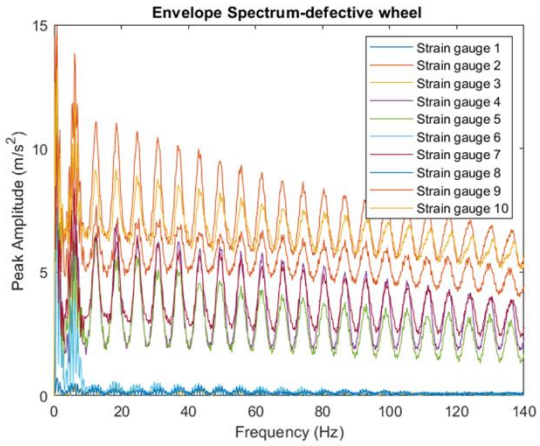

(**f**)

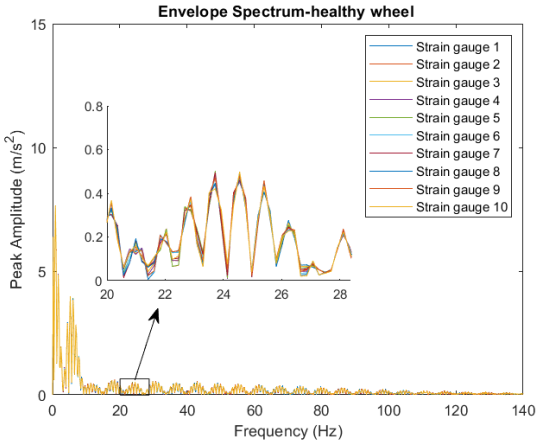

(**g**)

Figure 5-10 - Envelope spectrum analyses for the 10 SGs (layout scheme 1) for the *Alfa Pendular*, considering train speed ***V*=60 km/h** and *wf1* wheel flat profile: (**a**) class 3 track irregularity profile; (**b**) class 4 track irregularity profile; (**c**) class 5 track irregularity profile; (**d**) class 6 track irregularity profile; (**e**) class 7 track irregularity profile; (**f**) class 8 track irregularity profile; (**g**) control analyses with: train speed ***V*=60 km/h**, class 8 irregularity profile, and healthy wheel

The first set of results, shown in Figure 5-10 , come from analysing the *Alfa Pendular* vehicle passing at a speed *V*=60 km/h with a *wf2*-type wheel flat. By evaluating the results, it is possible to obverse a lag between the responses analysed at the several SGs where a defective wheel is presented (Figure 5-10(**a**)-(**f**)). Meanwhile, by looking at the control analysis (Figure 5-10(**g**)), the response in terms of envelope spectrum in all SGs are very similar (no lag), showing there are no flats in the wheels.

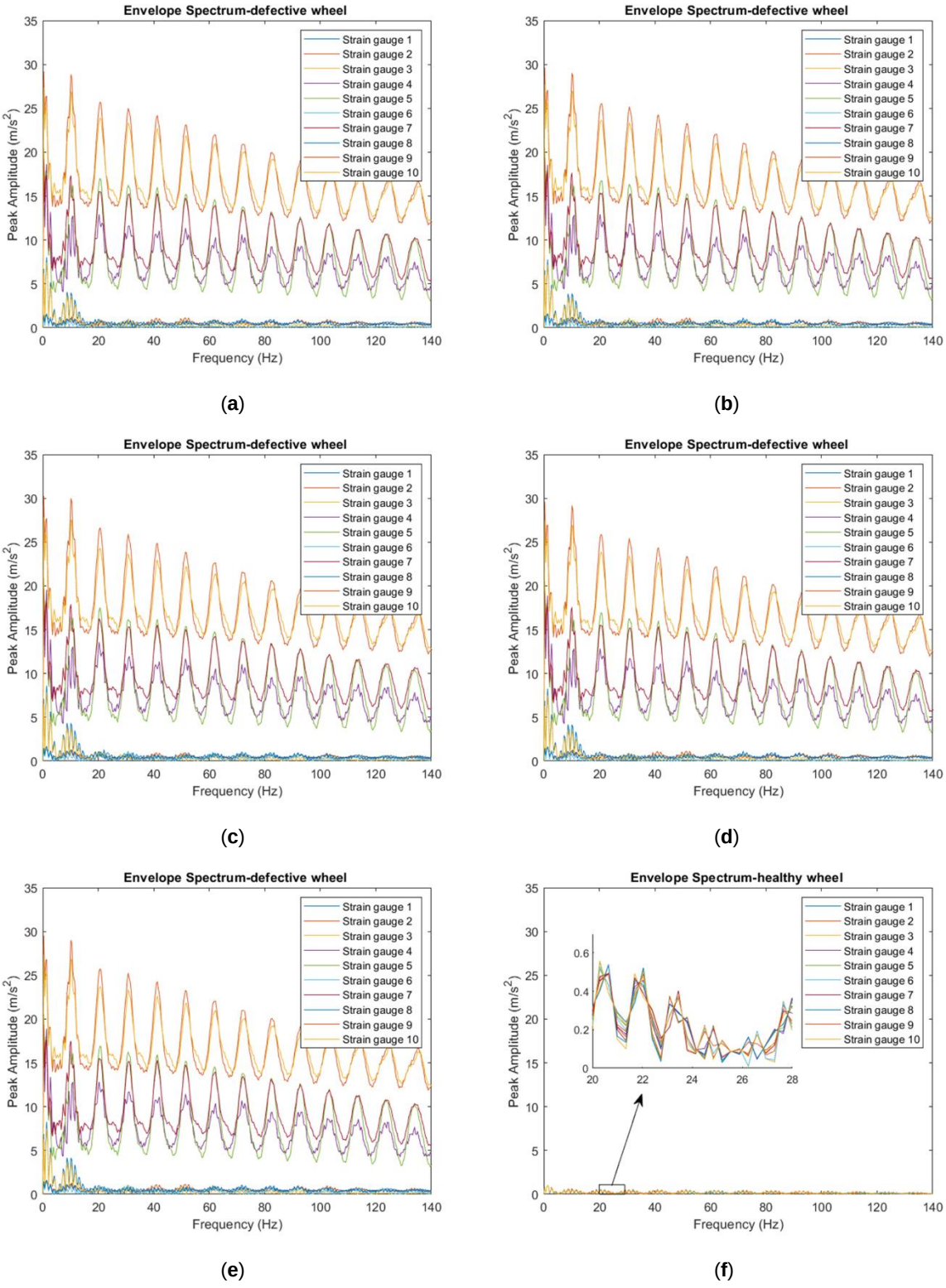

Figure 5-11 - Envelope spectrum analyses for the 10 SGs (layout scheme 1) for the *Alfa Pendular*, considering train speed ***V*=100 km/h** and *wf1* wheel flat profile: (**a**) class 4 track irregularity profile; (**b**) class 5 track irregularity profile; (**c**) class 6 track irregularity profile; (**d**) class 7 track irregularity profile; (**e**) class 8 track irregularity profile; (**f**) control analyses with: train speed ***V*=100 km/h**, class 8 irregularity profile, and healthy wheel

Figure 5-11 shows the results of envelope spectrum analyses for a train speed *V*=100 km/h, maintaining the *wf2*-type wheel flat evaluated for 10 SGs (layout scheme 1). One clear difference is the massive increase in peak amplitudes compared to the previous scenarios. It can thus be assumed that higher train speeds lead to greater impact forces from the wheel flat.

Another relevant information is the fact that the lag between responses is higher than the ones observed for *V*=60 km/h. Higher speeds lead to higher impact forces from the wheel flat, leading to this increase in lag response.

One of the interesting aspects observed in the analysis is the peak amplitude differences assessed by some SGs in Figure 5-11(**a**)-(**f**) that correspond to track irregularity classes 4-8. The reason is because these sensors are the nearest to the flat impact location with the rail.

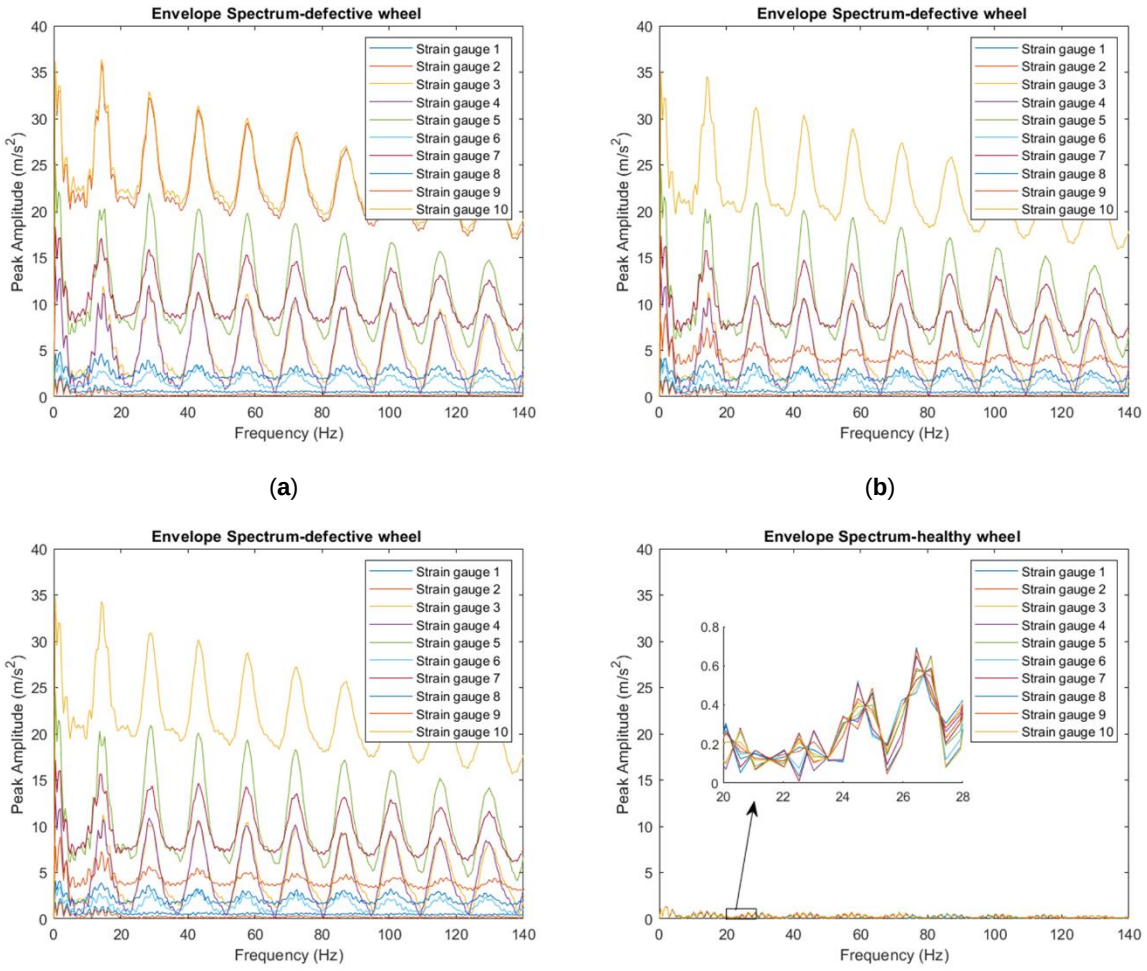

(**a**) (**b**)

(**c**) (**d**)

Figure 5-12 - Envelope spectrum analyses for the 10 SGs (layout scheme 1) for the *Alfa Pendular*, considering train speed *V*=**140 km/h** and *wf1* wheel flat profile: (**a**) class 6 track irregularity profile; (**b**) class 7 track irregularity profile; (**c**) class 8 track irregularity profile; (**d**) control analyses with: train speed ***V*=140 km/h**, class 8 irregularity profile, and healthy wheel

Figure 5-12 illustrates the results for a train speed V=140 km/h, keeping the *wf1* wheel flat profile. Peak amplitudes are again higher compared to the previous two scenario groups.

Influence of the Wheel Flat Profiles

In order to evaluate the effects of different wheel flats profiles, Figure 5-13 illustrates an analysis where all wheel flat profile variables are constant, with train speed, V=140 km/h, and class 7 (a real profile from the Portuguese Northern Line). For comparison, two control analysis are also presented, maintaining the same train speed: one for class 7 track irregularity profile and another for class 8. Both control analyses contain no defective wheels.

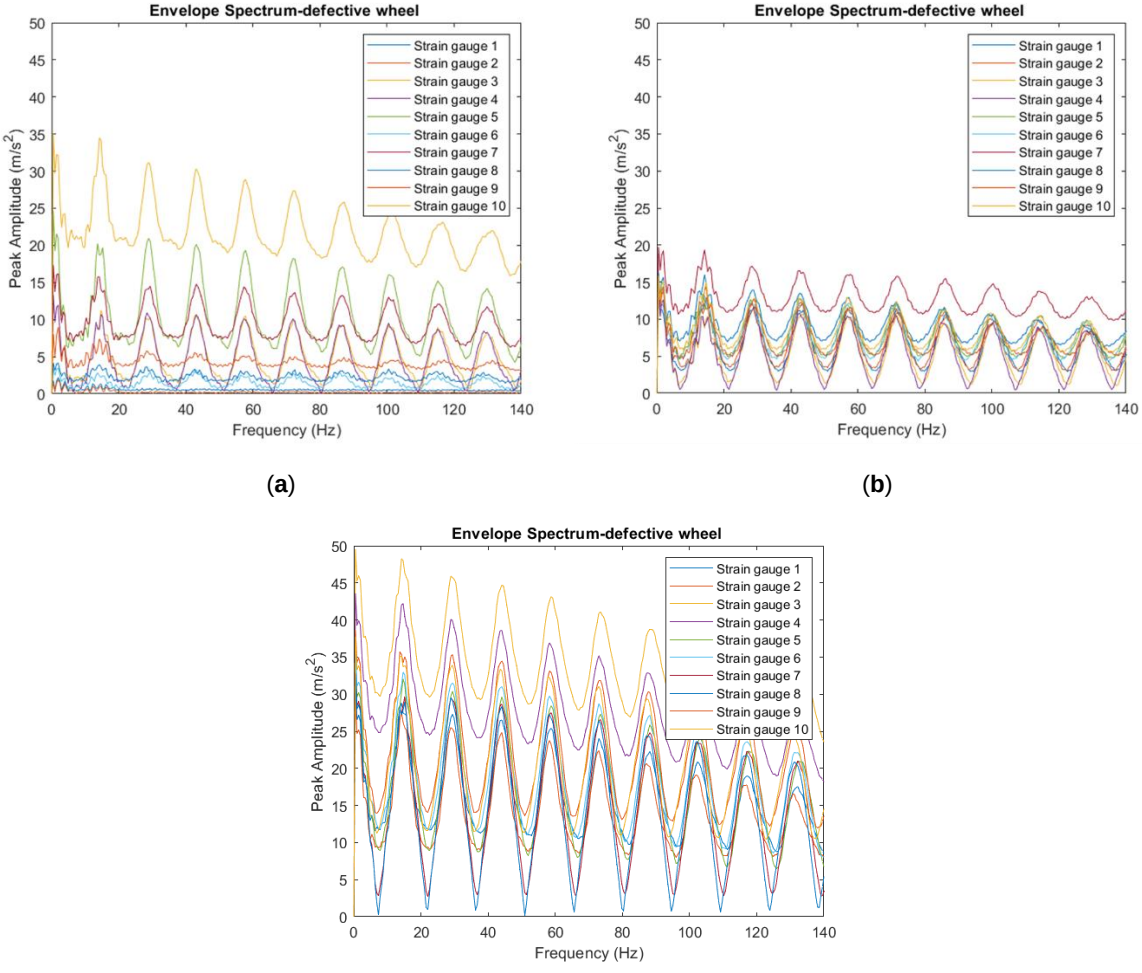

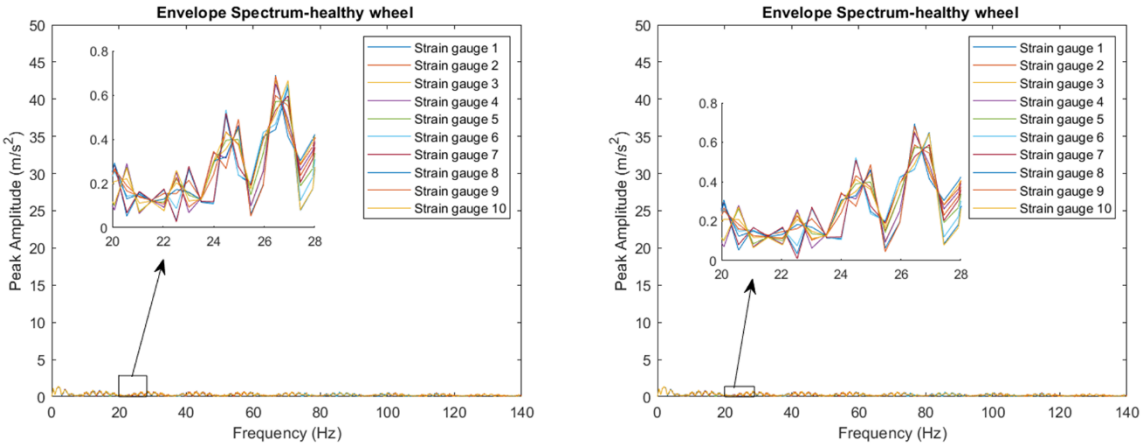

(**d**) (**e**)

Figure 5-13 - Envelope spectrum analyses for the 10 SGs (layout scheme 1) for the *Alfa Pendular*, considering train speed *V*=140 km/h and class 7 track irregularity profile: (**a**) ***wf1*** wheel flat profile; (**b**) ***wf2*** wheel flat profile; (**c**) ***wf3*** wheel flat profile; (**d**) control analyses with: train speed *V*=140 km/h, class 7 irregularity profile, and **healthy wheel**; (**e**) control analyses with: train speed *V*=140 km/h, class 8 irregularity profile, and **healthy wheel**

Comparing the five case scenarios illustrated above, an unexpected result is obtained from the *wf1* profile shown in Figure 5-13(**a**). It would be expected that greater wheel flats would originate higher peak amplitude responses from the SGs. While this is indeed verified when comparing *wf2* wheel flat profile (Figure 5-13(**b**)) and *wf3* wheel flat profile (Figure 5-13(**c**)), *wf1* flat profile shows peak amplitude responses in SGs 5 and 10 higher than what is seen in the same SGs results obtained when analysing *wf2* flat profile. One explanation for this could be that the flat impact on the rail happens directly above the SG sensors mentioned above. Looking at the other SGs in Figure 5-13(**a**), the peak amplitude values are lower than the results obtained from analysing *wf2*, observed in Figure 5-13(**b**).

However, when analysing the flat impact area corresponding to *wf1*, as can be seen in Figure 5-3, the closest sensor to the flat impact was SG 4 and not SG5, and SG 10 was nowhere near a flat impact area. Further analysis of *wf1* profile demonstrate that SG 10 (positioned at *X*=53.25 m) was located 0.75 m before the next flat impact, a significant distance outside both the sensor location and the analysed track section, as demonstrated in Figure 5-14.

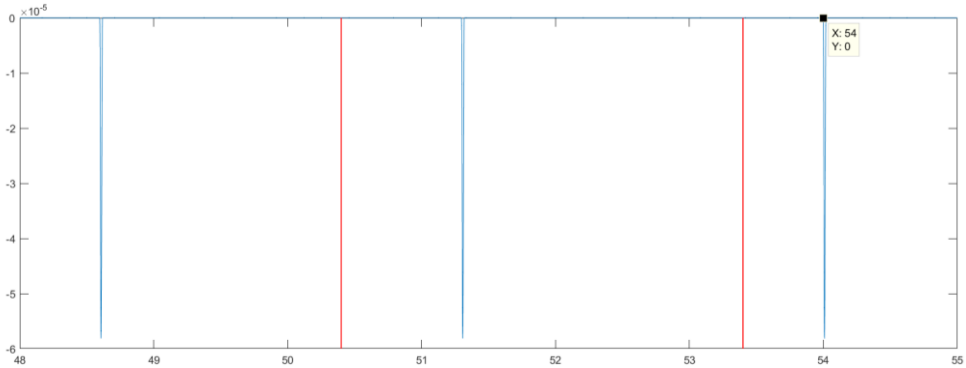

Figure 5-14 - *Wf1* profile showing the location of the flat impacts (blue line). The red lines indicate the length of the track section in study where the sensors were installed

Another aspect observed is the tendency of lag increase between SGs signal responses when wheel flat length increases, similar to what was observed with train speed increase. This is expected, as increasing flat length and depth leads to larger impact areas and thus, higher responses from the SGs.

By comparing the results from both accelerometers and SGs, it is evident that accelerometers have better results than SGs. This makes wheel flat detection analysis using accelerometers a good alternative instead of using SGs. Moreover, using strain gauges for long-term monitoring of wheel defect is not suitable because of their vulnerability to water and electromagnetic interferences. To compare the track response of strain gauges and accelerometers, both were placed in the same location, further concluding that strain gauges are not the best sensors to be used for wheel flat detection.

5.3. WHEEL POLYGONIZATION

The variables studied for wheel polygonization detection were: i.) speed of the train and ii.) OOR harmonic order. For these analyses, the Portuguese Northern Line track profile (class 7) was considered to simulate the effects of wheel polygonization on a real track profile. The train speeds, *V*, analysed were 60 km/h, 80km/h, 100 km/h, and 140 km/h.

A polygonised profile with wavelengths between 0.135 and 2.70 meters (2.70 meters being the circumference of the *Alfa Pendular* wheel) was considered for the simulation technique. To generate three polygonised wheel profiles, three different OOR harmonic orders were considered for the analyses:

- for the first polygonised wheel profile, nominated as *wp5*, the profile of the wheel is generated considering five harmonic orders. It was selected since wheels with harmonic orders of five have been identified in operational services, such as analysed in the work of Tao et al. (2019);
- for the second polygonised wheel profile, nominated as *wp12*, the profile of the wheel is generated taking into account 12 periodic harmonic orders. It was chosen as an intermediate value between the other two selected harmonic orders;
- for the third polygonised wheel profile, nominated as *wp20*, the profile of the wheel is generated considering 20 harmonic orders. It was chosen due to the fact that it is the highest harmonic order possible for this wheel circumference, as noted from Equation (12).

5.3.1. RESPONSE OBTAINED BY ACCELEROMETERS

The following figures present the envelope spectrum of the signal for a healthy and a defective wheel corresponding to 10 acceleration responses evaluated on the rail (positions 1 to 10 shown in Figure 5-1, corresponding to layout scheme 2), due to the passage of the *Alfa Pendular* vehicle.

Influence of the Train Speed

Figure 5-15 illustrates the envelope spectrum analyses obtained from the 10 accelerometers located between the sleepers from analysing the *Alfa Pendular* vehicle running in the Portuguese Northern Line track (class 7) with a polygonised wheel profile of *wp12*, running at speeds *V*=60 km/h (Figure 5-15(**a**)), *V*=80 km/h (Figure 5-15(**b**)), *V*=100 km/h (Figure 5-15(**c**)), and *V*=140 km/h (Figure 5-15(**d**)). Figure 5-15(**e**) presents the "control case", with a train speed *V*=100 km/h, class 7 track irregularity profile and healthy wheel.

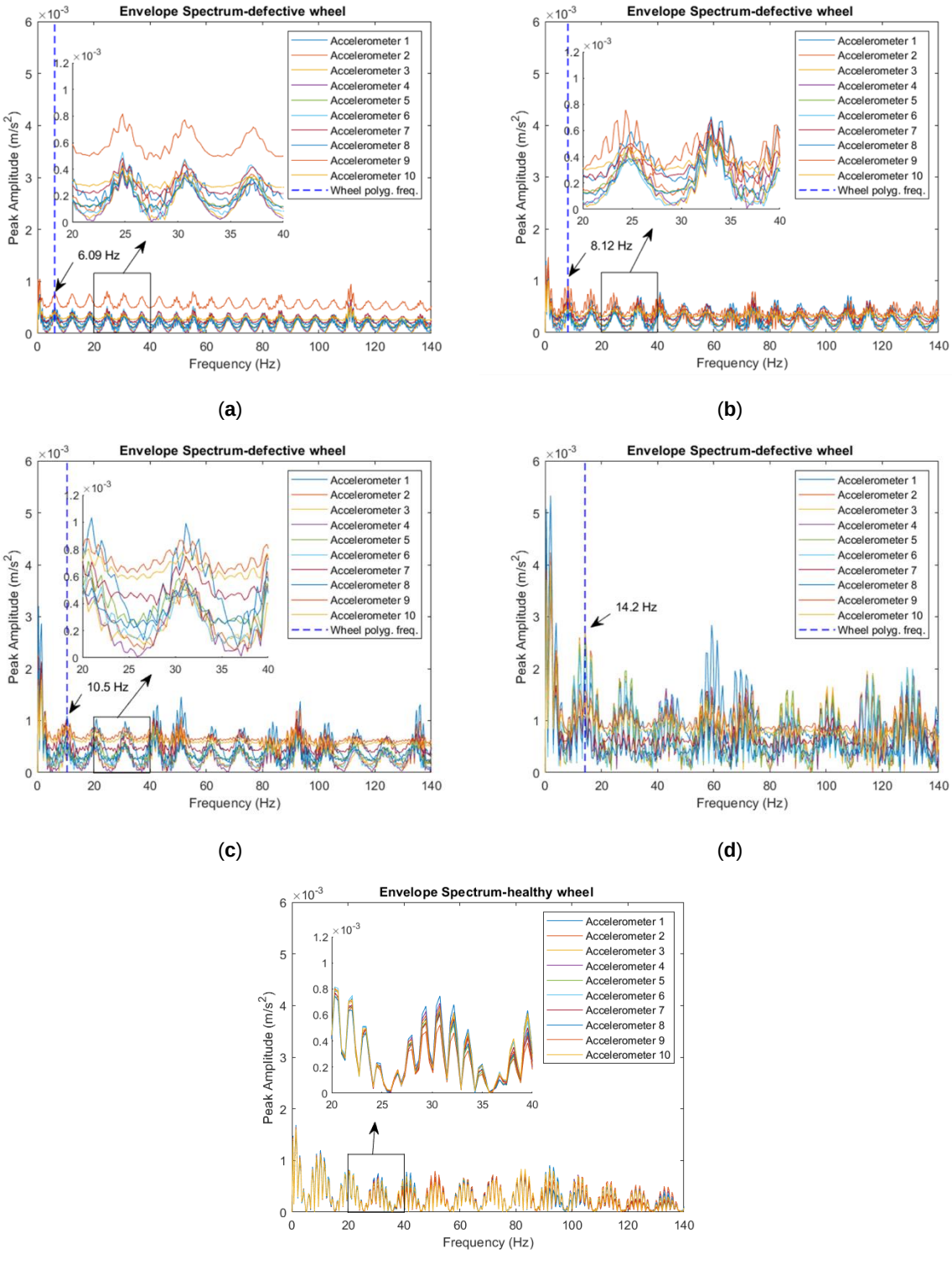

Figure 5-15 - Envelope spectrum analyses for the 10 accelerometers (layout scheme 2) for the *Alfa Pendular*, considering class 7 track irregularity profile and polygonised wheel with *wp12*: (**a**) train speed ***V*=60 km/h**; (**b**) train speed ***V*=80 km/h**; (**c**) train speed ***V*=100 km/h**; (**d**) train speed ***V*=140 km/h**; (**e**) control analyses with: train speed ***V*=100 km/h**, class 7 track irregularity profile, and healthy wheel

The peak amplitude responses evaluated by the accelerometers, as seen in Figure 5-15, enhance when the speed of the vehicle increases. Figure 5-15(**a**),(**b**),(**c**) show peak amplitude responses similar to those obtained from the control analysis (Figure 5-15(**e**)), with only the results for a train speed *V*=140 km/h (Figure 5-15(**d**)) showing peak amplitudes is higher than the control analysis. Nonetheless, all OOR case scenarios clearly show a lag in the responses, in contrast to the control analysis. When comparing the increase in peak amplitude responses with results obtained from the wheel flat detection analyses, the results from a polygonised wheel are significantly lower than those observed in wheel flats.

As with wheel flats, the polygonization frequencies obtained for each speed, shown in the figure above, were similar to the theoretical values obtained from Equation (11), being the same values obtained from the wheel flat detection analyses (the theoretical value for the speed *V*=80 km/h is 8.23 Hz, close to the 8.12 Hz value obtained during the analysis).

Influence of the Harmonic Orders

Figure 5-16 illustrates the envelope spectrum analyses obtained from 10 accelerometers from analysing the *Alfa Pendular* vehicle running in the Portuguese Northern Line track sample (class 7) with a speed of 100 km/h, considering *wp5* polygonised wheel profile (Figure 5-16(**a**)), *wp12* polygonised wheel profile (Figure 5-16(**b**)), and *wp20* polygonised wheel profile (Figure 5-16(**c**)). Figure 5-16(**d**) presents the "control case", with a train speed *V*=100 km/h, class 7 track irregularity profile and healthy wheel.

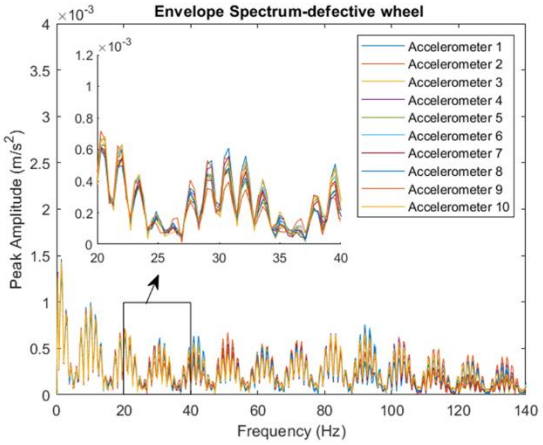

(**a**)

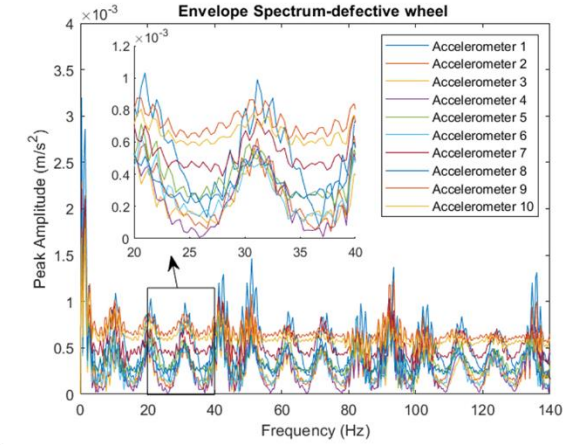

(**b**)

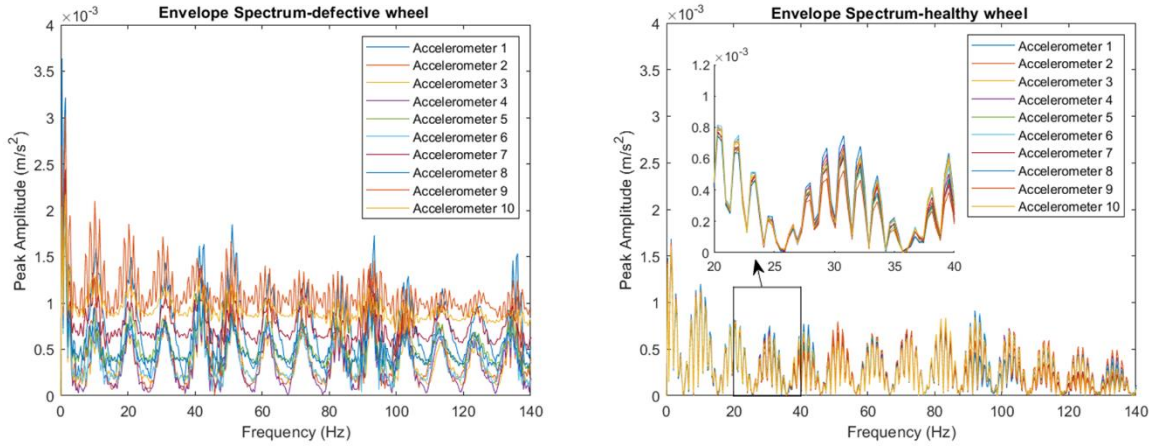

(**c**) (**d**)

Figure 5-16 - Envelope spectrum analyses for the 10 Accelerometers (layout scheme 2) for the *Alfa Pendular*, considering class 7 track irregularity profile and train speed *V*=100 km/h: (**a**) polygonised wheel profile ***wp5***; (**b**) polygonised wheel profile ***wp12***; (**c**) polygonised wheel profile ***wp20***; (**d**) control analyses with: train speed *V*=100 km/h, class 7 track irregularity profile, and **healthy wheel**

The envelope spectrum analyses shown in Figure 5-16 demonstrate that by increasing the number of harmonic order, the amplitude of envelope spectrum enhances as well, showing that although the defect is very small comparing to wheel flat, algorithm is still capable to detect a defective wheel. The results obtained for the polygonised wheel with a harmonic order of 5 (Figure 5-16(**a**)) are very similar to the responses received from a healthy wheel. For the cases depicted in Figure 5-16(**b**),(**c**) a lag in the responses from the Accelerometers is visible, showing that a defective wheel is present in the analyses. This does not seem to occur in Figure 5-16(**a**), corresponding to *wp5* profile, behaving similar to a healthy wheel.

As mentioned in the section 5.2 there are 2 indicators to defect a wheel flat. By applying the envelop spectrum analysis, it is possible to observe a lag between the responses evaluated at the several sensors in the defective wheel, showing that a flat has been detected. On the other hand, the responses in terms of the envelope spectrum in all sensors are very similar (no lag), indicating that there are no flats in the wheels. Moreover, the amplitude variation of the envelope spectral signal can also be seen as an additional indicator to evaluate whether the wheel is healthy or not. As shown in this figure, the amplitude variation of the envelope spectral signal of a defective wheel is higher than a healthy one.

To detect a polygonised wheel there is only 1 indicator to distinguish a healthy wheel from a defective one. It is possible to observe that, in the presence of a polygonised wheel, the responses of each accelerometer in terms of envelope spectrum present significant lag, while for the scenarios with a healthy wheel or a polygonised wheel with small number of harmonic orders, this lag is practically insignificant.

5.3.2. Response Obtained by the Strain Gauges

The following figures present envelope spectrum of the signal for defective wheels and the healthy ones corresponding to the ten shear responses evaluated on the rail (positions 1 to 10 shown in Figure 5-1, corresponding to layout scheme 1), due to the passage of the *Alfa Pendular* vehicle.

Influence of the Train Speed

Figure 5-17 presented Envelope spectrum analyses for the 10 SGs (layout scheme 1) for the *Alfa Pendular* vehicle considering class 7 track irregularity profile and polygonised wheel profile *wp12* for the speeds *V*=60 km/h (Figure 5-17(**a**)), *V*=80 km/h (Figure 5-17(**b**)), *V*=100 km/h (Figure 5-17(**c**)), and *V*=140 km/h (Figure 5-17(**d**)). Figure 5-17(**e**) presents the "control case", with a train speed *V*=100 km/h, class 7 track irregularity profile and healthy wheel.

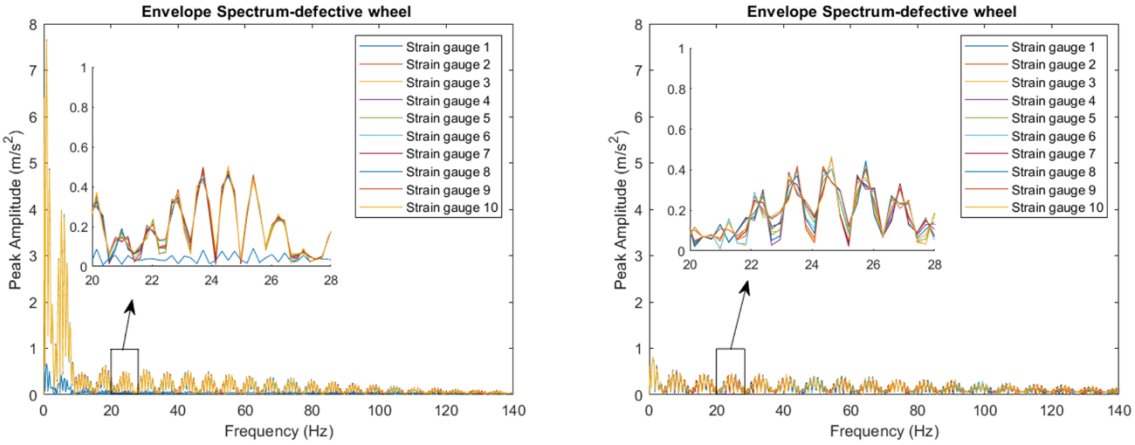

(**a**) (**b**)

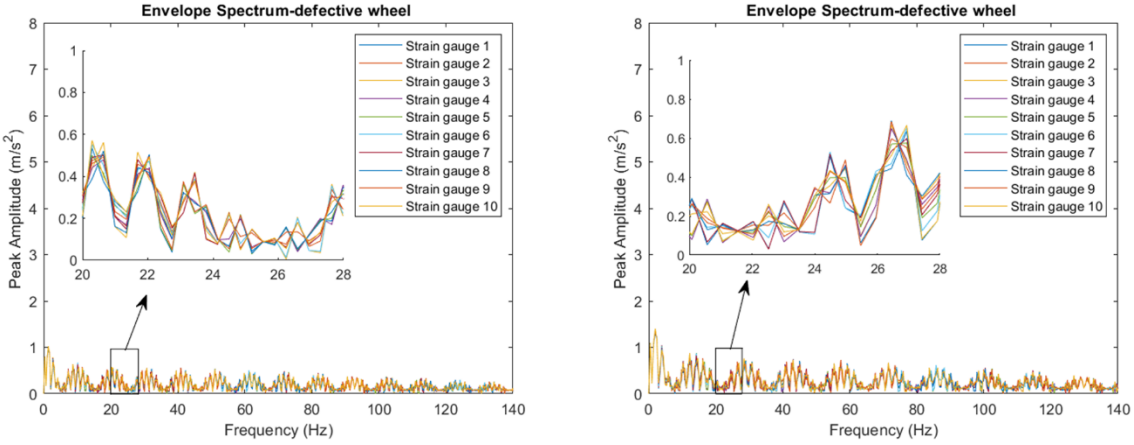

(**c**) (**d**)

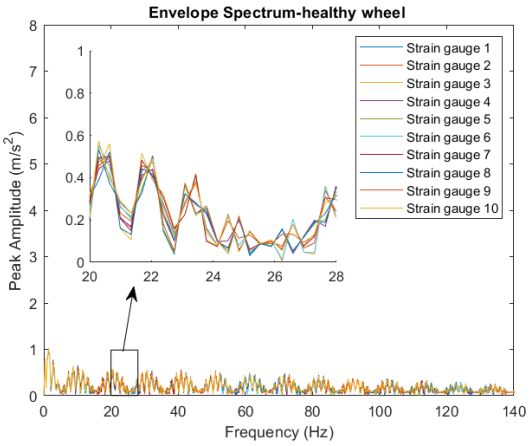

(**e**)

Figure 5-17 - Envelope spectrum analyses for the 10 SGs (layout scheme 1) for the *Alfa Pendular*, considering class 7 track irregularity profile and polygonised wheel profile *wp12*: (**a**) train speed ***V*=60 km/h**; (**b**) train speed ***V*=80 km/h**; (**c**) train speed ***V*=100 km/h**; (**d**) train speed ***V*=140 km/h**; (**e**) control analyses with: train speed ***V*=100 km/h**, class 7 track irregularity profile, and healthy wheel

Differently than the results shown in Figure 5-10, Figure 5-11, and Figure 5-12, regarding the detection of wheel flats, the peak amplitudes demonstrated in the majority of Figure 5-17 cases do not vary significantly with the increase in train speed. The analyses cases Figure 5-17(**b**),(**c**),(**d**) also present only marginally higher values compared to the control case (Figure 5-17(**e**)). For the scenario with a train speed of 60 km/h (Figure 5-17(**a**)), there is an increase in peak amplitude value for the first defect frequency compared to the other cases. For the remaining frequencies, the response values become similar to the other scenarios.

Comparing these results with the results obtained from the accelerometers presented in Figure 5-11, it is possible to infer that the accelerometers can detect the damaged wheel, while it is almost impossible to detect the polygonised wheel using a strain gauge response as an input for the algorithm.

Influence of the OOR Harmonic Orders

Figure 5-18 illustrates the envelope spectrum analyses for the 10 SGs (layout scheme 1) for the passage of Alfa Pendular vehicle, considering class 7 track irregularity profile. The train speed is considers as V=100 km/h having *wp5* wheel profile (Figure 5-18(**a**)), *wp12* wheel profile (Figure 5-18(**b**)), and *wp20* wheel profile (Figure 5-18(**c**)). Figure 5-18(**d**) presents the "control case", with a train speed *V*=100 km/h, class 7 track irregularity profile and healthy wheel.

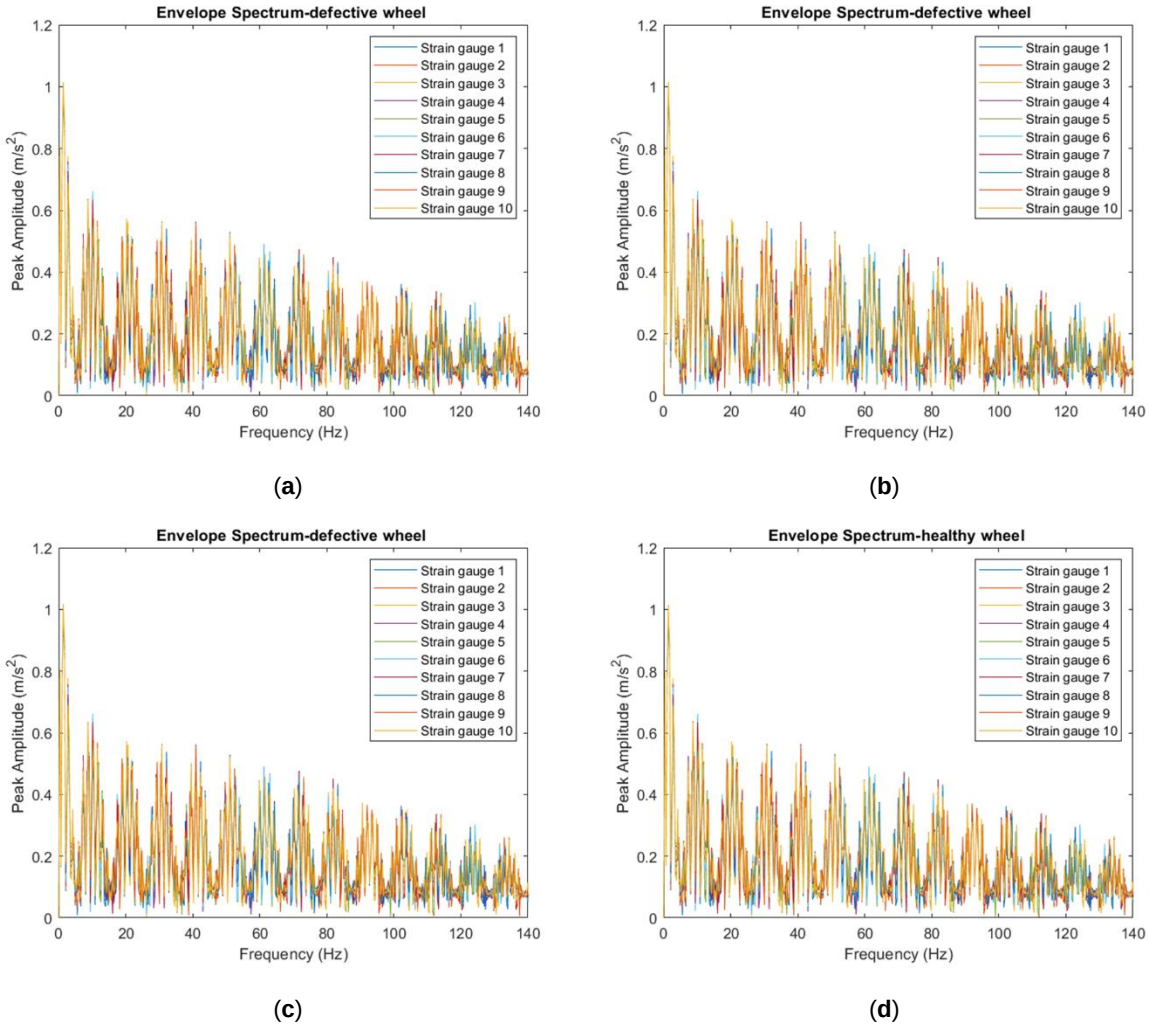

Figure 5-18 - Envelope spectrum analyses for the 10 SGs (layout scheme 1) for the *Alfa Pendular*, considering class 7 track irregularity profile and train speed *V*=100 km/h: (**a**) polygonised wheel profile ***wp5***; (**b**) polygonised wheel profile ***wp12***; (**c**) polygonised wheel profile ***wp20***; (**d**) control analyses with: train speed *V*=100 km/h, class 7 track irregularity profile, and **healthy wheel**

It is noticeable that all of the above results do not show a significant difference with the control case. Similar to what was observed when analysing the influence of train speed in Figure 5-17, it appears that harmonic order of polygonization does not affect the detection of defective wheels when utilizing SGs on the tracks, contrary to what is observed when analysing acceleration responses with accelerometers.

5.3.3. Relation Between Polygonization Harmonic Orders, Train Speed and Maximum Peak Acceleration Amplitude

To summarize the results from the analyses presented above, Figure 5-19 presents the relation between train speed, *V*, wheel OOR harmonic order, and maximum peak amplitude response obtained from across all the accelerometers belonging to layout scheme 2. “Class 7” was considered for the unevenness profile of the rail.

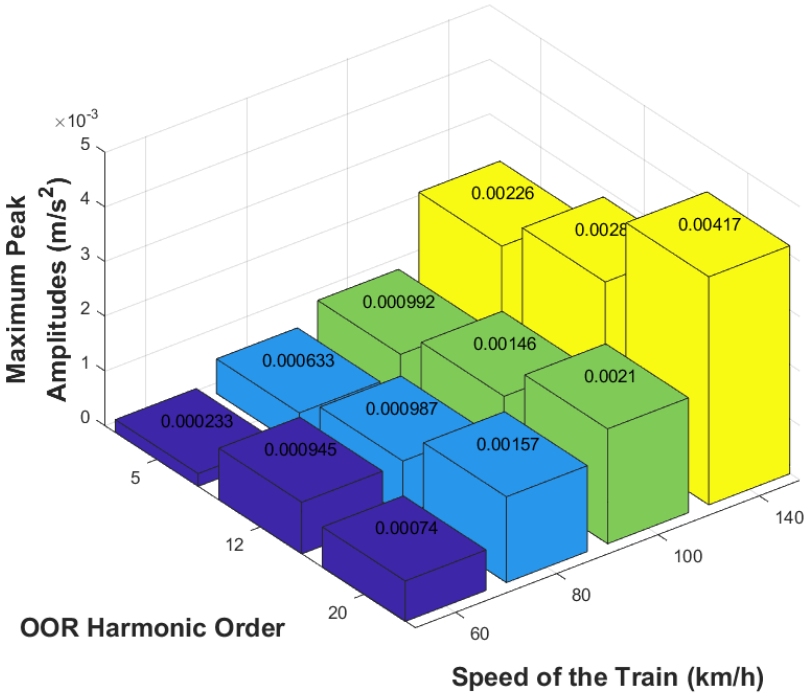

Figure 5-19 - Relation between train speed, *V*, OOR harmonic order and maximum peak amplitude obtained from the accelerometers (layout scheme 2) responses, using class 7 track irregularity profile

Figure 5-19 shows that higher train speeds and higher OOR harmonic orders of a polygonised wheel tend to generate higher peak amplitude responses. The challenge the envelope spectrum analyses for the polygonised wheel with lower harmonic orders (*wp5*) and lower speeds are very similar to the healthy wheel.

For the other cases, the algorithm was capable to detect a defective wheel, however more detailed analyses need to be carried out in order to detect a polygonised wheel with less harmonic orders and lower speeds.

5.4. Influence of One Defective Wheel in the Track

As mentioned in section 5.1 only the right wheel of the first wheelset has been modelled as a defective wheel. Although only the first wheel on the right side is considered as a defective wheel, the algorithm was able to distinguish a defective wheel from a healthy one by considering the input signals from the left side (which does not have defect). The following figure shows the comparison of envelope spectrum analyses for the 10 Accelerometers (Figure 5-20) for the *Alfa Pendular* vehicle, considering "class 7" track irregularity profile. Trian speed was set at *V*=140 km/h. *wf2* wheel flat profile was taken into account for the first wheel on the right side.

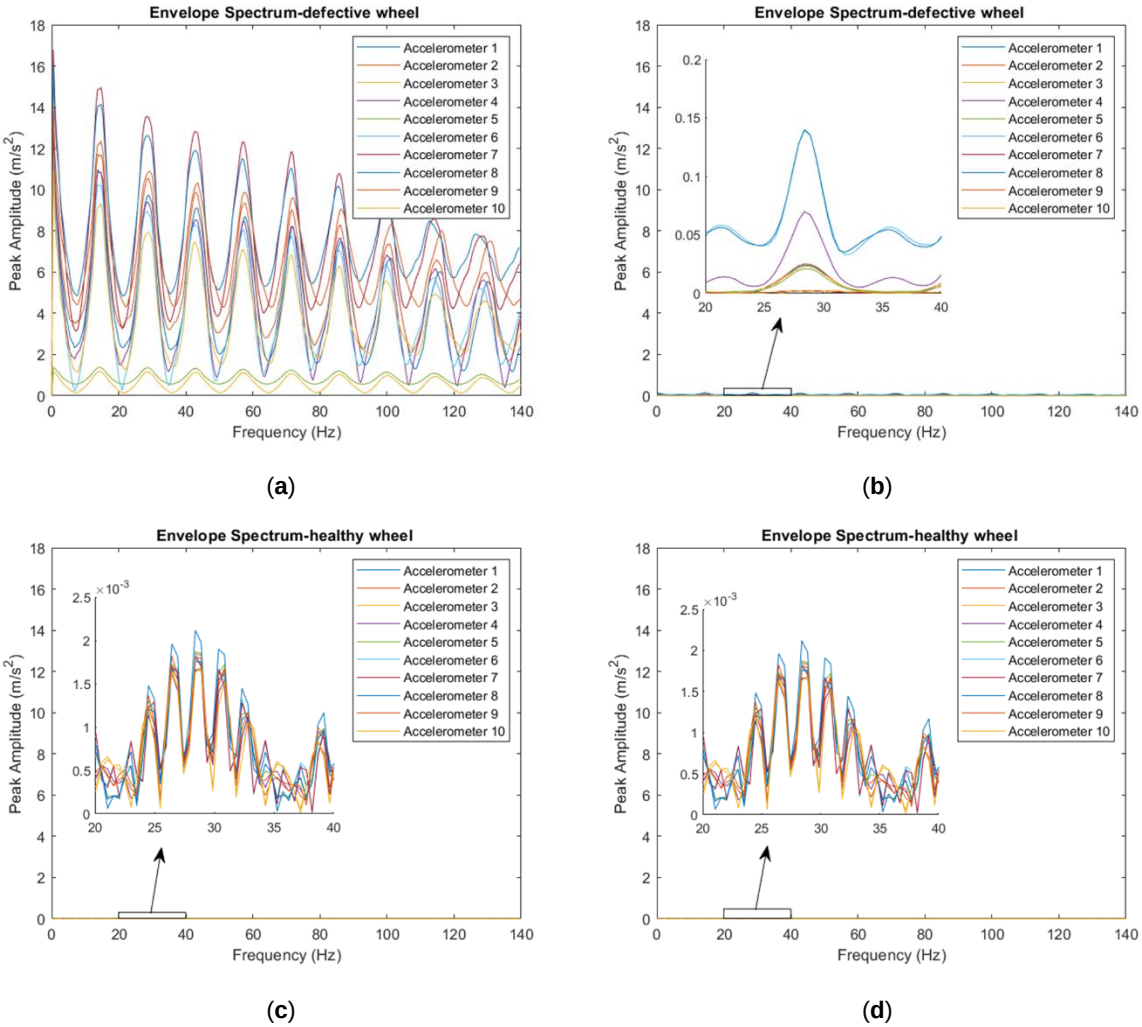

Figure 5-20 - Comparison of envelope spectrum analyses for the 10 Accelerometers (layout scheme 2) for the *Alfa Pendular*, considering "class 7" track irregularity profile and train speed *V*=140 km/h: (**a**) *wf2* wheel flat profile measured on the **right side** of the track; (**b**) *wf2* wheel flat profile measured on the **left side** of the track; (**c**) control analyses with a healthy wheel, measured on the **right side** of the track; (**d**) control analyses with a healthy wheel, measured on the **left side** of the track

As can be seen in Figure 5-20, the effects of the defective wheel on the right can still be noticed on the left side of the track, because the right and left wheel are connected to one axle. Looking at the results, it is clear that the values registered on the left rail were less predominant, being two orders of magnitude lower than on the side of the defective wheel (Figure 5-20(**a**),(**b**)). Nonetheless, they were still much higher than the responses obtained with a healthy wheel scenario (Figure 5-20(**c**),(**d**)). It can thus be concluded that a defect located on only one of the axle's wheels can have implications on both rails.

6
CONCLUSIONS

This Chapter presents: i.) a summary of the conclusions from the simulations performed and ii.) future developments to be made in the field of railway vehicle OOR detection based on the results from the analyses.

6.1. GENERAL CONCLUSIONS

This dissertation aimed to validate the aforementioned algorithm in order to simulate the detection of railway train wheel OOR. For this a series of scenario combinations where considered, utilizing healthy wheels, three-wheel flat profiles, three polygonised wheel profiles, three to four train speeds, and track irregularity profiles modelled according to the FRA regulation (classes 3 to 6), a track sample from the Portuguese Network Northern Line ("class 7"), and a theoretical "perfect track" ("class 8"). The algorithm simulated a multisensor array for the detection of wheel defects, with the use of both strain gauge and accelerometers sensors. The implemented analyses have been shown that the algorithm is capable of detecting wheel flats and polygonised wheels in numerous case scenarios.

The effects of wheel flat are more noticeable in the algorithm simulations compared to the effects of periodically polygonised wheels. This may be caused by the sudden shift from the regular wheel profile into the hit of the flat, something that does not occur in the case of polygonised wheel. In fact, some results from polygonised wheel (*wp5* and speed V=60 km/h) analyses show sensor responses close to those obtained when analysing healthy wheels, especially when utilising strain gauge sensors, as also observed in Gonçalves et al. (2023). This can create a false assumption that the train wheel is not damaged (because there is no lag between signals), which can lead to serious problems in a real case scenario analysis.

The use of envelope spectrum analysis has proven to be beneficial in the analyses, demonstrating that both strain gauge sensors and accelerometers are capable of detecting these two types of wheel defects. Moreover, it allows for better analysis in a real case scenario, due to the drawbacks of strain gauge sensors mentioned above and under non-ideal weather conditions, as it was already demonstrated in Mosleh et al. (2021). Comparing the results of the two different layouts for the accelerometers locations were also positive, proving that, as it was also concluded by Mosleh et al. (2021), for the same track section, accelerometers located on top of the sleepers, and therefore less sensors overall, are capable of detecting a damaged wheel. Therefore, it can be concluded that the algorithm is able to detect a defective wheel regardless of the position of the sensors.

Comparing the peak responses for each wheel defect profile and vehicle speed, it was observed that worse wheels and higher speeds lead to higher peak responses. This shows that the higher train speeds result in more impact on the railway tracks, an effect worsened the more damaged the wheel is.

Regarding the track irregularity, it does not seem to have noticeable influence on the detection of defective wheels.

6.2. FUTURE DEVELOPMENTS

The algorithm is meant to simulate sensor responses caused by wheel defects on a moving train in a physical track section. As it was mentioned above, the algorithm has shown to be capable of detecting wheels that suffer from flats or polygonization. To validate the accuracy of the results from the performed analyses, experimental analysis with sensors installed on a physical track section needs to be conducted.

To further validate the algorithm, research into other scenarios, the usage of other types of passenger trains or freight trains and analysing the effect of different levels of occupation of the trains must be realised. Another field of study for the algorithm is its usefulness in detecting other types of wheel defects, such as non-periodic polygonization of the wheels or corrugation. The case for non-periodic polygonization could be deemed challenging, as modelling a wheel with this type of defect using software is extremely complex.

BIBLIOGRAPHICAL REFERENCES

Ahlström, J., & Karlsson, B. (1999). Microstructural evaluation and interpretation of the mechanically and thermally affected zone under railway wheel flats. *Wear*, *232*(1), 1–14. https://doi.org/10.1016/S0043-1648(99)00166-0

Alemi, A., Pang, Y., & Lodewijks, G. (2018). In-service detection of defective railway wheels with periodic out-of-roundness. *Proceedings of the 11th International Conference on Contact Mechanics and Wear of Rail/Wheel Systems, CM 2018*.

Alexandrou, G., Kouroussis, G., & Verlinden, O. (2016). A comprehensive prediction model for vehicle/track/soil dynamic response due to wheel flats. *Proceedings of the Institution of Mechanical Engineers, Part F: Journal of Rail and Rapid Transit*, *230*(4), 1088–1104. https://doi.org/10.1177/0954409715576015

Amini, A., Entezami, M., Huang, Z., Rowshandel, H., & Papaelias, M. (2016). Wayside detection of faults in railway axle bearings using time spectral kurtosis analysis on high-frequency acoustic emission signals. *Advances in Mechanical Engineering*, *8*(11). https://doi.org/10.1177/1687814016676000

Amini, A., Entezami, M., & Papaelias, M. (2016). Onboard detection of railway axle bearing defects using envelope analysis of high frequency acoustic emission signals. *Case Studies in Nondestructive Testing and Evaluation*, *6*, 8–16. https://doi.org/10.1016/J.CSNDT.2016.06.002

ANSYS®. (2018). *Academic Research Version 19.2* (19.2). ANSYS Inc.

Antoni, J. (2006). The spectral kurtosis: a useful tool for characterising non-stationary signals. *Mechanical Systems and Signal Processing*, *20*(2), 282–307. https://doi.org/10.1016/J.YMSSP.2004.09.001

Antoni, J. (2007). Fast computation of the kurtogram for the detection of transient faults. *Mechanical Systems and Signal Processing*, *21*(1), 108–124. https://doi.org/10.1016/J.YMSSP.2005.12.002

Auersch, L. (2008). Dynamic interaction of various beams with the underlying soil – finite and infinite, half-space and Winkler models. *European Journal of Mechanics - A/Solids*, *27*(5), 933–958. https://doi.org/10.1016/J.EUROMECHSOL.2008.02.001

Bogdevicius, M., Zygiene, R., Bureika, G., & Dailydka, S. (2016). An analytical mathematical method for calculation of the dynamic wheel–rail impact force caused by wheel flat. *Vehicle System Dynamics*, *54*(5), 689–705. https://doi.org/10.1080/00423114.2016.1153114

Bosso, N., Gugliotta, A., & Zampieri, N. (2018). Wheel flat detection algorithm for onboard diagnostic. *Measurement*, *123*, 193–202. https://doi.org/10.1016/J.MEASUREMENT.2018.03.072

Brandt, A. (2011). Noise and Vibration Analysis: Signal Analysis and Experimental Procedures. In *Noise and Vibration Analysis: Signal Analysis and Experimental Procedures*. https://doi.org/10.1002/9780470978160

Cavuto, A., Martarelli, M., Pandarese, G., Revel, G. M., & Tomasini, E. P. (2016). Train wheel diagnostics by laser ultrasonics. *Measurement*, *80*, 99–107. https://doi.org/10.1016/J.MEASUREMENT.2015.11.014

Colaço, A., Costa, P. A., & Connolly, D. P. (2016). The influence of train properties on railway ground vibrations. *Structure and Infrastructure Engineering*, *12*(5), 517–534. https://doi.org/10.1080/15732479.2015.1025291

Costa, P. M. B. (2011). *Vibrações do sistema via-maciço induzidas por tráfego ferroviário : modelação numérica e validação experimental* [PhD Thesis, Faculty of Engineering of the University of Porto]. http://hdl.handle.net/10216/61470

Entezami, M., Roberts, C., Weston, P., Stewart, E., Amini, A., & Papaelias, M. (2020). Perspectives on railway axle bearing condition monitoring. *Proceedings of the Institution of Mechanical Engineers, Part F: Journal of Rail and Rapid Transit*, *234*(1), 17–31. https://doi.org/10.1177/0954409719831822

Esveld, C. (1997). Track structures in an urban environment. *TU Delft, Symposium KU Leuven*. https://www.esveld.com/Download/TUD/urban.pdf

Esveld, C. (2001). *Modern Railway Track* (2nd ed.). MRT-Productions.

European Rail Research Institute. (1999a). *Improved Knowledge of Forces in CWR Track (Including Switches): Parametric Study and Sensivity Analysis of Cwerri* (ERRI D 202/RP 11).

European Rail Research Institute. (1999b). *Rail Bridges for Speeds > 200 km/h: Numerical Investigation of the Effect of Track Irregularities at Bridge Resonance* (ERRI D 214/RP 5).

European Standard. (2002). *Railway Applications Railway Applications—Track-Rail-Part1: Vignole Railway 46 kg/m and above* (peEN 13674–1, Final Draf).

Railway applications - Track - Rail - Part 1: Vignole railway rails 46 kg/m and above, Pub. L. No. EN 13674-1:2011+A1:2017 (2017).

Fang, L., Li, S., Dai, W., Zhang, Y., Xing, Z., & Han, Y. (2020). Method of Wheel Out-of-Roundness Detection Based on POVMD and Multinuclear LS-SVM. *Lecture Notes in Electrical Engineering*, *639*, 19–27. https://doi.org/10.1007/978-981-15-2866-8_3

Fortunato, E. M. C. (2005). *Renovação de plataformas ferroviárias: estudos relativos à capacidade de carga* [PhD Thesis, Faculty of Engineering of the University of Porto]. https://hdl.handle.net/10216/11441

Fries, R. H., & Coffey, B. M. (1990). A state-space approach to the synthesis of random vertical and crosslevel rail irregularities. *Journal of Dynamic Systems, Measurement and Control, Transactions of the ASME*, *112*(1), 83–87. https://doi.org/10.1115/1.2894143

Gao, R., He, Q., & Feng, Q. (2019). Railway wheel flat detection system based on a parallelogram mechanism. *Sensors*, *19*(16). https://doi.org/10.3390/s19163614

Gonçalves, V., Mosleh, A., Vale, C., & Montenegro, P. A. (2023). Wheel Out-of-Roundness Detection Using an Envelope Spectrum Analysis. *Sensors*, *23*(4). https://doi.org/10.3390/s23042138

Guo, Q., Chen, S., Xie, X., Ma, L., Hu, Q., Liu, H., Liu, Y., Zhao, J., & Li, X. (2019). An empirical study towards characterizing deep learning development and deployment across different frameworks and platforms. *Proceedings - 2019 34th IEEE/ACM International Conference on Automated Software Engineering, ASE 2019*, 810–822. https://doi.org/10.1109/ASE.2019.00080

Hamid, A., & Yang, T. L. (1982). Analytical description of track-geometry variations. In *Transportation Research Record* (Vol. 838, pp. 19–26). Transportation Research Board.

Hasan, T. (1983). Complex demodulation: Some theory and applications. In D. R. Brillinger & P. R. Krishnaiah (Eds.), *Time Series in the Frequency Domain. Handbook of Statistics* (Vol. 3, pp. 125–156). North-Holland Publishing Company. https://doi.org/10.1016/S0169-7161(83)03009-6

Hu, X. Y., He, Q. F., Wang, H. S., & Liu, J. Z. (2008). Vibration signal demodulation method based on STFT and its application in rolling bearing fault detections. *Zhendong Yu Chongji/Journal of Vibration and Shock*, *27*(2), 82–86.

Huang, H., Wang, H., Zhang, W., & Gu, W. (2021). A Fault Diagnosis Method for Out-of-Round Faults of Metro Vehicle Wheels with Strong Noise. *Shock and Vibration*, *2021*(Special Issue), 1–12. https://doi.org/10.1155/2021/9257622

International Union of Railways. (2001). *Track/Bridge Interaction—Recommendations for Calculation* (UIC 774-3-R).

Iwnicki, S. (2006). Handbook of railway vehicle dynamics. In *Handbook of Railway Vehicle Dynamics*. https://doi.org/10.1201/9781420004892

Jergéus, J., Odenmarck, C., Lundén, R., Sotkovszki, P., Karlsson, B., & Cullers, P. (1999). Full-scale railway wheel flat experiments. *Proceedings of the Institution of Mechanical Engineers, Part F: Journal of Rail and Rapid Transit*, *213*(1), 1–13. https://doi.org/10.1243/0954409991530985

Jiang, Y., Chen, B. K., & Thompson, C. (2019). A comparison study of ride comfort indices between Sperling's method and EN 12299. *International Journal of Rail Transportation*, *7*(4), 279–296. https://doi.org/10.1080/23248378.2019.1616329

Jin, X., Wu, L., Fang, J., Zhong, S., & Ling, L. (2012). An investigation into the mechanism of the polygonal wear of metro train wheels and its effect on the dynamic behaviour of a wheel/rail system. *Vehicle System Dynamics*, *50*(12), 1817–1834. https://doi.org/10.1080/00423114.2012.695022

Jin, X., Wu, Y., Liang, S., & Wen, Z. (2018). Mechanisms and Countermeasures of Out-of-Roundness Wear on Railway Vehicle Wheels. *Xinan Jiaotong Daxue Xuebao/Journal of Southwest Jiaotong University*, *53*(1), 1–14. https://doi.org/10.3969/j.issn.0258-2724.2018.01.001

Jo, J., & Bengio, Y. (2017). Measuring the tendency of CNNs to Learn Surface Statistical Regularities. *ArXiv*, 1–13. https://doi.org/10.48550/arxiv.1711.11561

Johansson, A., & Andersson, C. (2005). Out-of-round railway wheels - A study of wheel polygonalization through simulation of three-dimensional wheel-rail interaction and wear. *Vehicle System Dynamics*, *43*(8). https://doi.org/10.1080/00423110500184649

Kennedy, J., & Eberhart, R. (1995). *Particle Swarm Optimization, Proceedings of IEEE International Conference on Neural Networks Vol. IV: 1942–1948.* Neural Networks.

KLW WheelCo SA. (2019). *iWheel: KLW customer newsletter* (Issue 8). https://interpipe.biz/upload/catalog/2019120209582825c2437341469ed4151fb73d579a79ea.pdf

Komorski, P., Nowakowski, T., Szymanski, G. M., & Tomaszewski, F. (2018). Application of Time-Frequency Analysis of Acoustic Signal to Detecting Flat Places on the Rolling Surface of a Tram Wheel. *Springer Proceedings in Mathematics and Statistics*, *249*. https://doi.org/10.1007/978-3-319-96601-4_19

Komorski, P., Szymanski, G. M., Nowakowski, T., Orczyk, M., & Awrejcewicz, J. (2021). Advanced acoustic signal analysis used for wheel-flat detection. *Latin American Journal of Solids and Structures*, *18*(1). https://doi.org/10.1590/1679-78256086

Kouroussis, G., Kinet, D., Moeyaert, V., Dupuy, J., & Caucheteur, C. (2016). Railway structure monitoring solutions using fibre Bragg grating sensors. *International Journal of Rail Transportation*, *4*(3), 135–150. https://doi.org/10.1080/23248378.2016.1184598

Lan, Q., Dhanasekar, M., & Handoko, Y. A. (2019). Wear damage of out-of-round wheels in rail wagons under braking. *Engineering Failure Analysis*, *102*. https://doi.org/10.1016/j.engfailanal.2019.04.019

Lewis, R., & Olofsson, U. (2009). Wheel-Rail Interface Handbook. In *Wheel-Rail Interface Handbook*. https://doi.org/10.1533/9781845696788

Li, H., Li, X., Jia, R., Bai, L., & Luo, X. (2016). Fault diagnosis of vibration for hydropower units based on empirical mode decomposition and support vector machine. *Shuili Fadian Xuebao/Journal of Hydroelectric Engineering*, *35*(12), 105–111. https://doi.org/10.11660/slfdxb.20161211

Liu, J., Ding, X., & Wang, C. (2007). Adaptive resonance demodulation method and its application to fault diagnosis of freight car rolling bearings. *Zhendong Yu Chongji/Journal of Vibration and Shock*, *26*(1), 38–41.

Ma, W., Song, R., & Luo, S. (2016). Study on the mechanism of the formation of polygon-shaped wheels on subway vehicles. *Proceedings of the Institution of Mechanical Engineers, Part F: Journal of Rail and Rapid Transit*, *230*(1), 129–137. https://doi.org/10.1177/0954409714529269

MATLAB®. (2018). *Release R2018a* (Release R2018a). The MathWorks Inc.

Meinke, P., & Meinke, S. (1999). Polygonalization of wheel treads caused by static and dynamic imbalances. *Journal of Sound and Vibration*, *227*(5), 979–986.

Meixedo, A., Goncalves, A., Calcada, R., Gabriel, J., Fonseca, H., & Martins, R. (2016). Weighing in motion and wheel defect detection of rolling stock. *Exp.at 2015 - 3rd Experiment International Conference: Online Experimentation*, 2–4. https://doi.org/10.1109/EXPAT.2015.7463220

Montenegro, P. A. (2015). *A methodology for the assessment of the train running safety on bridges* [PhD Thesis, Faculty of Engineering of the University of Porto]. https://hdl.handle.net/10216/78571

Montenegro, P. A., Calçada, R., Carvalho, H., Bolkovoy, A., & Chebykin, I. (2020). Stability of a train running over the Volga river high-speed railway bridge during crosswinds. *Structure and Infrastructure Engineering*, *16*(8), 1121–1137. https://doi.org/10.1080/15732479.2019.1684956

Montenegro, P. A., Carvalho, H., Ribeiro, D., Calçada, R., Tokunaga, M., Tanabe, M., & Zhai, W. M. (2021). Assessment of train running safety on bridges: A literature review. In *Engineering Structures* (Vol. 241, p. 112425). https://doi.org/10.1016/j.engstruct.2021.112425

Montenegro, P. A., Heleno, R., Carvalho, H., Calçada, R., & Baker, C. J. (2020). A comparative study on the running safety of trains subjected to crosswinds simulated with different wind models. *Journal of Wind Engineering and Industrial Aerodynamics*, *207*, 104398. https://doi.org/10.1016/j.jweia.2020.104398

Montenegro, P. A., Neves, S. G. M., Azevedo, A. F. M., & Calçada, R. (2013). A nonlinear vehicle-structure interaction methodology with wheel-rail detachment and reattachment. *ECCOMAS Thematic Conference - COMPDYN 2013: 4th International Conference on Computational Methods*

in Structural Dynamics and Earthquake Engineering, Proceedings - An IACM Special Interest Conference. https://doi.org/10.7712/120113.4533.c1269

Montenegro, P. A., Neves, S. G. M., Calçada, R., Tanabe, M., & Sogabe, M. (2015). Wheel–rail contact formulation for analyzing the lateral train–structure dynamic interaction. *Computers & Structures*, *152*, 200–214. https://doi.org/10.1016/J.COMPSTRUC.2015.01.004

Morys, B. (1999). Enlargement of out-of-round wheel profiles on high speed trains. *Journal of Sound and Vibration*, *227*(5), 965–978. https://doi.org/10.1006/jsvi.1999.2055

Mosleh, A., Costa, P. A., & Calçada, R. (2020). A new strategy to estimate static loads for the dynamic weighing in motion of railway vehicles. *Proceedings of the Institution of Mechanical Engineers, Part F: Journal of Rail and Rapid Transit*, *234*(2), 183–200. https://doi.org/10.1177/0954409719838115

Mosleh, A., Costa, P., & Calçada, R. (2019). Development of a low-cost trackside system for weighing in motion and wheel defects detection. In *International Journal of Railway Research* (Vol. 7, Issue 1, pp. 1–9). https://doi.org/10.22068/IJRARE.7.1.1

Mosleh, A., Meixedo, A., Ribeiro, D., Montenegro, P., & Calçada, R. (2022a). Automatic clustering-based approach for train wheels condition monitoring. *International Journal of Rail Transportation*, 1–26. https://doi.org/10.1080/23248378.2022.2096132

Mosleh, A., Meixedo, A., Ribeiro, D., Montenegro, P., & Calçada, R. (2022b). Early wheel flat detection: an automatic data-driven wavelet-based approach for railways. *Vehicle System Dynamics*, 1–30. https://doi.org/10.1080/00423114.2022.2103436

Mosleh, A., Montenegro, P., Costa, P. A., & Calçada, R. (2020). An approach for wheel flat detection of railway train wheels using envelope spectrum analysis. *Structure and Infrastructure Engineering*, *17*(12), 1710–1729. https://doi.org/10.1080/15732479.2020.1832536

Mosleh, A., Montenegro, P., Costa, P., & Calçada, R. (2021). Railway vehicle wheel flat detection with multiple records using spectral kurtosis analysis. *Applied Sciences*, *11*(9), 1–25. https://doi.org/10.3390/app11094002

Mosleh, A., Montenegro, P., Costa, P., & Calçada, R. (2022). Approaches for weigh-in-motion and wheel defect detection of railway vehicles. In R. Calçada & S. Kaewunruen (Eds.), *Rail Infrastructure Resilience, A Best-Practices Handbook. Woodhead Publishing Series in Civil and Structural Engineering* (1st ed., pp. 183–207). Woodhead Publishing. https://doi.org/10.1016/B978-0-12-821042-0.00009-5

Müller, R., & Diener, M. (1995). Verschleißerscheinungen an Radlaufflächen von Eisenbahnfahrzeugen (Wear phenomena on wheel treads of railway vehicles). *ZEV + DET Glasers Annalen (Zeitschrift Für Eisenbahnwesenund Verkehrstechnik)*, *119*(6), 177–192.

Neto, J., Montenegro, P. A., Vale, C., & Calçada, R. (2021). Evaluation of the train running safety under crosswinds - a numerical study on the influence of the wind speed and orientation considering the normative Chinese Hat Model. *International Journal of Rail Transportation*, *9*(3), 1–28. https://doi.org/10.1080/23248378.2020.1780965

Neves, J., Ribeiro, D., & Ribeiro, Á. (2019). TESTE2019 - 2nd Conference on Testing and Experimentations in Civil Engineering - Proceedings. *TESTE2019 - 2nd Conference on Testing and Experimentations in Civil Engineering - Proceedings*, 19–21. https://doi.org/10.5281/ZENODO.3355354

Neves, S. G. M., Azevedo, A. F. M., & Calçada, R. (2012). A direct method for analyzing the vertical vehicle–structure interaction. *Engineering Structures*, *34*, 414–420. https://doi.org/10.1016/J.ENGSTRUCT.2011.10.010

Neves, S. G. M., Montenegro, P. A., Azevedo, A. F. M., & Calçada, R. (2014). A direct method for analyzing the nonlinear vehicle–structure interaction. *Engineering Structures*, *69*, 83–89. https://doi.org/10.1016/J.ENGSTRUCT.2014.02.027

Nielsen, J. C. O., & Johansson, A. (2000). Out-of-round railway wheels-a literature survey. *Proceedings of the Institution of Mechanical Engineers, Part F: Journal of Rail and Rapid Transit*, *214*(2), 79–91. https://doi.org/10.1243/0954409001531351

Pallgen, G. (1998). Unrunde Räder an Eisenbahnfahrzeugen. *Eisenbahningenieur*, *49*(1), 56–60.

Peng, B., Iwnicki, S., Shackleton, P., Zhao, Y., & Cui, D. (2018). A practical method for simulating the evolution of railway wheel polygonalization. *The Dynamics of Vehicles on Roads and Tracks*, *2*, 753–758.

Phanyakit, T., & Satiennam, T. (2018). Track-quality index and degradation of railway track structure: The construction track doubling project of northeast line from thanon chira junction to khon kaen station, Thailand. *MATEC Web of Conferences*, *192*. https://doi.org/10.1051/matecconf/201819202022

Pintão, B. (2021). *Avaliação de metodologia para pesagem dinâmica de comboios* [Faculdade de Engenharia da Universidade do Porto]. https://hdl.handle.net/10216/135099

Rode, W., Müller, D., & Villman, J. (1997, November 13). Results of DB AG investigations 'out-of-round wheels'. *Proceedings Corrugation Symposium—Extended Abstracts, IFV Bahntechink, Technische Universität Berlin, Berlin, Germany*.

Sadeghi, J., Seyedkazemi, M., & Khajehdezfuly, A. (2020). Nonlinear simulation of vertical behavior of railway fastening system. *Engineering Structures*, *209*, 110340. https://doi.org/10.1016/J.ENGSTRUCT.2020.110340

Shevtsov, I. Y. (2008). *Wheel/Rail Interface Optimisation* [Doctoral Dissertation, Delft University of Technology]. http://resolver.tudelft.nl/uuid:a728ca2a-9fa9-4b0f-959f-2fca6ca25365

Snyder, T., Stone, D. H., & Kristan, J. (2003). Wheel flat and out-of round formation and growth. *Proceedings of the IEEE/ASME Joint Railroad Conference*, 143–148. https://doi.org/10.1115/rtd2003-1659

Song, Y., Wang, Z., & Du, Y. (2014). Study on train wheel out-of-roundness monitoring method by PVDF sensing technology. *Open Mechanical Engineering Journal*, *8*(1). https://doi.org/10.2174/1874155X01408010077

Steenbergen, M. J. M. M. (2008). The role of the contact geometry in wheel-rail impact due to wheel flats: Part II. *Vehicle System Dynamics*, *46*(8), 713–737. https://doi.org/10.1080/00423110701584027

Stratman, B., Liu, Y., & Mahadevan, S. (2007). Structural Health Monitoring of Railroad Wheels Using Wheel Impact Load Detectors. *Journal of Failure Analysis and Prevention*, *7*(3), 218–225. https://doi.org/10.1007/s11668-007-9043-3

Takemiya, H., & Bian, X. (2005). Substructure Simulation of Inhomogeneous Track and Layered Ground Dynamic Interaction under Train Passage. *Journal of Engineering Mechanics*, *131*(7), 699–711. https://doi.org/10.1061/(asce)0733-9399(2005)131:7(699)

Tao, G., Wen, Z., Liang, X., Ren, D., & Jin, X. (2019). An investigation into the mechanism of the out-of-round wheels of metro train and its mitigation measures. *Vehicle System Dynamics*, *57*(1). https://doi.org/10.1080/00423114.2018.1445269

Thompson, D. (2009). Railway Noise and Vibration: Mechanisms, Modelling and Means of Control. In *Railway Noise and Vibration*. Elsevier Science. https://doi.org/10.1016/B978-0-08-045147-3.X0023-0

Trilla, A., Bob-Manuel, J., Lamoureux, B., & Vilasis-Cardona, X. (2021). Integrated Multiple-Defect Detection and Evaluation of Rail Wheel Tread Images using Convolutional Neural Networks. *International Journal of Prognostics and Health Management*, *12*(1), 1–19. https://doi.org/10.36001/ijphm.2021.v12i1.2906

Vale, C. (2021). Wheel flats in the dynamic behavior of ballasted and slab railway tracks. *Applied Sciences (Switzerland)*, *11*(15). https://doi.org/10.3390/app11157127

Vale, C., & Calçada, R. (2014). A Dynamic Vehicle-Track Interaction Model for Predicting the Track Degradation Process. *Journal of Infrastructure Systems*, *20*(3). https://doi.org/10.1061/(asce)is.1943-555x.0000190

Vernersson, T. (1999a). Thermally induced roughness of tread braked railway wheels: Part 2: modelling and field measurements. *Wear*, *236*(1–2), 106–116. https://doi.org/10.1016/S0043-1648(99)00261-6

Vernersson, T. (1999b). Thermally induced roughness of tread-braked railway wheels: Part 1: brake rig experiments. *Wear*, *236*(1–2), 96–105. https://doi.org/10.1016/S0043-1648(99)00260-4

Vernersson, T., & Järnvägsmekanik, K. C. (1996). *Non-roundness of Block-braked Railway Wheels: A Literature Survey*. Department of Solid Mechanics, Chalmers University of Technology. https://books.google.pt/books?id=rdiZMwAACAAJ

Vostroukhov, A. v., & Metrikine, A. v. (2003). Periodically supported beam on a visco-elastic layer as a model for dynamic analysis of a high-speed railway track. *International Journal of Solids and Structures*, *40*(21), 5723–5752. https://doi.org/10.1016/S0020-7683(03)00311-1

Wang, P., Wang, X., Wang, Y., & Zhang, R. (2020). Polygonal Wheel Detection Model Based on Track Irregularity of High-Speed Railways. *Xinan Jiaotong Daxue Xuebao/Journal of Southwest Jiaotong University*, *55*(4). https://doi.org/10.3969/j.issn.0258-2724.20180283

Wang, R., Crosbee, D., Beven, A., Wang, Z., & Zhen, D. (2020). Vibration-Based Detection of Wheel Flat on a High-Speed Train. *Smart Innovation, Systems and Technologies*, *166*, 159–169. https://doi.org/10.1007/978-3-030-57745-2_14

Wu, X., Rakheja, S., Ahmed, A. K. W., & Chi, M. (2018). Influence of a flexible wheelset on the dynamic responses of a high-speed railway car due to a wheel flat. *Proceedings of the Institution of Mechanical Engineers, Part F: Journal of Rail and Rapid Transit*, *232*(4), 1033–1048. https://doi.org/10.1177/0954409717708895

Wu, Y. S., & Yang, Y. bin. (2003). Steady-state response and riding comfort of trains moving over a series of simply supported bridges. *Engineering Structures*, *25*(2), 251–265. https://doi.org/10.1016/S0141-0296(02)00147-5

Xu, X., Liu, J., Sun, S., & Xie, W. (2020). Detection method for polygonalization of wheel treads based on dynamic response. *ACM International Conference Proceeding Series*. https://doi.org/10.1145/3450292.3450296

Yang, Y. B., Yau, J. D., & Wu, Y. S. (2004). Vehicle–Bridge Interaction Dynamics. In *Vehicle–Bridge Interaction Dynamics*. https://doi.org/10.1142/5541

Ye, Y., Shi, D., Krause, P., Tian, Q., & Hecht, M. (2020). Wheel flat can cause or exacerbate wheel polygonization. *Vehicle System Dynamics1604*, *58*(10), 1576–1604. https://doi.org/10.1080/00423114.2019.1636098

Zhai, W. M., Wang, Q. C., Lu, Z. W., & Wu, X. S. (2001). Dynamic effects of vehicles on tracks in the case of raising train speeds. *Proceedings of the Institution of Mechanical Engineers*, *215*(2), 125–135. https://doi.org/10.1243/0954409011531459

Zhai, W., Wang, K., & Cai, C. (2009). Fundamentals of vehicle-track coupled dynamics. *Vehicle System Dynamics*, *47*(11), 1349–1376. https://doi.org/10.1080/00423110802621561

Zhai, W., Xia, H., Cai, C., Gao, M., Li, X., Guo, X., Zhang, N., & Wang, K. (2013). International Journal of Rail Transportation High-speed train-track-bridge dynamic interactions-Part I: theoretical model and numerical simulation) High-speed train-track-bridge dynamic interactions-Part I: theoretical model and numerical simulation High-speed train-track-bridge dynamic interactions-Part I: theoretical model and numerical simulation. *International Journal of Rail Transportation*, *1*(2), 3–24. https://doi.org/10.1080/23248378.2013.791498

Zhang, Z., Entezami, M., Stewart, E., & Roberts, C. (2017). Enhanced fault diagnosis of roller bearing elements using a combination of empirical mode decomposition and minimum entropy deconvolution. *Proceedings of the Institution of Mechanical Engineers, Part C: Journal of Mechanical Engineering Science*, *231*(4), 655–671. https://doi.org/10.1177/0954406215623575

Zhao, X. N., Chen, G. X., Lv, J. Z., Zhang, S., Wu, B. W., & Zhu, Q. (2019). Study on the mechanism for the wheel polygonal wear of high-speed trains in terms of the frictional self-excited vibration theory. *Wear*, *426–427*, 1820–1827. https://doi.org/10.1016/J.WEAR.2019.01.020

APPENDIX

Accelerometers (layout scheme 2)

Wheel Flat

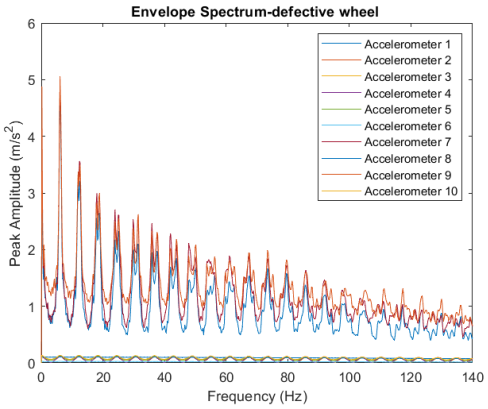

Wf2, *V*=60 km/h, track class 3

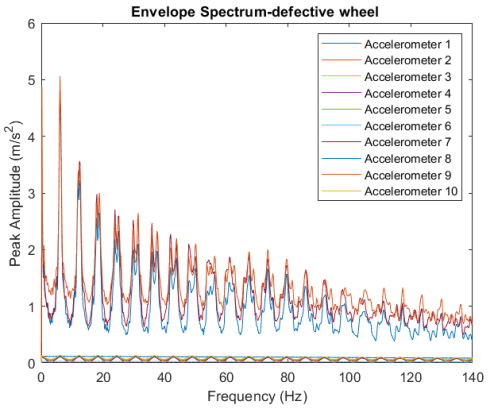

Wf2, *V*=60 km/h, track class 4

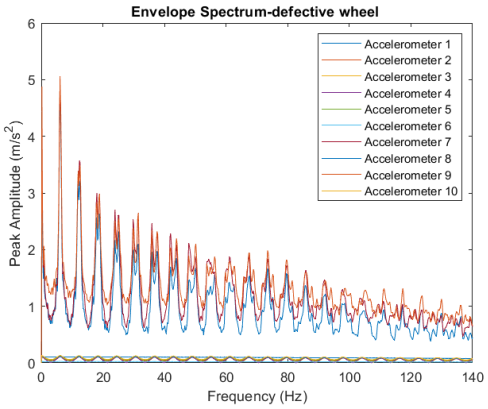

Wf2, *V*=60 km/h, track class 5

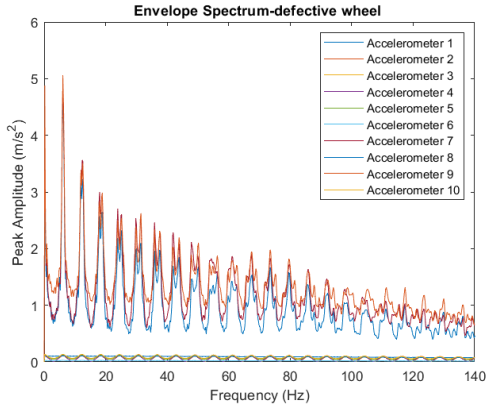

Wf2, *V*=60 km/h, track class 6

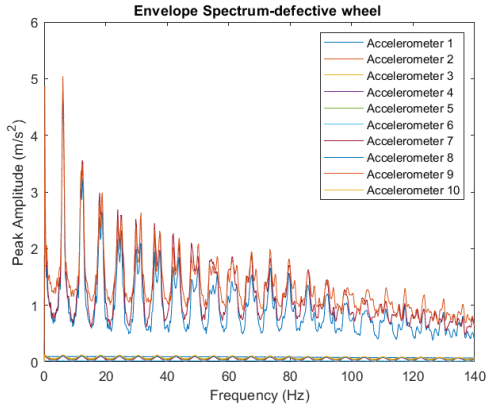

Wf2, *V*=60 km/h, track class 7

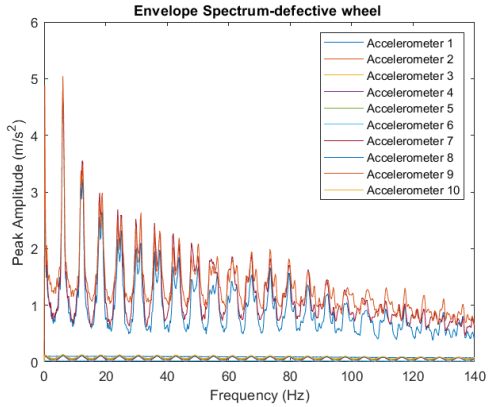

Wf2, *V*=60 km/h, track class 8

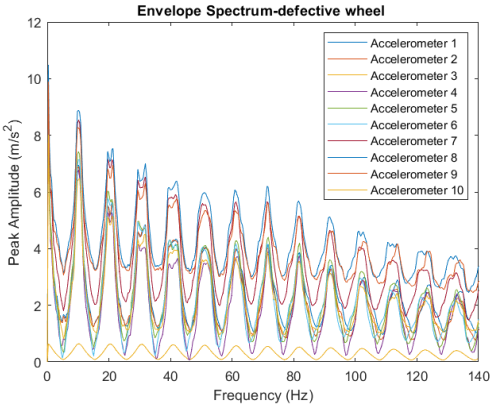

Wf2, *V*=100 km/h, track class 4

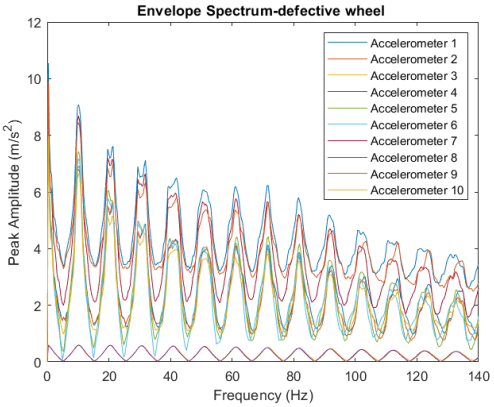

Wf2, *V*=100 km/h, track class 5

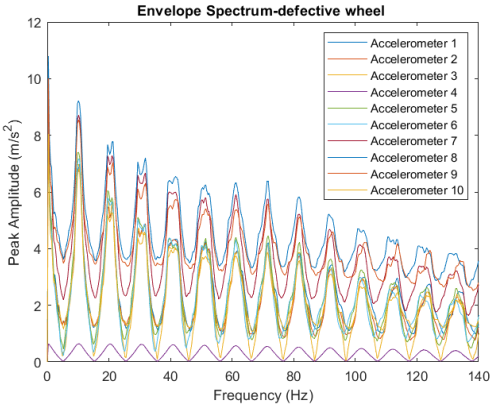

Wf2, *V*=100 km/h, track class 6

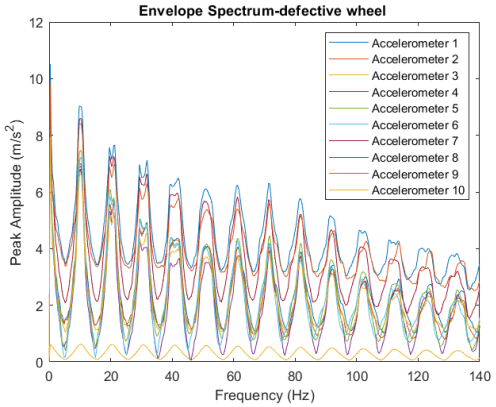

Wf2, *V*=100 km/h, track class 8

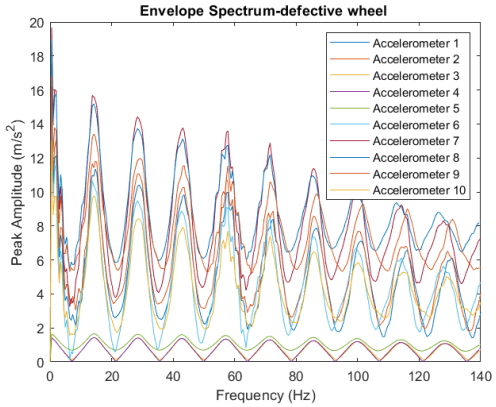

Wf2, *V*=140 km/h, track class 6

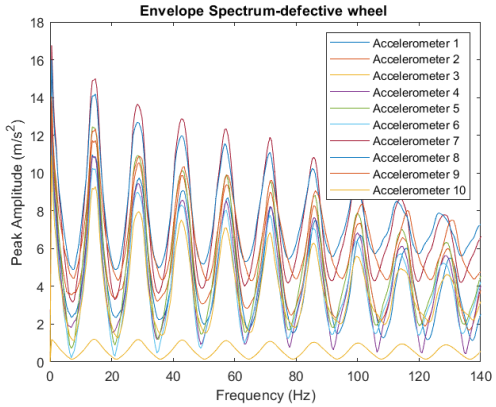

Wf2, *V*=140 km/h, track class 8

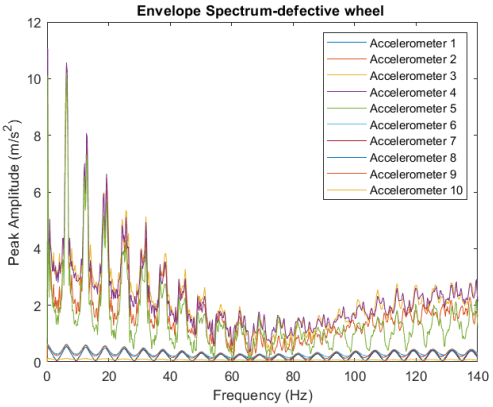

Wf3, *V*=60 km/h, track class 3

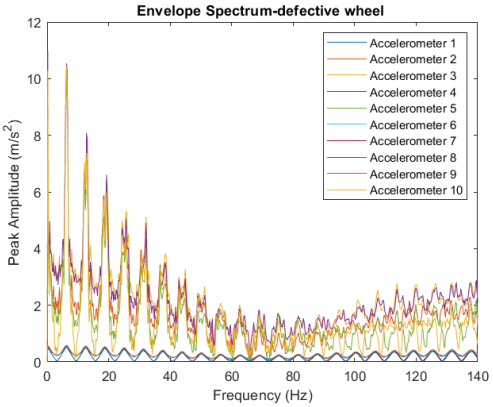

Wf3, *V*=60 km/h, track class 4

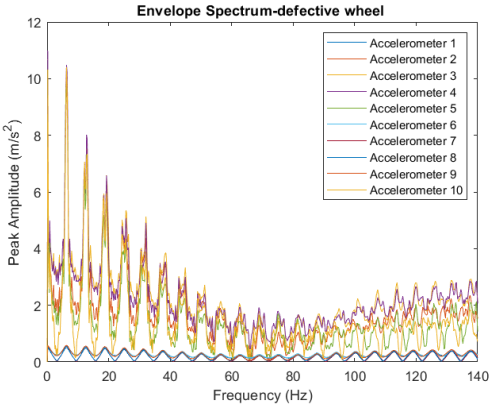

Wf3, *V*=60 km/h, track class 5

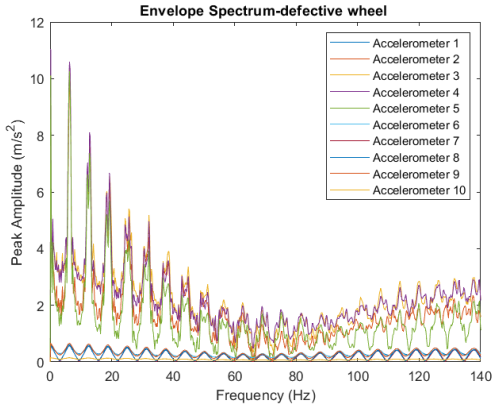

Wf3, *V*=60 km/h, track class 6

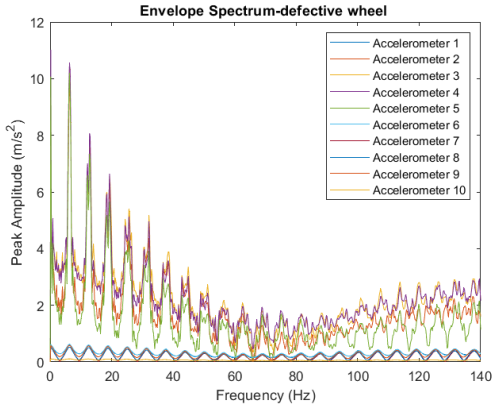

Wf3, *V*=60 km/h, track class 7

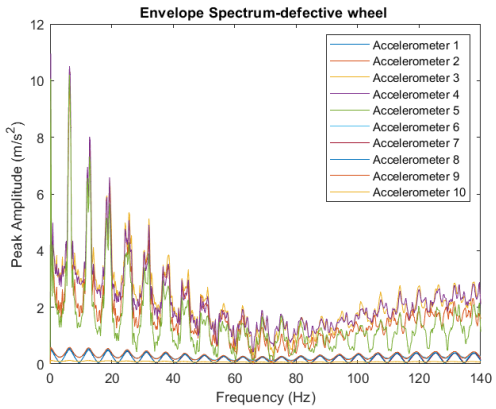

Wf3, *V*=60 km/h, track class 8

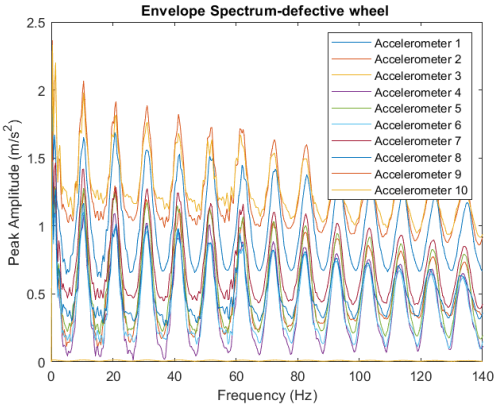

Wf3, *V*=100 km/h, track class 4

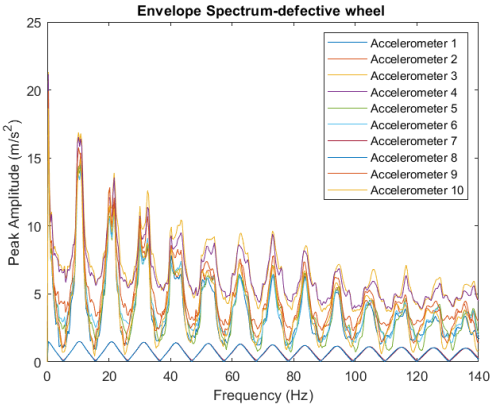

Wf3, *V*=100 km/h, track class 5

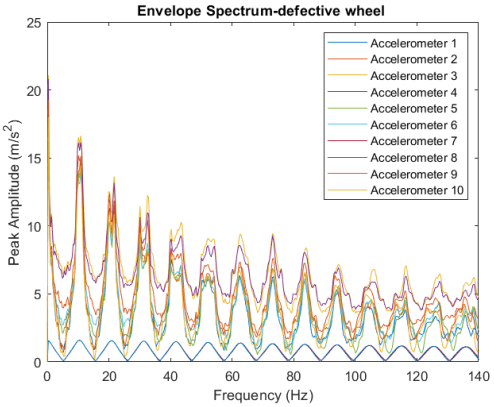

Wf3, *V*=100 km/h, track class 6

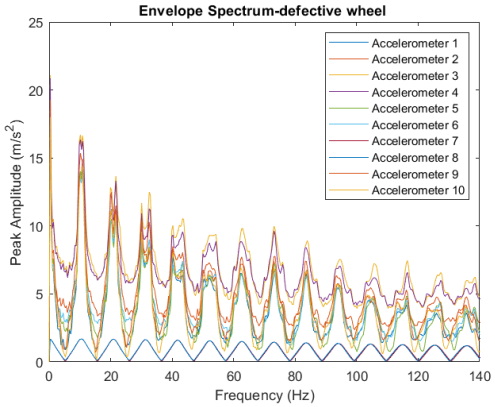

Wf3, *V*=100 km/h, track class 8

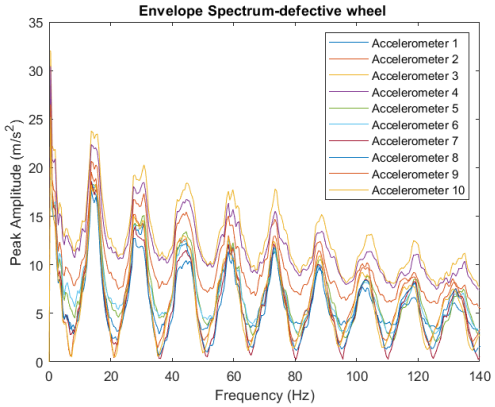

Wf3, *V*=140 km/h, track class 6

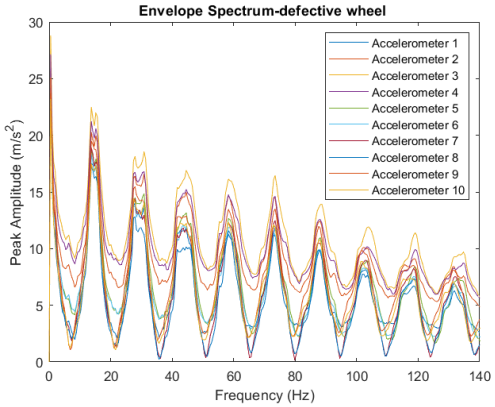

Wf3, *V*=140 km/h, track class 7

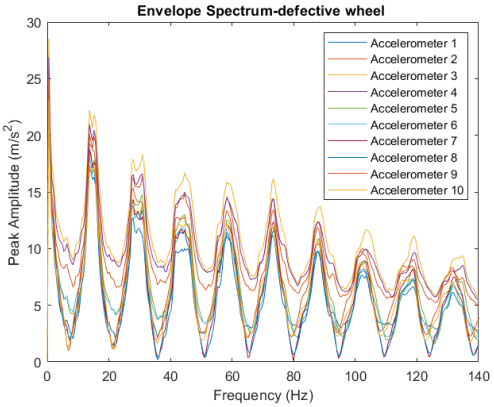

Wf3, *V*=140 km/h, track class 8

Polygonised Wheel

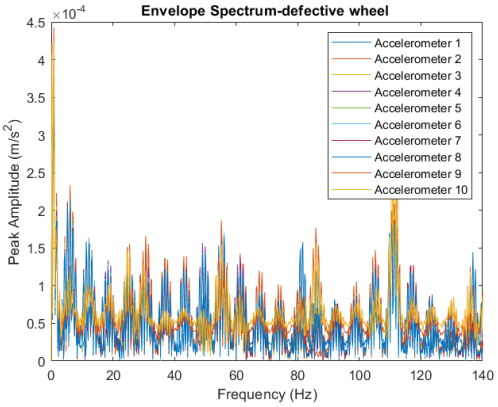

wp5, *V*=60 km/h, track class 7

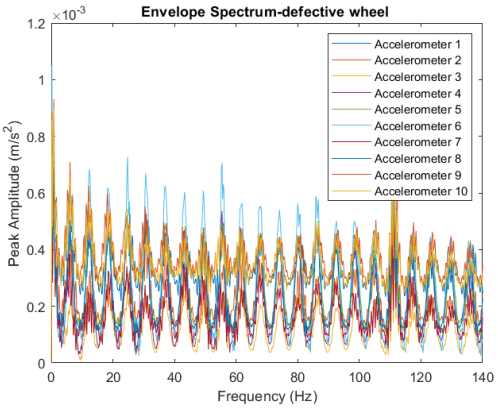

wp20, *V*=60 km/h, track class 7

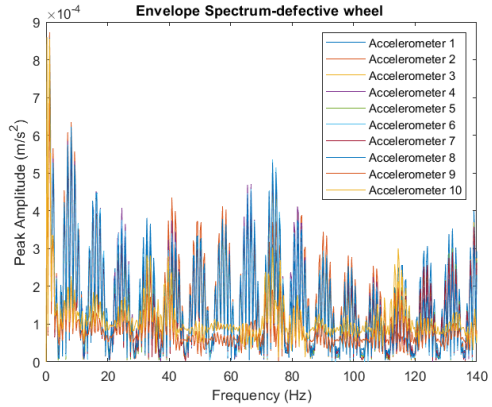

wp5, *V*=80 km/h, track class 7

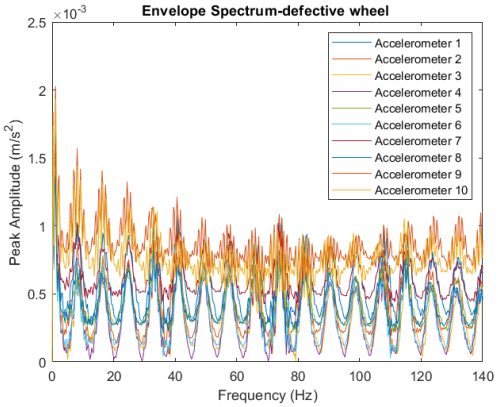

wp20, *V*=80 km/h, track class 7

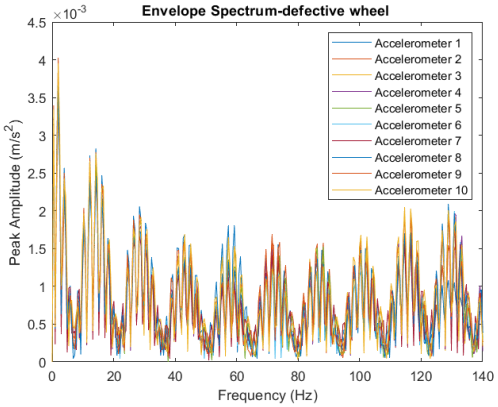

wp5, *V*=140 km/h, track class 7

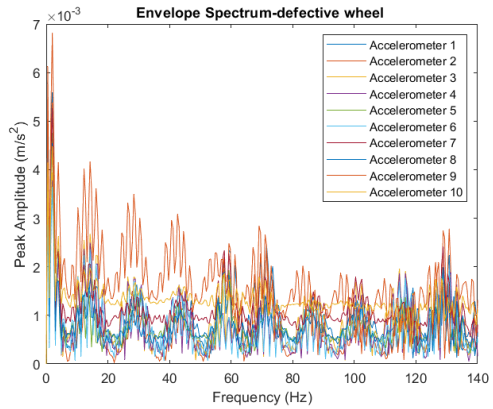

wp20, *V*=140 km/h, track class 7

Healthy Wheel

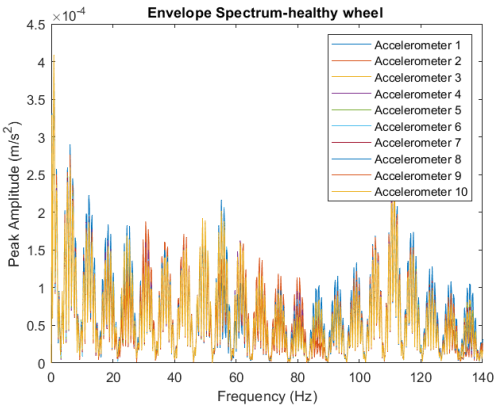

Healthy wheel, *V*=60 km/h, track class 7

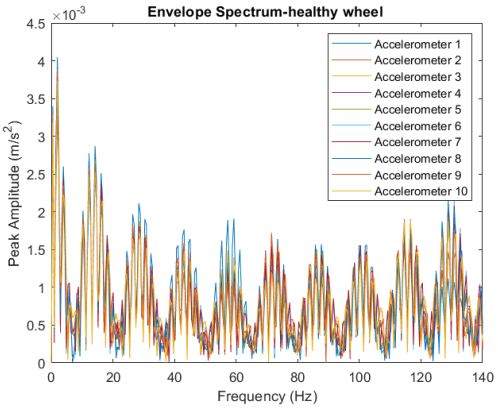

Healthy wheel, *V*=140 km/h, track class 7

Accelerometers (layout scheme 3)

Wheel Flat

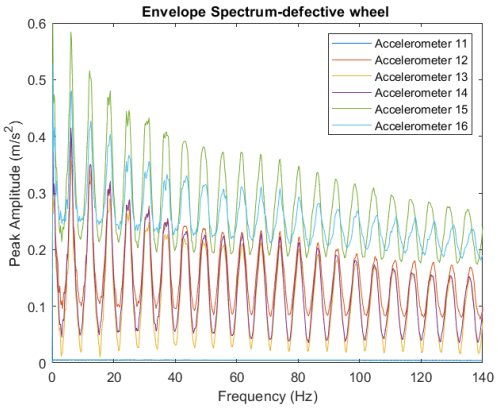

Wf1, *V*=60 km/h, track class 3

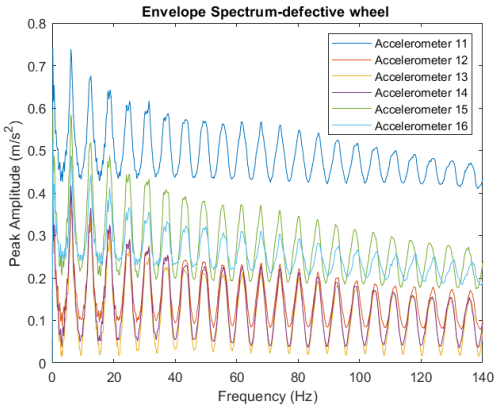

Wf1, *V*=60 km/h, track class 4

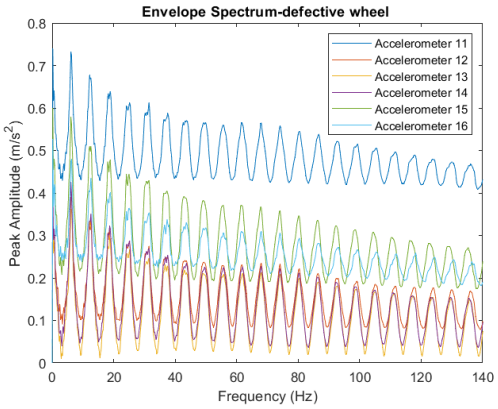

Wf1, *V*=60 km/h, track class 5

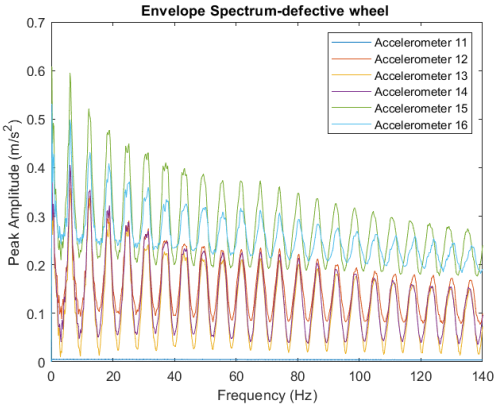

Wf1, *V*=60 km/h, track class 6

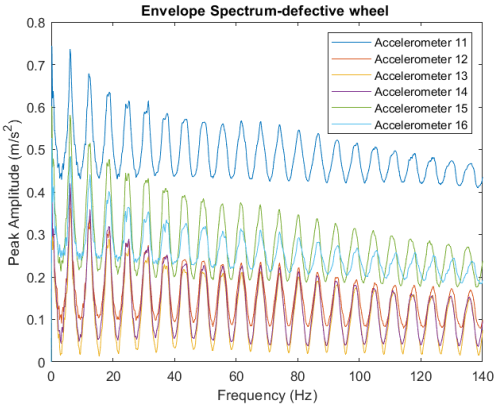

Wf1, *V*=60 km/h, track class 7

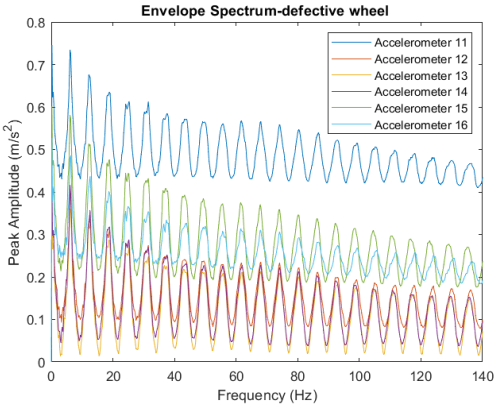

Wf1, *V*=60 km/h, track class 8

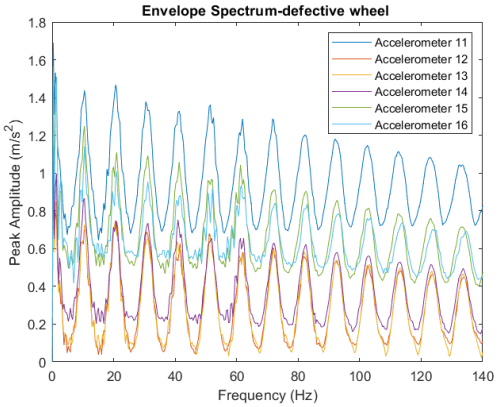

Wf1, *V*=100 km/h, track class 4

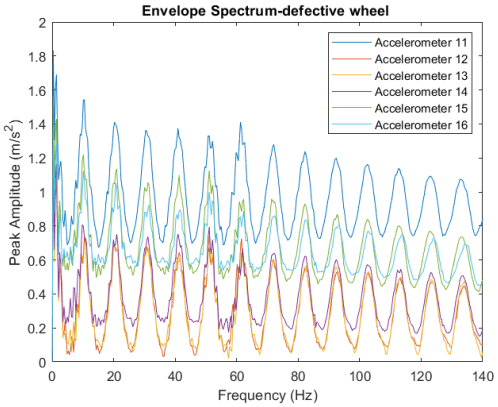

Wf1, *V*=100 km/h, track class 5

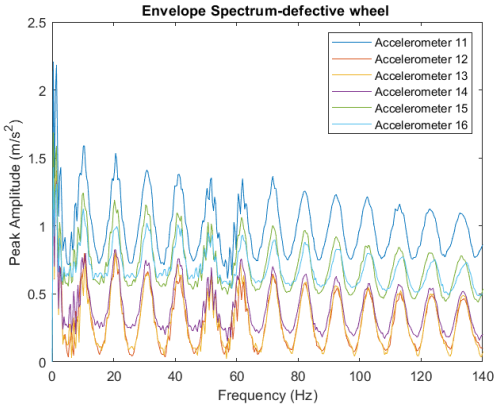

Wf1, *V*=100 km/h, track class 6

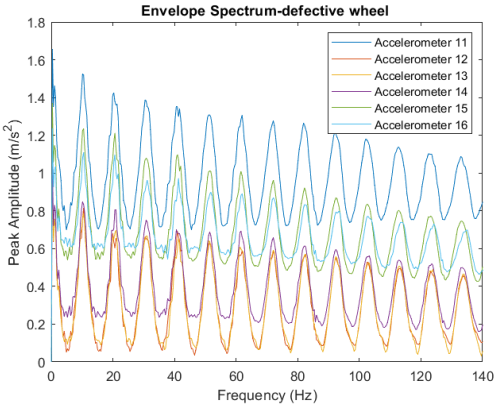

Wf1, *V*=100 km/h, track class 7

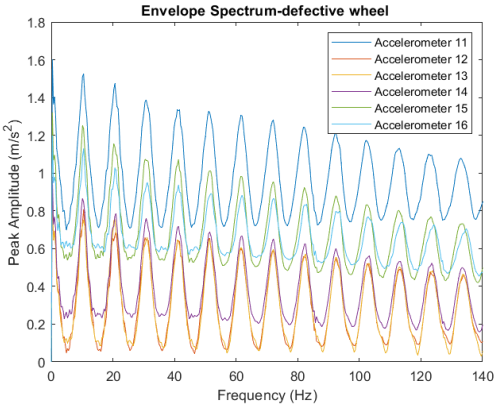

Wf1, *V*=100 km/h, track class 8

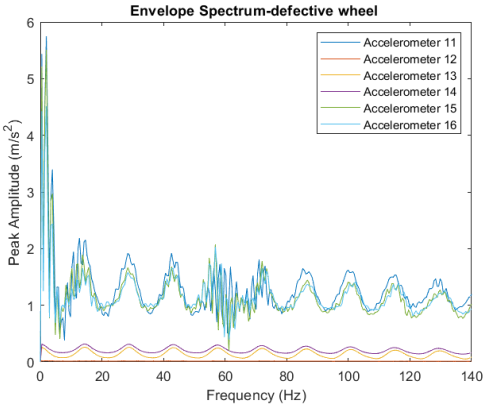

Wf1, *V*=140 km/h, track class 6

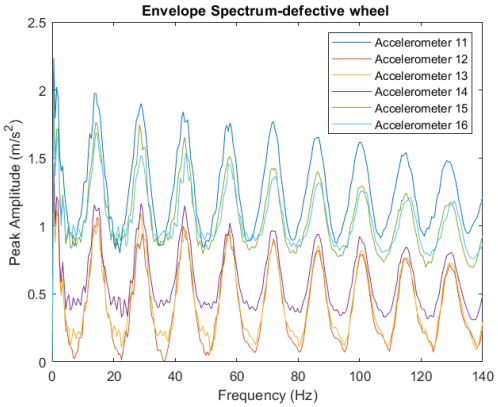

Wf1, *V*=140 km/h, track class 7

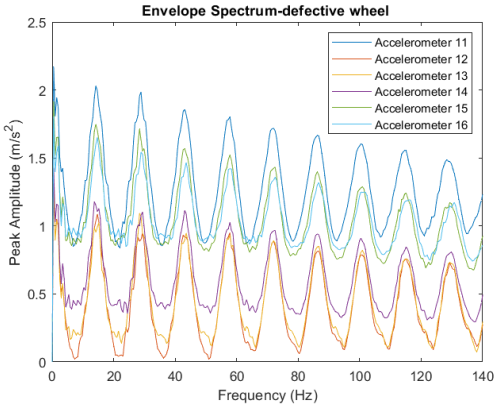

Wf1, *V*=140 km/h, track class 8

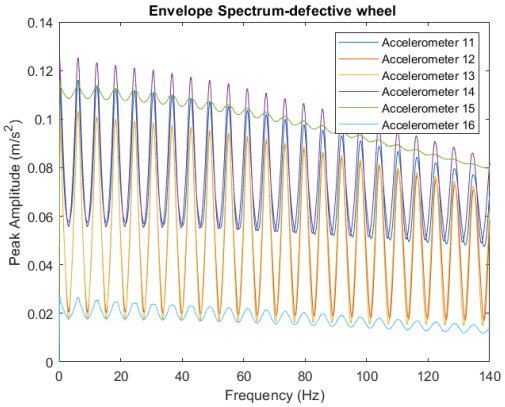

Wf2, *V*=60 km/h, track class 3

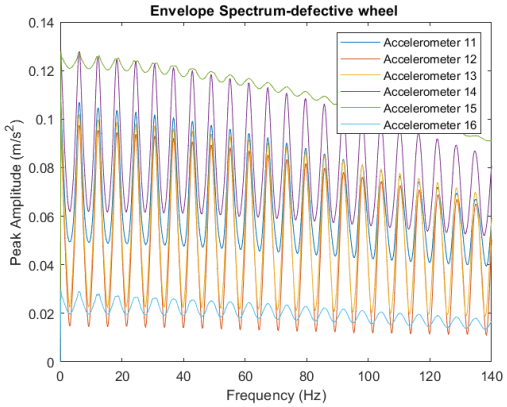

Wf2, *V*=60 km/h, track class 4

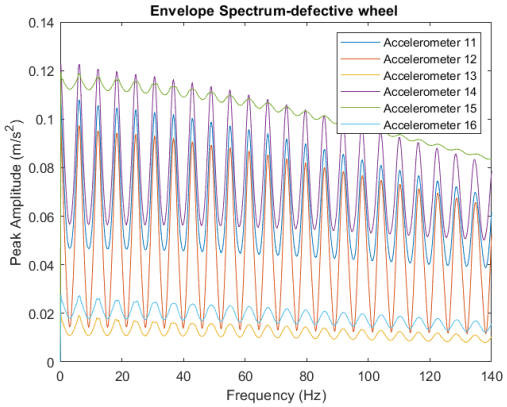

Wf2, *V*=60 km/h, track class 5

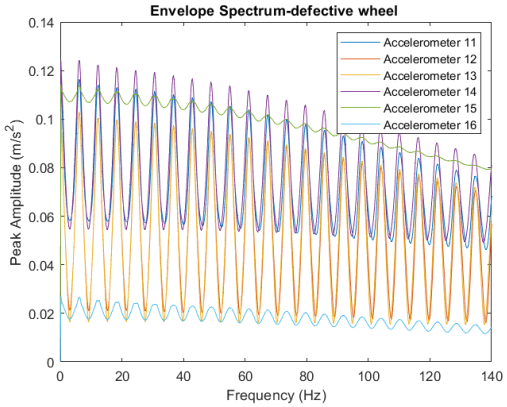

Wf2, *V*=60 km/h, track class 6

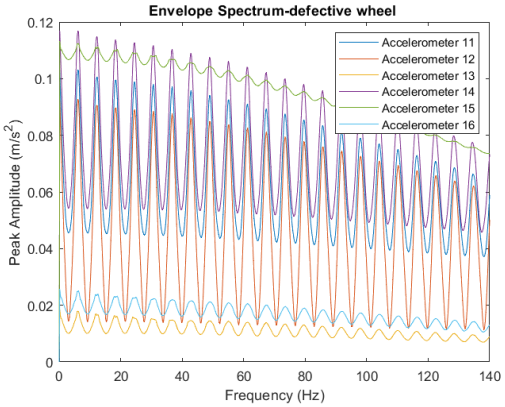

Wf2, *V*=60 km/h, track class 7

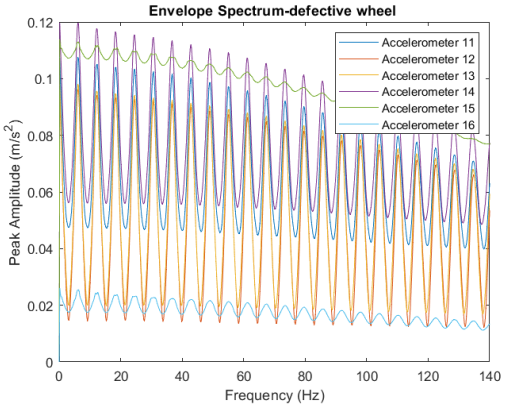

Wf2, *V*=60 km/h, track class 8

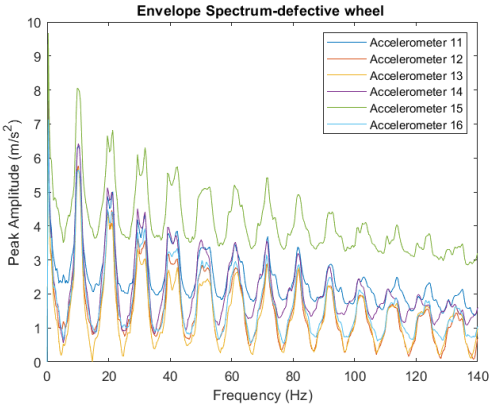

Wf2, *V*=100 km/h, track class 4

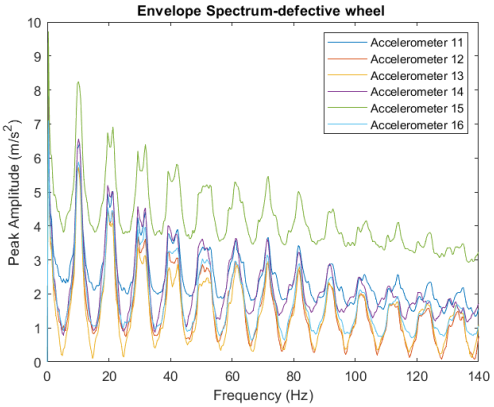

Wf2, *V*=100 km/h, track class 5

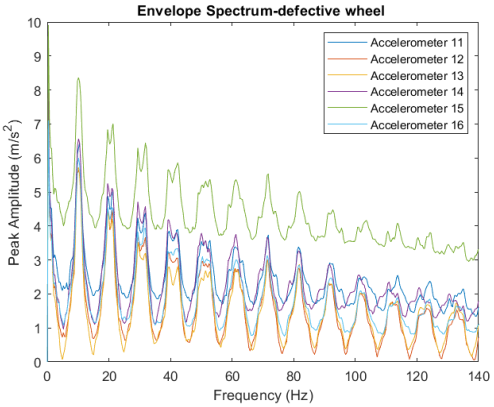

Wf2, *V*=100 km/h, track class 6

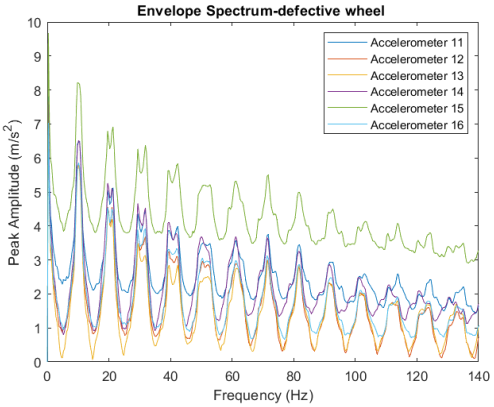

Wf2, *V*=100 km/h, track class 8

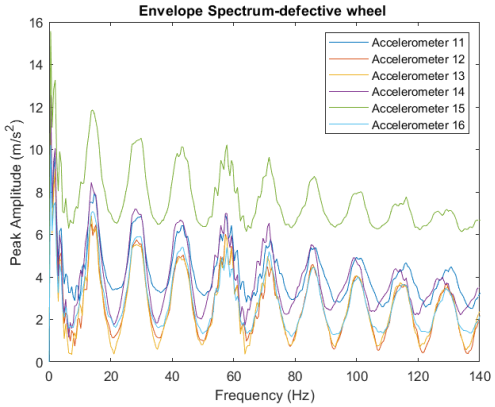

Wf2, *V*=140 km/h, track class 6

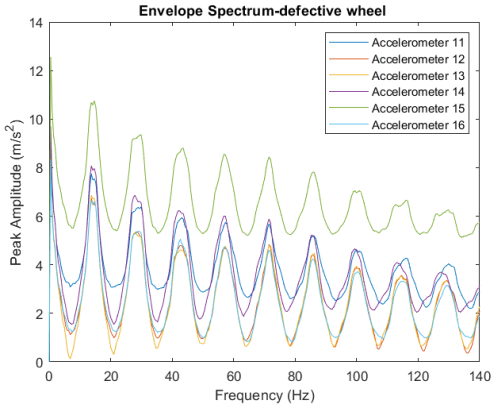

Wf2, *V*=140 km/h, track class 7

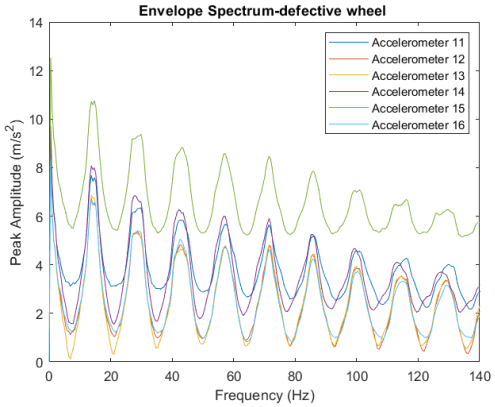

Wf2, *V*=140 km/h, track class 8

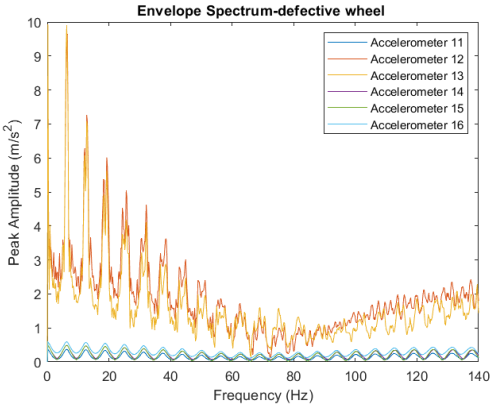

Wf3, *V*=60 km/h, track class 3

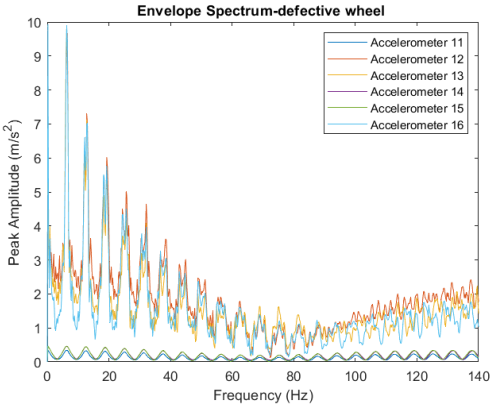

Wf3, *V*=60 km/h, track class 4

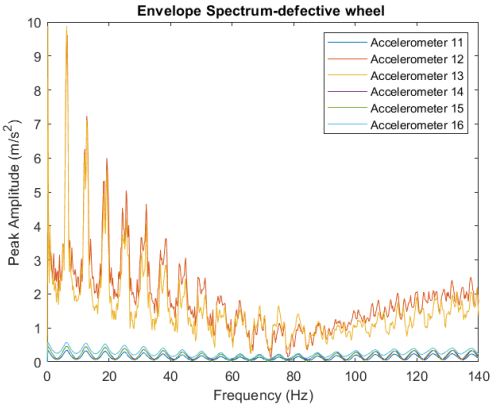

Wf3, *V*=60 km/h, track class 5

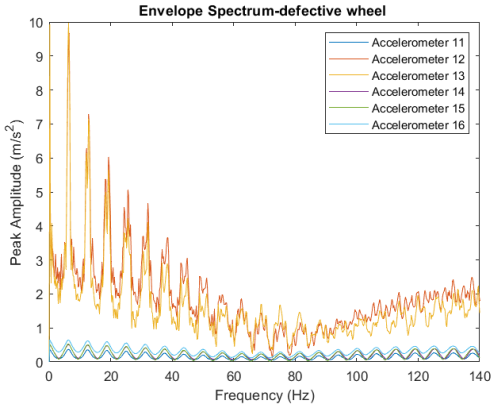

Wf3, *V*=60 km/h, track class 6

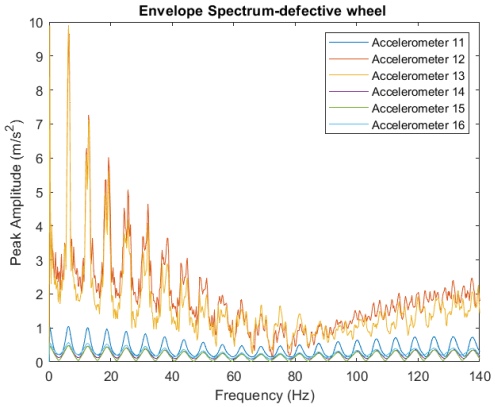

Wf3, *V*=60 km/h, track class 7

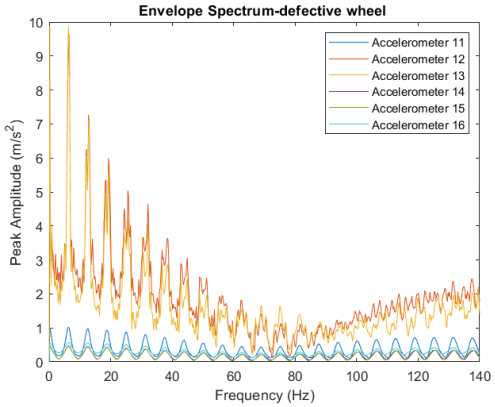

Wf3, *V*=60 km/h, track class 8

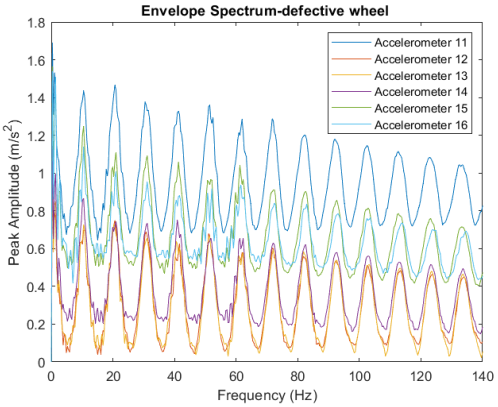

Wf3, *V*=100 km/h, track class 4

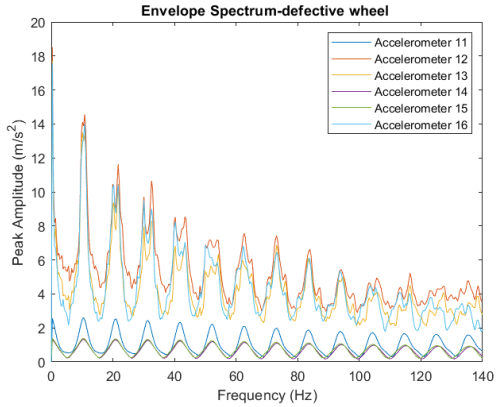

Wf3, *V*=100 km/h, track class 5

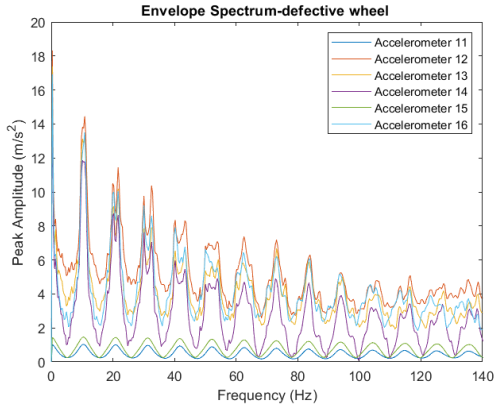

Wf3, *V*=100 km/h, track class 6

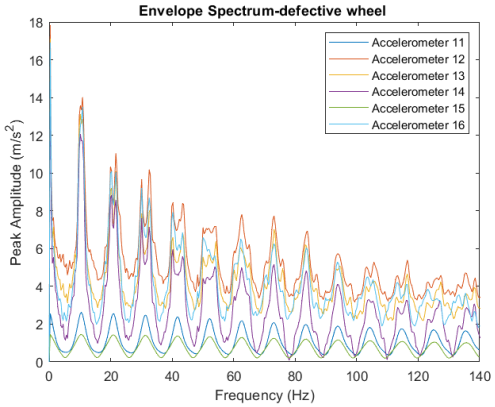

Wf3, *V*=100 km/h, track class 7

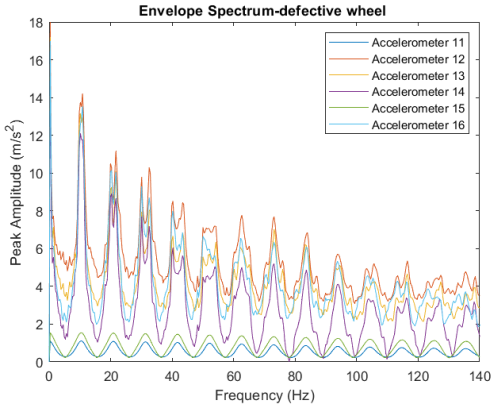

Wf3, *V*=100 km/h, track class 8

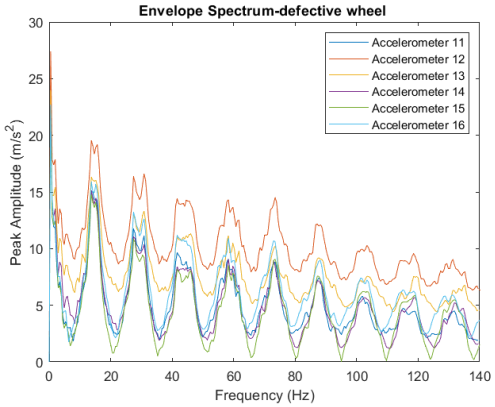

Wf3, *V*=140 km/h, track class 6

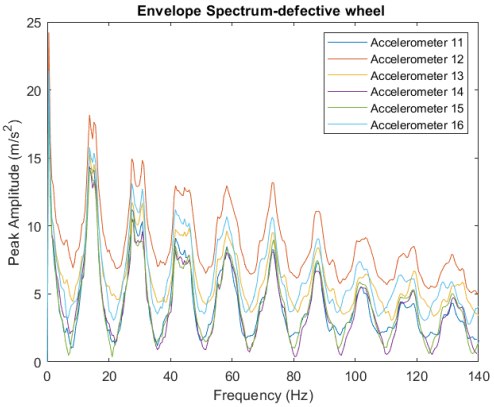

Wf3, *V*=140 km/h, track class 7

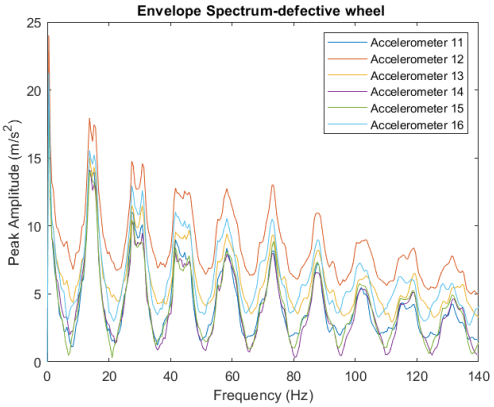

Wf3, *V*=140 km/h, track class 8

Polygonised Wheel

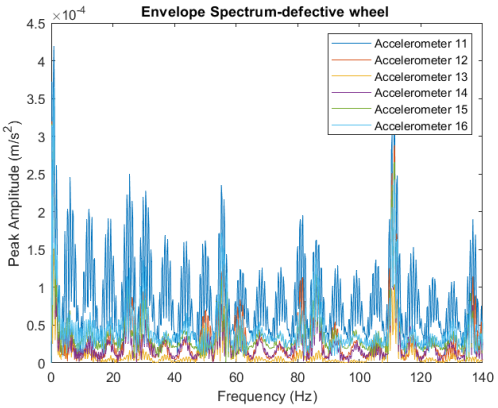

wp5, *V*=60 km/h, track class 7

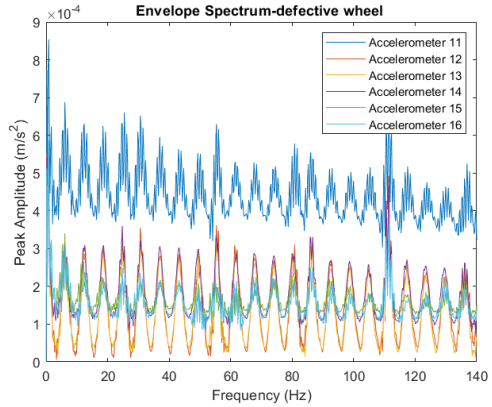

wp12, *V*=60 km/h, track class 7

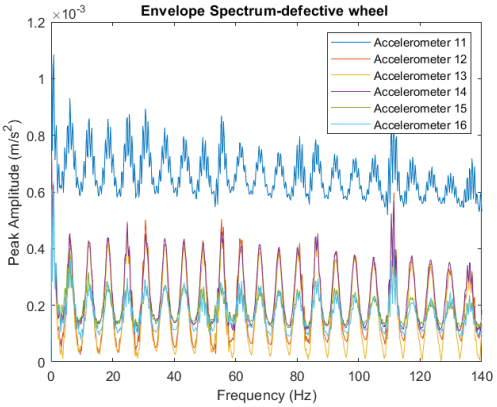

wp20, *V*=60 km/h, track class 7

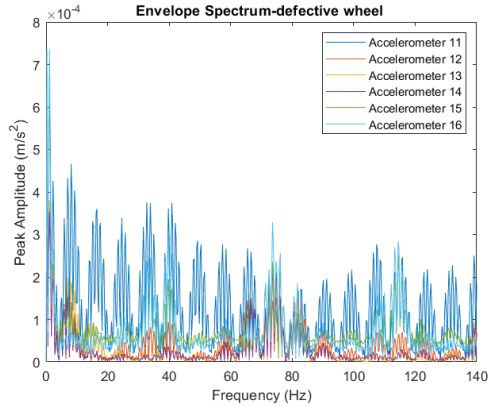

wp5, *V*=80 km/h, track class 7

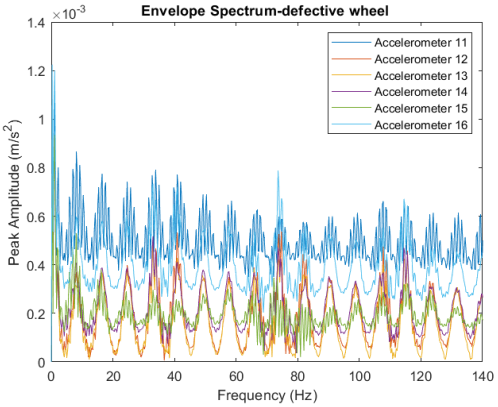

wp12, *V*=80 km/h, track class 7

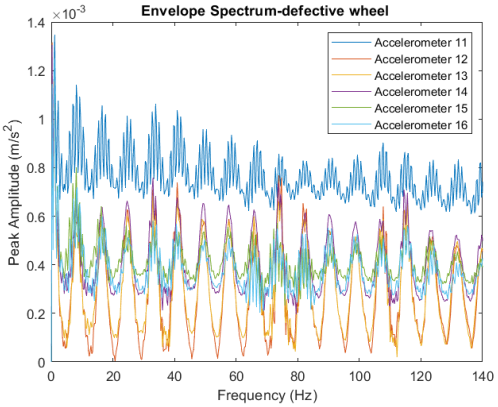

wp20, *V*=80 km/h, track class 7

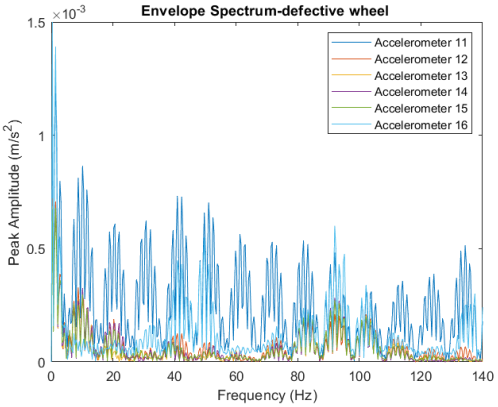

wp5, *V*=100 km/h, track class 7

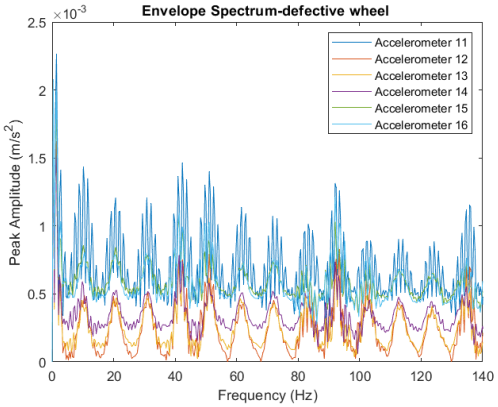

wp12, *V*=100 km/h, track class 7

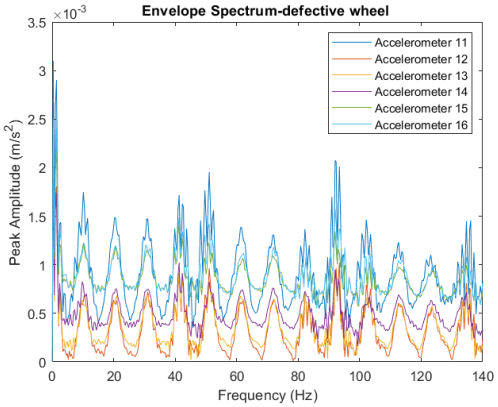

wp20, *V*=100 km/h, track class 7

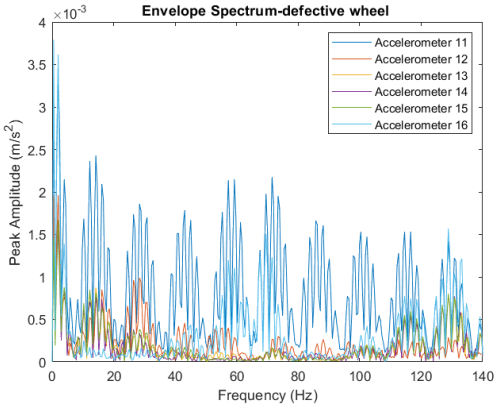

wp5, *V*=140 km/h, track class 7

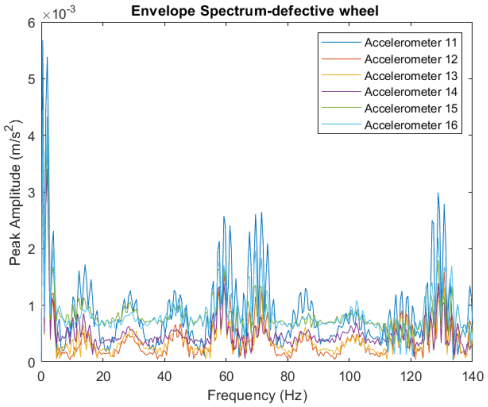

wp12, *V*=140 km/h, track class 7

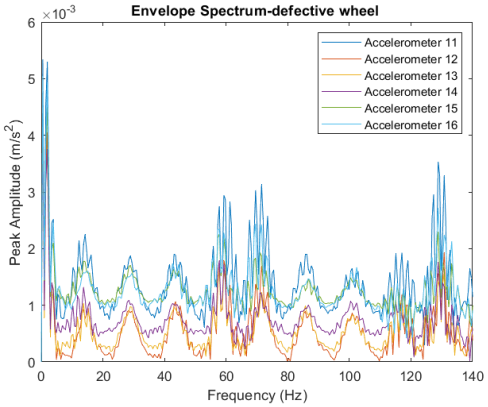

wp20, *V*=140 km/h, track class 7

Healthy Wheel

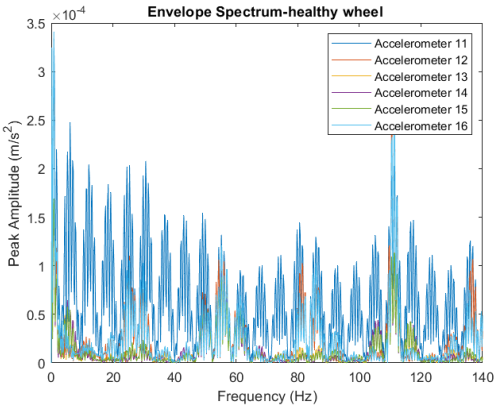

Healthy wheel, *V*=60 km/h, track class 7

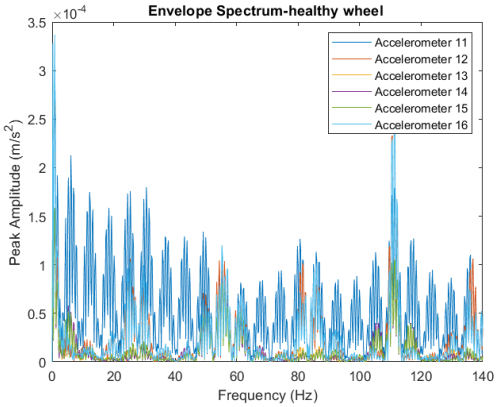

Healthy wheel, *V*=60 km/h, track class 8

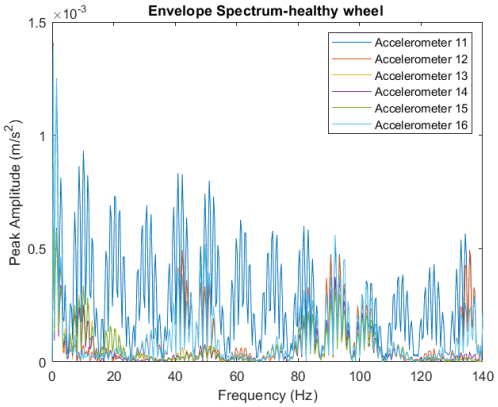

Healthy wheel, *V*=100 km/h, track class 8

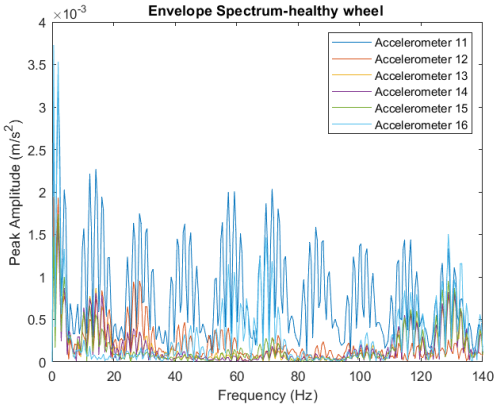

Healthy wheel, *V*=140 km/h, track class 7

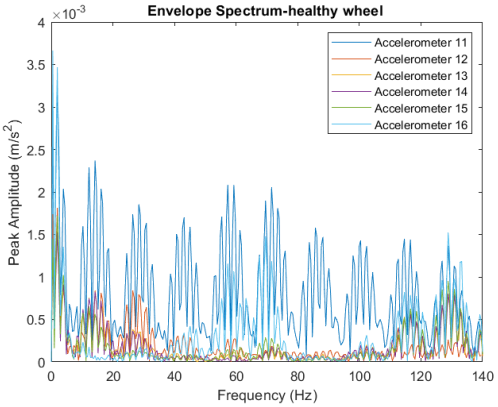

Healthy wheel, *V*=140 km/h, track class 8

Strain Gauge Sensors (layout scheme 1)

Wheel Flat

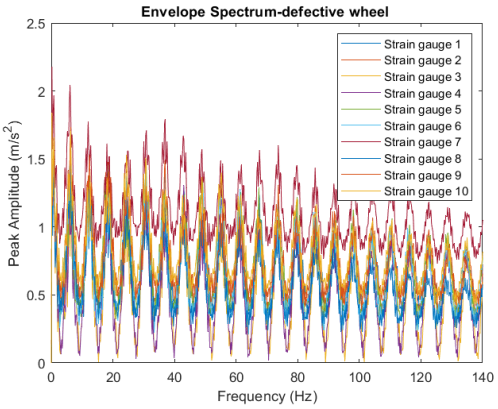

Wf2, *V*=60 km/h, track class 3

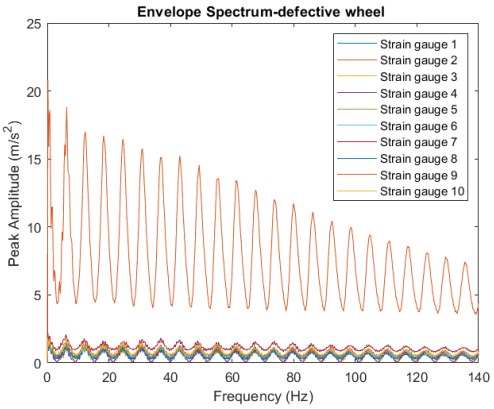

Wf2, *V*=60 km/h, track class 4

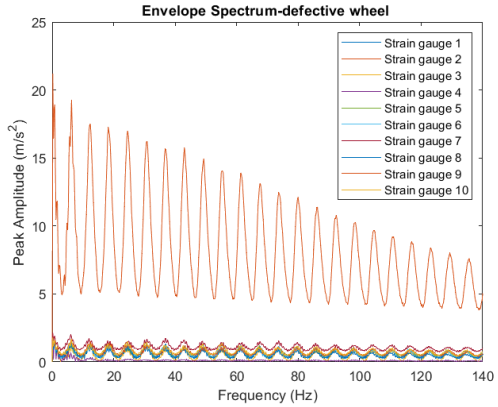

Wf2, *V*=60 km/h, track class 5

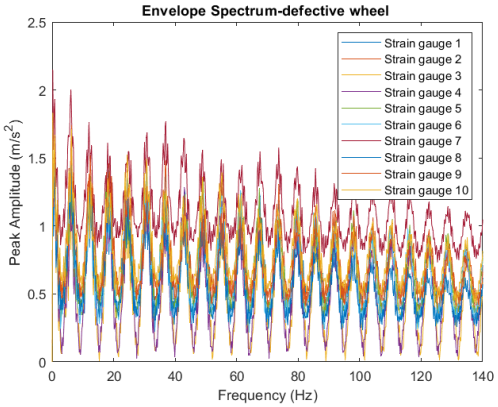

Wf2, *V*=60 km/h, track class 6

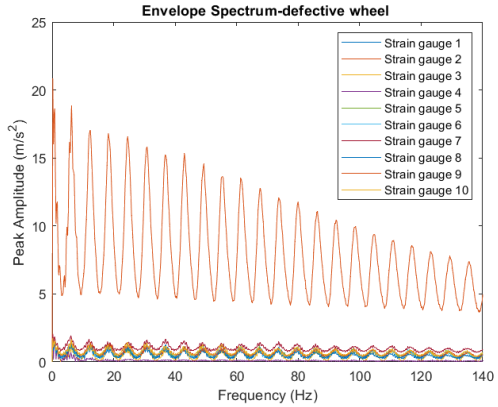

Wf2, *V*=60 km/h, track class 7

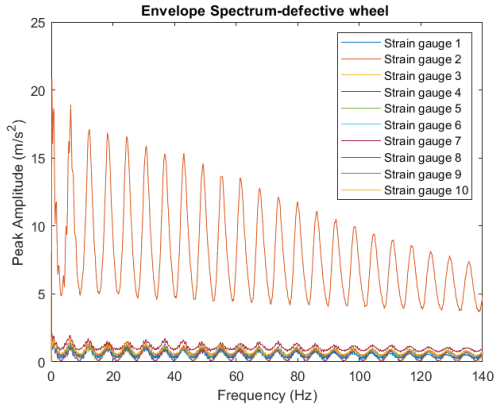

Wf2, *V*=60 km/h, track class 8

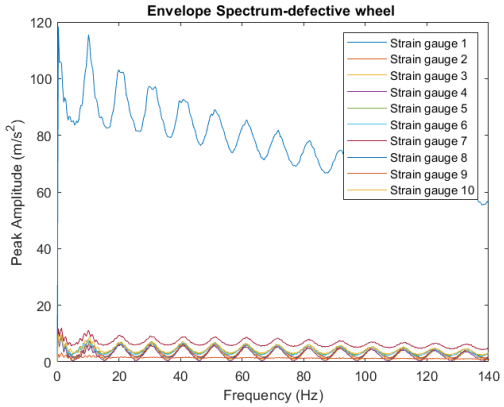

Wf2, *V*=100 km/h, track class 4

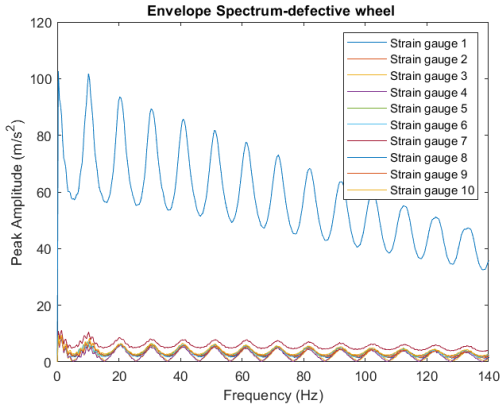

Wf2, *V*=100 km/h, track class 5

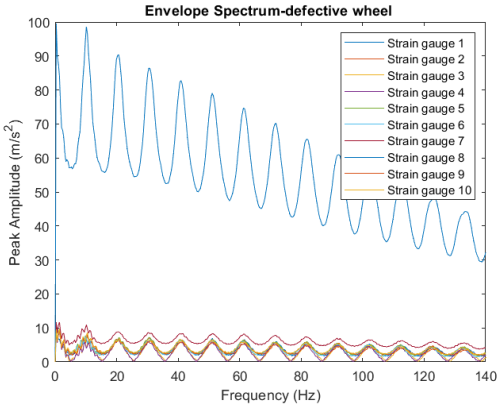

Wf2, *V*=100 km/h, track class 6

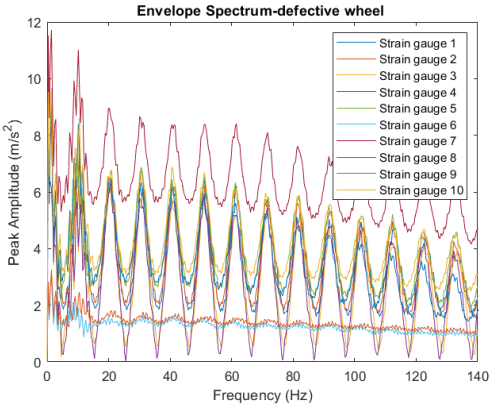

Wf2, *V*=100 km/h, track class 7

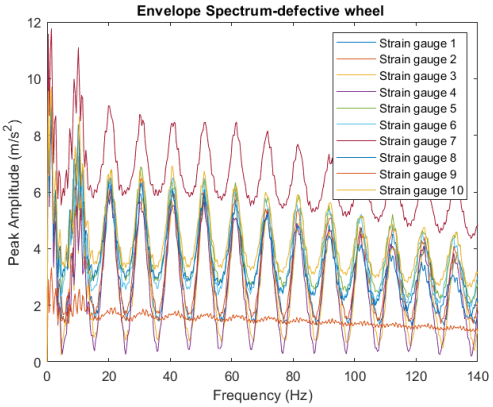

Wf2, *V*=100 km/h, track class 8

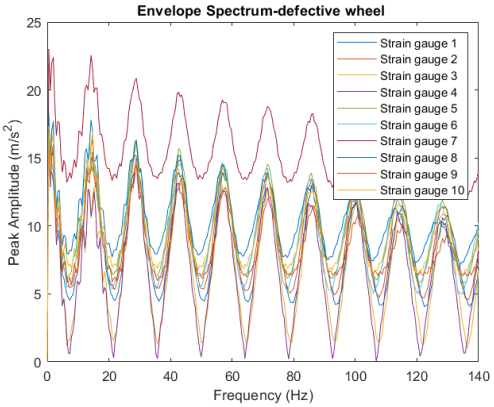

Wf2, *V*=140 km/h, track class 6

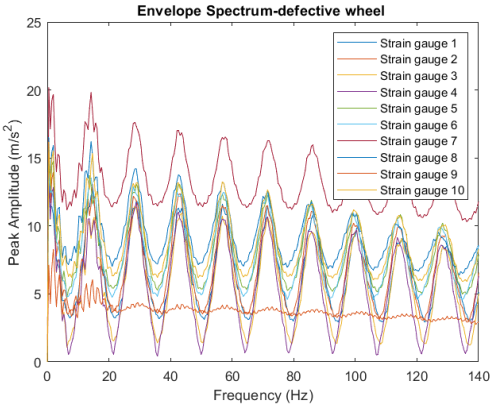

Wf2, *V*=140 km/h, track class 8

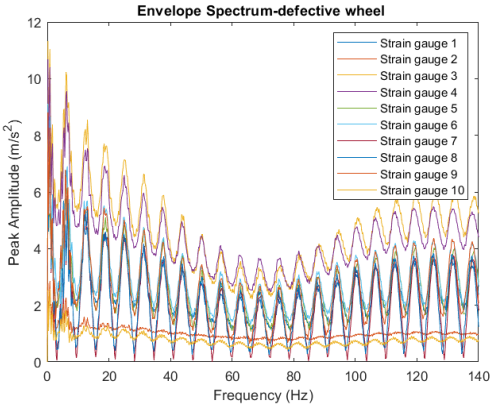

Wf3, *V*=60 km/h, track class 3

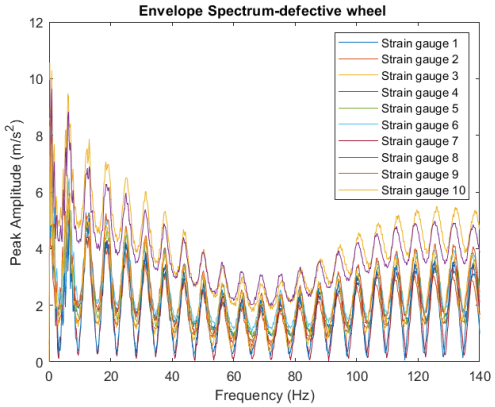

Wf3, *V*=60 km/h, track class 4

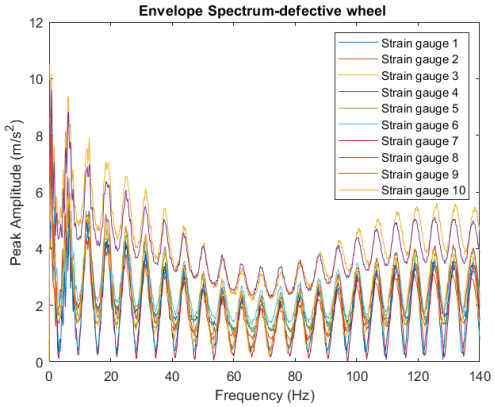

Wf3, *V*=60 km/h, track class 5

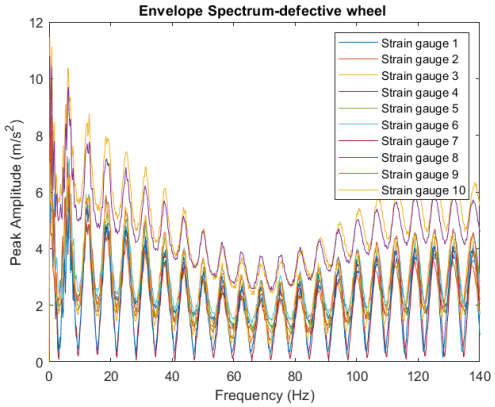

Wf3, *V*=60 km/h, track class 6

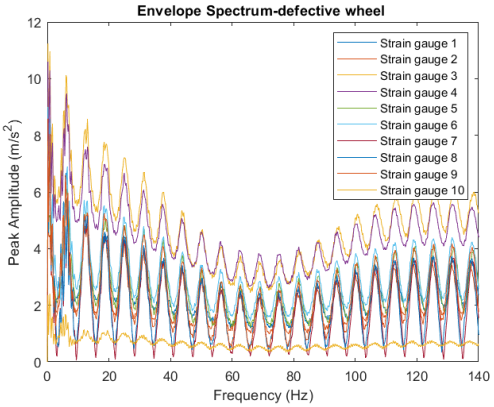

Wf3, *V*=60 km/h, track class 7

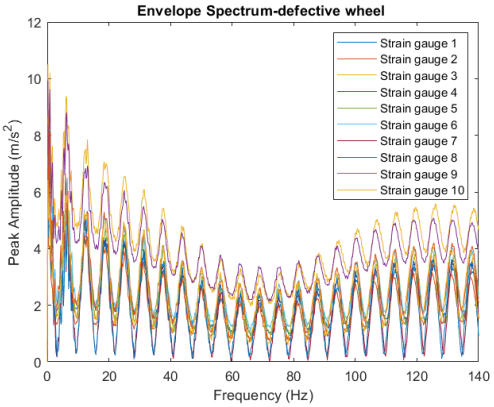

Wf3, *V*=60 km/h, track class 8

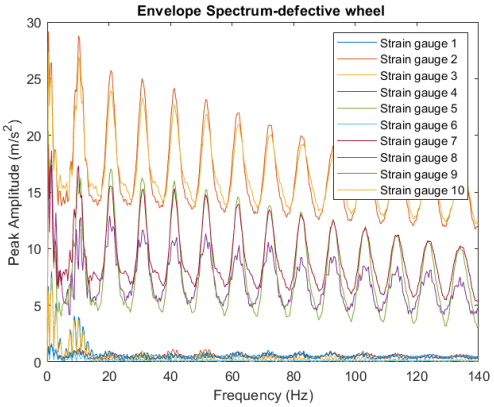

Wf3, *V*=100 km/h, track class 4

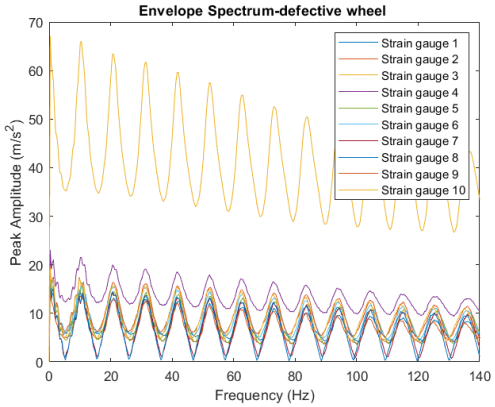

Wf3, *V*=100 km/h, track class 5

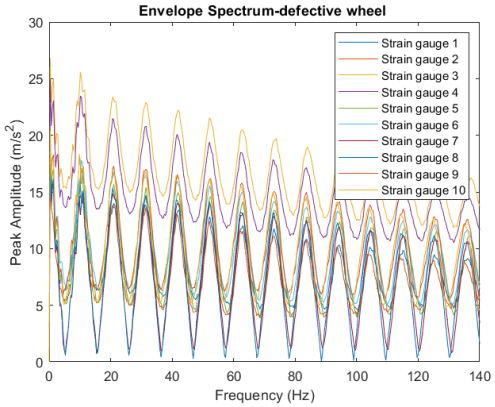

Wf3, *V*=100 km/h, track class 6

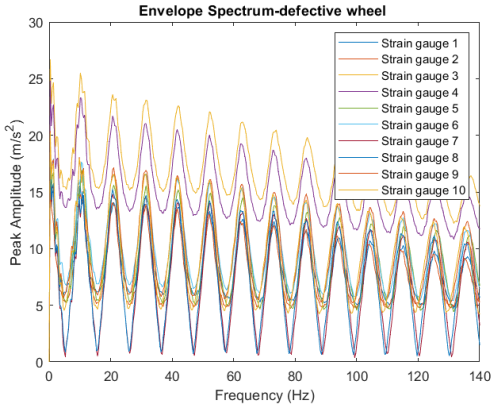

Wf3, *V*=100 km/h, track class 7

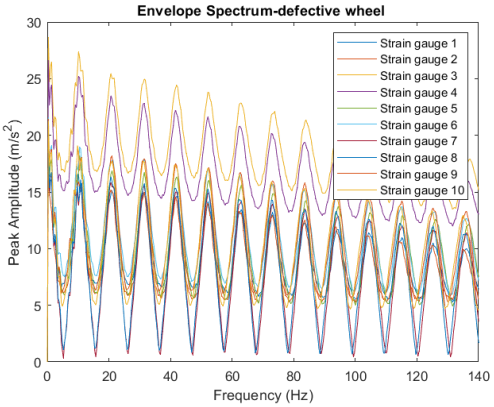

Wf3, *V*=100 km/h, track class 8

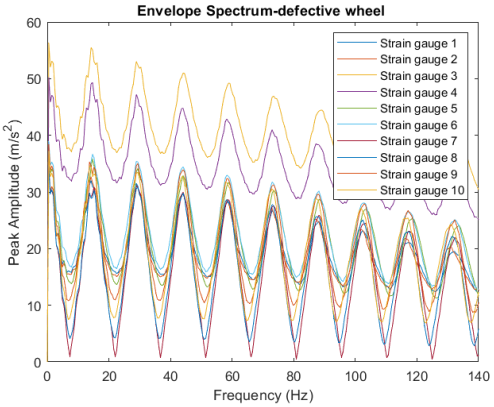

Wf3, *V*=140 km/h, track class 6

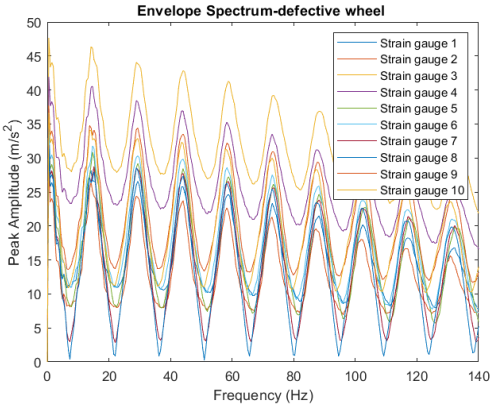

Wf3, *V*=140 km/h, track class 8

Polygonised Wheel

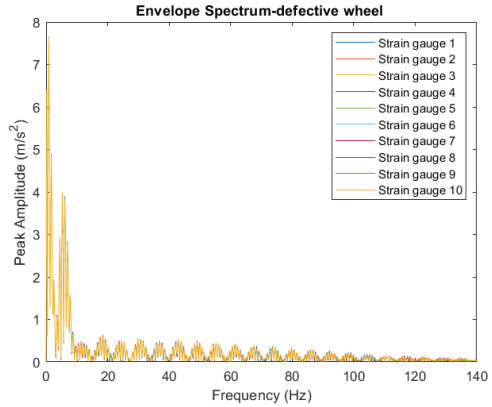

wp5, *V*=60 km/h, track class 7

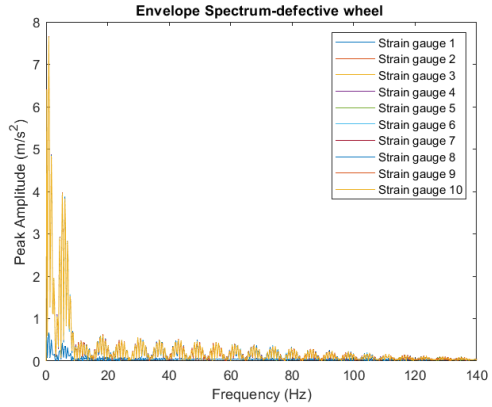

wp20, *V*=60 km/h, track class 7

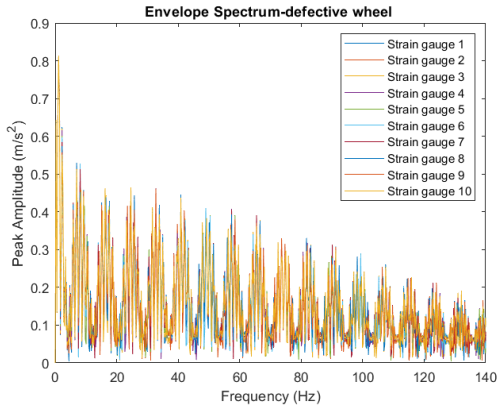

wp5, *V*=80 km/h, track class 7

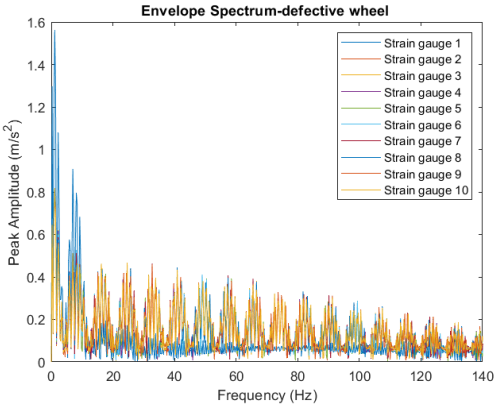

wp20, *V*=80 km/h, track class 7

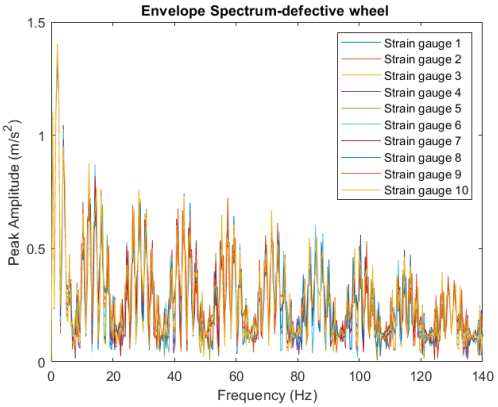

wp5, *V*=140 km/h, track class 7

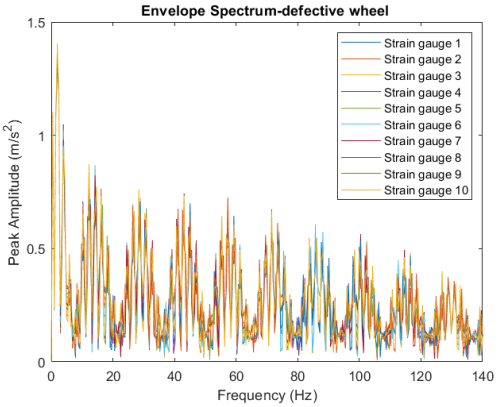

wp20, *V*=140 km/h, track class 7

Healthy Wheel

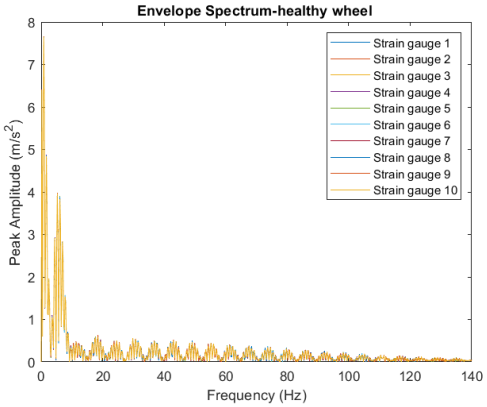

Healthy wheel, *V*=60 km/h, track class 7